Nano Research
2020, 13(4): 891–918
ISSN 1998-0124 CN 11-5974/O4
https://doi.org/10.1007/s12274-020-2749-1

Review Article

Present advances and perspectives of broadband photo-detectors based on emerging 2D-Xenes beyond graphene

Bing Wang[1], Shipeng Zhong[1], Yanqi Ge[1], Huide Wang[1], Xiaoling Luo[2] (✉), and Han Zhang[1] (✉)

[1] College of Physics and Optoelectronic Engineering, College of Electronic and Information Engineering, Institute of Microscale Optoelectronics, Collaborative Innovation Centre for Optoelectronic Science & Technology, Key Laboratory of Optoelectronic Devices and Systems of Ministry of Education and Guangdong Province, Shenzhen Key Laboratory of Micro-Nano Photonic Information Technology, Guangdong Laboratory of Artificial Intelligence and Digital Economy (SZ), Shenzhen University, Shenzhen 518060, China
[2] Department of Ophthalmology, Shenzhen People's Hospital, Second Clinical Medical College of Jinan University, Shenzhen 518020, China

© Tsinghua University Press and Springer-Verlag GmbH Germany, part of Springer Nature 2020
Received: 29 November 2019 / **Revised:** 16 January 2020 / **Accepted:** 7 March 2020

ABSTRACT

As an excellent optical device, photodetectors have many important applications, such as communication technology, display technology, scientific measurement, fire monitoring, aerospace and biomedical research, and it's of great significance in the research of nanotechnology and optoelectronics. Graphene, as the first two-dimensional (2D) single-element nanomaterial, has the advantages of high carrier mobility, high strength, high light transmittance and excellent thermal conductivity, and it's widely used in various nano-optical devices. The great success of graphene has led scientists to extensive research on other 2D single-element nanomaterials. Recently, a group of novel 2D single-element nanomaterials have attracted a lot of attention from scientists because of its excellent physical, chemical, electronic, mechanical and optical properties. Furthermore, it has opened a new door for the realization of new and efficient photodetectors. The group of 2D single-element nanomaterials are called 2D-Xenes and used to make high-performance photodetectors. Currently, there are few studies on photodetectors based on 2D-Xenes, but some 2D-Xenes have been applied to photodetectors and reported. Some of these have excellent photodetection performance, such as high photoresponsivity (R), broad spectral response range, fast photoresponse speed and high specific detectivity (D^*). Based on the novel 2D-Xenes, this review explores the types and preparation methods of 2D-Xenes, and the working mechanisms of 2D-Xenes photodetectors. Finally, the challenges and development trends of 2D-Xenes in the future are discussed. The research of 2D-Xenes is of great significance for the development of high-performance photodetectors in the future, and is expected to be widely used in other nanoelectronics and optical devices.

KEYWORDS

photodetectors, 2D single-element nanomaterials, 2D-Xenes

1 Introduction

The photodetectors can sense the existence of photons in the light. It's a semiconductor device that can convert incident light with electromagnetic radiation energy into a precise electrical signal, and has a wide range of applications in video imaging, optical communication, fire detection, radiometry and detection, astronomical detection, and so on [1–7]. According to different working wavelength ranges, photodetectors can be divided into ultraviolet (UV) photodetectors, visible (Vis) photodetectors, short-wave infrared (SWIR) photodetectors, long-wavelength infrared (LWIR) photodetectors, near-infrared (NIR) photodetectors, mid-infrared (MIR) photodetectors, far-infrared (FIR) photodetectors and terahertz (THz) photodetectors [8–11]. These photodetectors are widely used in different operating wavelengths.

Two-dimensional (2D) nanomaterials are usually composed of monolayer or few layers of atoms or molecular layers, which have strong molecular bond forces or ion bond forces in the layer and show weak van der Waals forces between layers [12, 13]. With two kinds of force interactions, 2D nanomaterials have excellent electrical, optical, magnetic and mechanical properties, and are considered to be applied to the manufacture of next-generation novel electronic and optical devices, especially photodetectors [14–31]. Besides, as a result of the weak intermolecular van der Waals, atomically thin 2D nanomaterials with strong interlayer quantum confinement effect can be obtained, thus improving the optoelectronic performance of the corresponding devices [32–34]. The first 2D nanomaterial, graphene, which was successfully prepared in 2004, which triggered an upsurge in the research of 2D nanomaterials by researchers all over the world [35]. Graphene is a honeycomb monolayer carbon atom separated from graphite block, which has excellent optical [36–60], electrical [35, 61], thermal and mechanical properties [62]. The graphene is not only a semiconductor material, but also a semi-metallic material. Its strength and transmittance are very high, and the carrier mobility is as high as 230,000 $cm^2/(V·S)$ [61]. A strong interaction is generated between the graphene and the photons, and the photons of any frequency in the ultra-wide band spectrum range in the UV–Vis–IR–THz wave band have a resonant photoresponse, and graphene have wide application prospects

Address correspondence to Han Zhang, hzhang@szu.edu.cn; Xiaoling Luo, LXL2603@vip.sina.com

in the field of ultra-fast and ultra-wide photodetectors [63–65]. However, the bandgap of the graphene is zero, which results in its carrier lifetime is not long, and the logic switching of the semiconductor cannot be realized, thus limiting its applications in the semiconductor industry [66–69]. Another typical 2D nanomaterials is transition metal dichalcogenides (TMDCs), which has excellent electronic, optical, physical, chemical, thermal and mechanical properties [70]. TMDC group has a typical formula-MX_2, where M include Ti, Hf, Zr, Ta, Nb, Mo, Re, W, and other transition metal element, and X represents chalcogen include S, Se or Te. Unlike the zero bandgap characteristics of graphene, many TMDCs have large bandgap and can change the number of layers so that tune bandgap. For example, bulk MoS_2 is a semiconductor with indirect bandgap of 1.3 eV, and it's a semiconductor with direct bandgap of 1.8 eV when it becomes monolayer [71]. The layer-related properties of TMDCs make them widely used in the fields of electrons, optoelectronics and nano-photons [72–79]. For example, TMDCs can be used to fabricate photodetectors with high on/off ratios, which is better than graphene with zero bandgap. However, some TMDCs exhibit low carrier mobility at room temperature, which limits their application ranges [80, 81].

Recently, researchers have discovered a novel group of 2D single-element nanomaterials. They are followers of graphene, called Xenes, where 'X' represents the name of a given chemical element, and 'ene' comes from the sp^2-hybrid alkene bond, which represents alkene. Therefore, Xenes represents 2D nanomaterials made up of atoms of a single element. The distance between their atoms is large, which leads to the upper and lower atoms buckled and the formation of honeycomb crystal structure [82]. According to the 2D single-element nanomaterials Xenes that have been discovered so far, 2D single-element nanomaterials Xenes includes borophene, gallenene, graphene, silicene, germanene, stanene, plumbene, phosphorene, arsenene, antimonene, bismuthene, selenene and tellurene. Graphene was the first to be discovered in Xenes, and then borophene [83], silicene [84], germanene [85, 86], stanene [87], phosphorene [88–140], arsenene [141, 142], antimonene [143–153], bismuthene [154–161], selenene [162, 163] and tellurene [164–169] appeared. Researchers have used many methods to prepare 2D-Xenes, including mechanical exfoliation, physical vapor deposition (PVD), pulsed laser deposition (PLD), chemical vapor deposition (CVD), liquid-phase exfoliation, wet-chemical synthesis, chemical exfoliation, etching and plasma-assisted synthesis, among which molecular beam epitaxy (MBE) is the most widely used preparation method. These preparation methods have their own advantages and disadvantages, which will be highlighted in the section 3. The unique crystal structure of Xenes makes them have many excellent physical, chemical, electronic and optical properties [170, 171]. Compared with other 2D materials such as bulk silicon, TMDCs and perovskites, Xenes have many excellent properties. For example, bulk silicon is fragile, while borophene has better flexibility [172]. The carrier mobility of TMDCs is lower at room temperature, while gallenene [173], silicene [174], germanene [175], phosphorene [176–178], arsenene [179–181], antimonene [181, 182], bismuthene [181, 183], selenene [184, 185], tellurene [186–188] all have higher carrier mobility. Perovskite contains lead and have certain toxicity, while most Xenes are green, environmentally friendly materials. In addition, Xenes have excellent properties such as quantum spin hall effect (QSHE), spin-orbit coupling (SOC) effect, 2D topological properties and layer-dependent bandgap, which make them have broad application prospects in photodetectors [189, 190], optoelectronics [191–195], sensor [196], field effect transistor (FET) [197], photocatalysis [198] and biomedicine [199, 200].

In this review, we introduce the types of 2D-Xenes, and clarify the structure and properties of various 2D-Xenes. Then, we illustrate various methods of preparing 2D-Xenes, as well as the working mechanisms of photodetectors based on 2D-Xenes. Nowadays, the photodetectors based on 2D-Xenes are still in the initial stage and have not received a lot of reports, and we don't discuss the research of graphene based photodetectors, which has been discussed elsewhere [4]. At the end of the paper, we put forward some opinions on the development of photodetectors based on 2D-Xenes in the future.

2 The types of 2D-Xenes

From the distribution of elements in the periodic table, the 2D single-element nanomaterial Xenes is distributed in the group III, IV, V and VI. Group III has boron and gallium, and their single-element materials are named borophene and gallenene, respectively. Group IV has silicon, germanium, stannum and lead, and their single-element materials are named silicene, germanene, stanene and plumbene. Group V has phosphorus, arsenic, antimony and bismuth, and their single element materials are named as phosphorene, arsenene, antimonene and bismuthene. Group VI has selenium and tellurium. Their single-element materials are named selenene and tellurene, respectively. The characteristics of these 2D single-element materials will be discussed separately below.

2.1 Group III

Group III includes two single-element materials such as borophene and gallenene. At present, there have been a lot of researches on these two materials.

2.1.1 Borophene

Boron is adjacent to carbon in the periodic table, so boron may have many properties as excellent as carbon [201]. Boron atom has three valence electrons, which makes its bonding mechanism extremely complex. Boron can not only form conventional strong covalent bonds, but also form a series of multicenter chemical bonds. Boron has hundreds of crystal structures because of boron atoms has stronger bonding ability than carbon atoms [202, 203]. Bulk boron has characteristics of three-position polyhedral structure, and all of them are insulators. Borophene is a 2D material with thick monatomic layer composed of boron atoms, which has rich physical and chemical properties. At first, the structure of borophene was predicted by first-principles studies, and then a lot of experiments were carried out [204]. Finally, through epitaxial growth of boron atom on silver metal surface, monolayer boron with different atomic configurations of buckled and flat structures was synthesized [205]. The morphology of boron atoms grown on silver metal surface is shown in Figs. 1(a)–1(d) [205, 206]. Figrues 1(a) and 1(b) show monolayer borophene with buckled structure. Figures 1(c) and 1(d) show monolayer borophene with flat structure. After the successful growth of borophene, scientists have done a lot of researches on borophene, and found that borophene has many excellent properties. For example, borophene has both non-metal and metal properties, and its conductivity is higher than that of intrinsic graphene. Borophene also has mechanical compliance and optical transparency. Borophene is the lighter and thinnest 2D metal reported at present [201, 207, 208]. In addition, the multicenter chemical bonds contained in the borophene give it rich chemical property and strong chemical activity. The theoretical study

show that borophene has excellent mechanical properties, such as flexibility and elasticity, which makes borophene have a potential application prospect in composite materials, flexible electronic devices and optically controlled devices [172]. Some researchers also have obtained the electron structure, chemical bond, optical, electronic and thermodynamic properties of borophene by first-principles calculations [209]. Compared with other 2D materials having a honeycomb structure, borophene has a unique crystal structure, exhibits high anisotropy and thus has large optical anisotropy and electrical conductivity. Studies have shown that single-crystal ultrathin boron nanosheets (UBNSs) has anisotropy, free of trap state, large specific surface area, high photoresponse and good field emission performance [210]. It can be used in high-performance field emission electron source and high-speed photodetectors with high sensitivity [210].

2.1.2 *Gallenene*

Gallium exists in liquid form at room temperature and exhibits metal properties in its bulk crystals [173, 211, 212]. It has different forms under non-standard pressure and temperature, such as tightly filled metal phases or boron-like molecular morphology [213, 214]. Bulk gallium shows α-Ga, which is the only phase that displays metal and molecular characteristics under zero pressure [212]. Kochat et al. used a simple technique to peel off the surface solid layer from Ga molten phase for the first time, which produced a thin atomic 2D gallium layer, known as gallenene [215]. They explained the structure of gallenene in detail through theoretical knowledge. At first, because the most stable phase of the bulk gallium morphology is α-Ga, they discussed the stability of the layers obtained in the specified direction in the crystal α-Ga by density functional theory (DFT). Then, the results of calculated electron localization functions (ELF) show that the first adjacent Ga-Ga bonds exhibit covalent bond force, while the other adjacent Ga-Ga bonds such as the second, third, and fourth show metal properties.

The forces of gallium atoms between layers in the direction of 100 (a_{100}) are both metal bonds and covalent bonds, while the forces of gallium atoms between layers in the direction of 010 (b_{010}) are only covalent bonds, as shown in Figs. 1(e)–1(g) [215]. By extracting one monolayer along 100 (a_{100}) and another monolayer along 010 (b_{010}), they relax them and construct a thin layer of gallenene. After complete relaxation, gallenene a_{100} is transformed into honeycomb structure, and gallenene b_{010} maintains its original structure. Gallenene b_{010}

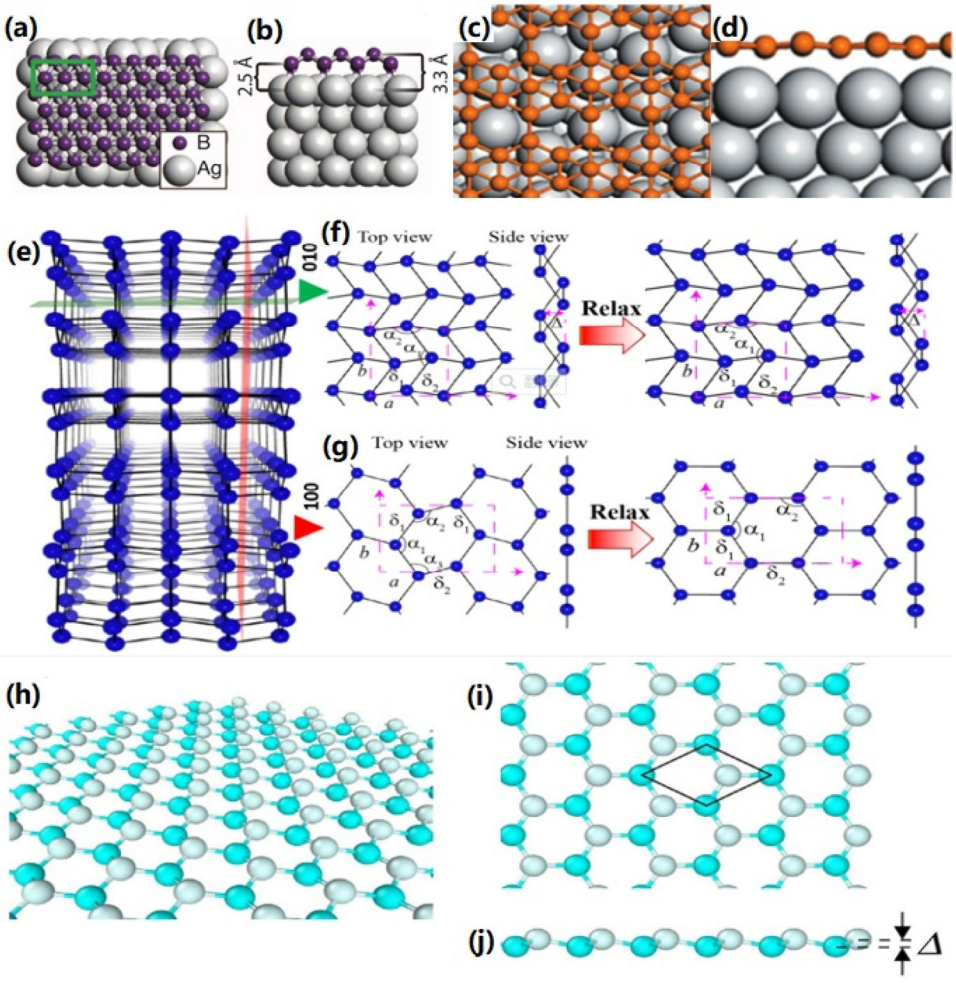

Figure 1 The structure of borophene, gallenene, silicene, germanene, stanene and plumbene. (a) The top view of borophene with buckling structure. (b) The side view of borophene with buckling structure (adapted with permission from Ref. [205], © American Association for the Advancement of Science 2015). (c) The top view of borophene with flattening structure. (d) The side view of borophene with flattening structure (adapted with permission from Ref. [206], © Springer Nature 2016). (e) The crystal structure of gallenene. (f) The gallenene monolayer structure extracted from the block α-Ga along the 010 direction is completely relaxed, the converted diamond-shaped structure. (g) The gallenene monolayer structure extracted from the block α-Ga along the 100 direction is completely relaxed, the converted honeycomb structure (adapted with permission from Ref. [215], © The Authors, some rights reserved; exclusive licensee American Association for the Advancement of Science 2018). (h) The perspective view of silicene, germanene, stanene and plumbene. (i) The top view of silicene, germanene, stanene and plumbene. (j) The side view of silicene, germanene, stanene and plumbene (adapted with permission from Ref. [216], © IOP Publishing Ltd. 2018).

has a quasi 2D multilayered structure compare with gallenene a_{100}. The two different forms of gallenene are separated on 1.32 Å vertically and show buckling structure, which often occurs in other 2D-Xenes such as silicene, germanene, stanene, plumbene, and phosphorene. Their experimental results show that gallenene has great application potential in plasma, sensor and electrical contact field. Meantime, gallenene, as a 2D material, will also have important applications in the field of photodetectors.

2.2 Group IV

Group IV has silicon, germanium, stannum and lead, and the atomic arrangement of these elements is similar to the hexagonal honeycomb structure of graphene. Unlike the structure in which all carbon atoms of graphene are bonded together in one plane, these elements form a hexagonal structure in their stable state, and all of them have low-buckled honeycomb structure, as shown in Figs. 1(h)–1(j) [216]. Graphene has the properties of sp^2-hybrid, while silicon, germanium, stannum and lead exhibit the properties of sp^2-sp^3-hybrid due to the preferential state of sp^3-hybrid. Their single-element materials are named silicene, germanene, stanene and plumbene. The following is an analysis of these four materials.

2.2.1 *Silicene*

Silicene is a 2D material with low-buckled honeycomb structure arranged by silicon atoms, and its structure is shown in Figs. 1(h)–1(j) [216]. Silicon is a semiconductor with indirect bandgap of 1.1 eV, while silicene is a semiconductor with zero bandgap [217, 218]. According to the first-principles calculation, silicene has high intrinsic carrier mobility [174]. The electron and hole mobilities of silicene are 2.57×10^5 $cm^2/(V{\cdot}S)$ and 2.22×10^5 $cm^2/(V{\cdot}S)$ at room temperature, respectively [174]. The band structure of silicene show that π and π^* bands intersect with a linear dispersion at Fermi energy level, which lead zero bandgap and form a kind of Dirac cones at the K and K' points in the hexagonal Brillouin zone without SOC [84, 219, 220]. The unique feature of band structure shows that the charge carrier in the silicon layer is a massless Dirac fermion. Silicene also have other unique materials properties, including QSHE, strong SOC, huge magneto resistance, field tunable bandgap, superconductivity, nonlinear electro-optical effect and piezomagnetism effect, etc. These excellent properties make silicene have great applications in the field of sensor, FET, optical device, hydrogen storage, gas adsorbent, thermoelectrics and Li-ion batteries [85, 221, 222]. However, the most problem of silicene is zero bandgap. Therefore, in order for silicene to be widely used in more electronic and photoelectronic device directions, such as photodetectors, opening a suitable bandgap is the most important problem to be solved at present.

2.2.2 *Germanene*

Similar to silicene structure, germanene is also a low buckle honeycomb structure, which remains stable at high strain, as shown in Figs. 1(h)–1(j) [216, 219, 223, 224]. According to the theoretical prediction, compared with graphene, the intrinsic bandgap of germanene's Dirac point is as high as 23.9 meV, which is due to the atomic number of germanium is larger than that of carbon and has the stronger SOC [225]. Germanene has high carrier mobility and extraordinary topological properties. Several theoretical reports have found that functionalized germanium can exhibit interesting physical and topological properties, such as QSHE, magnetism, metal ferromagnetism and highly anisotropic photoresponse. For example, polygermanes (GeH) have shown strong photoluminescence properties, which is expected to be used in photodetectors [226]. Halogenated germanene has a stable bandgap, which can be further widened by applied electric field, and the 2D topological phase can also be realized at room temperature by functionalization [227–229]. Therefore, germanene is considered to be a candidate material for Dirak fermion materials, which is used in high speed and low energy consumption FET, and functional germanene is expected to be widely used in the field of photodetectors.

2.2.3 *Stanene*

Bulk stannum mainly has two stable homogeneous structures: α-Sn (gray stannum) has the diamond cubic structure with low density and β-Sn (white stannum) has the expandable tetrahedral structure under environmental conditions [230]. As shown in Figs. 1(h)–1(j), the structure of stanene is similar to that of graphene hexagonal lattice. It consists of a diatomic layer of α-Sn (111), in which two triangular sublattices are superimposed to exhibit a buckle honeycomb lattice structure. In the void state, the stanene supports both the quantum spin Hall (QSH) state and the quantum abnormal Hall (QAH) state, which makes it possible to develop new topological insulator (TIs). Recent research results show that the functionalized stanene such as hydrogenated stanene (stanane) has excellent electron and optical properties such as high carrier mobility and a strain-tunable direct bandgap [231]. In addition, with the SOC effect and electron-hole interaction, the monolayer stanane has a strong photoresponse in the Vis and IR wavelength range [232]. Although it has the property of zero bandgap, stanene is considered to be a new type of quantum 2D materials because of its topological insulation and strong SOC, which may have great applications in the field of photodetectors.

2.2.4 *Plumbene*

The plumbene has a buckled honeycomb structure and shows metal properties, as shown in Figs. 1(h)–1(j). Pb-Pb bond distance of plumbene is 3 Å. According to the first-principles calculation, by electron doping, the independent plumbene can be converted from the normal insulator with a bandgap of 400 meV to the TIs with a volume gap of 200 meV [233]. Through functionalized modification, plumbene can show extraordinary topological insulation state [234]. For example, a new group of PbX monolayers have a large bandgap of 1.34 eV. Besides, through decorating with cyanogen (CN), PbCN has a giant bandgap of 0.92 eV. With the external strain, the bandgap can be tuned [235]. For the external strain, the QSH state of plumbene is more intense. Plumbene is expected to be widely used for the applications of topological phenomena in electronic and optical devices at room temperature.

2.3 Group V

Group V has phosphorus, arsenic, antimony and bismuth. Their monolayer materials are called phosphorene, arsenene, antimonene and bismuthene, respectively. They have high carrier mobility and broad tunable bandgap, which makes them potential candidates for nano-optical devices in the future. At present, there have been a lot of researches on these four materials, which are analyzed below.

2.3.1 *Phosphorene*

There are many allotropes of simple phosphorus. Compared with white phosphorus with small molecular crystal structure or red phosphorus with amorphous structure, the morphology of black phosphorus (BP) in air is the most stable, and its reaction activity is the lowest [236–238]. BP has four crystal structures, which are orthogonal, rhombic, simple cubic and

amorphous. At room temperature and pressure, BP has orthogonal crystal structure. There are four phosphorus atoms in the primary primitive cell of BP, each unit cell has eight atoms. Similar to the crystal structure of graphene, BP also has 2D layered structure and monolayer BP is called phosphorene [176, 239, 240]. However, unlike graphene, the phosphorus atoms in the same layer are not on the same plane, and each atom behaves as covalent bond force with the surrounding three atoms, showing a honeycomb fold structure, as shown in Fig. 2(a) [241]. In the layer, the phosphorus atom is connected with the three surrounding phosphorus atoms through the 3p hybrid orbital, and the s-p orbital hybrid makes the fold layered structure very stable [177, 178]. There are strong covalent bonds and a single electron pair in the layer, so each atom is saturated. The distance between the layers is 5.4 Å, and the interlayer atoms are van der Waals force [242]. The bulk BP is ap-type 2D indirect bandgap semiconductor material with a bandgap of 0.3 eV, while phosphorene is a direct bandgap semiconductor with a bandgap of 1.45 eV, in which conduction band bottom and valence band top at the same K point, and its bandgap size is related to the number of layers [243–245]. It has a strong effect on photons in the wavelength range from near-ultraviolet (NUV) to MIR, which is the greatest advantage of phosphorene. Besides, phosphorene has large carrier mobility [246]. The hole mobility may reach 10,000–26,000 $cm^2/(V·S)$. In addition, phosphorene have other important properties include excellent mechanical properties, high anisotropy transport, negative Poisson's ratio, photoluminescence properties, excellent thermoelectric properties, excellent optical properties and 2D topological properties induced by vertical electric fields. These unique characteristics make it have a great application prospects in many fields, especially in the field of photodetectors.

2.3.2 *Arsenene*

Simple arsenic exists in the form of gray arsenic, black arsenic and yellow arsenic. All three allotropes have layered rhomboid structure, among which gray arsenic is the most typical and stable of these three allotropes. Its structure is shown in Figs. 2(b) and 2(c) [180]. Bulk arsenic is a semi-metal with good electronic conductivity and its layered structure is stable under environmental conditions [179]. Arsenene share some common characteristics with graphene, such as honeycomb lattices. However, the bending structure of arsenic layer is used to improve its stability. The independent arsenene is semiconductor with an indirect bandgap of 2.49 eV, and the bilayer arsenene has an indirect bandgap of 0.37 eV [180]. In addition, under biaxial strain, it can be converted from indirect bandgap semiconductor to direct bandgap semiconductor. The excellent electronic properties make it have potential applications in the field of photodetectors, while the excellent mechanical properties can also play its role in mechanical sensing.

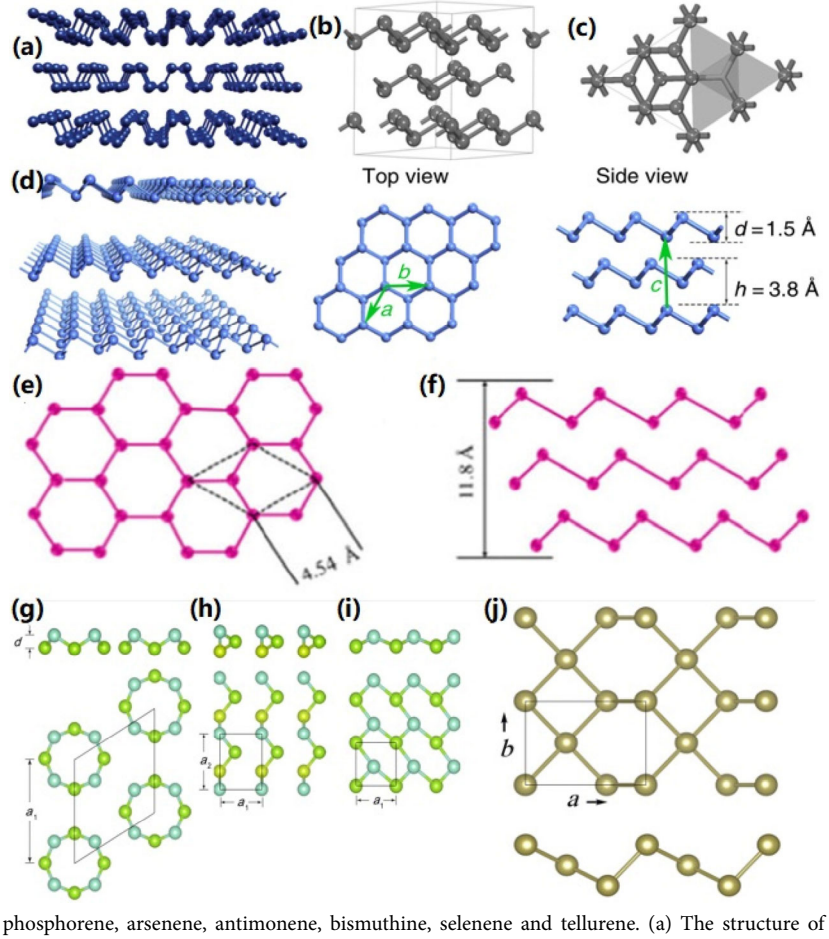

Figure 2 The structure of phosphorene, arsenene, antimonene, bismuthine, selenene and tellurene. (a) The structure of phosphorene (adapted with permission from Ref. [241], © WILEY-VCH Verlag GmbH & Co. KGaA, Weinheim 2016). (b) The side view of arsenene structure. (c) The top view of arsenene structure (adapted with permission from Ref. [180], © WILEY-VCH Verlag GmbH & Co. KGaA, Weinheim 2015). (d) The structure of β-antimonene (adapted with permission from Ref. [247], © Springer Nature 2016). (e) The top view of β-bismuthene structure. (f) The side view of β-bismuthene structure (adapted with permission from Ref. [160], © WILEY-VCH Verlag GmbH & Co. KGaA, Weinheim 2018). (g) The 0D atomic ring of selenene structure. (h) The 1D spiral atomic chain of selenene structure. (i) The 2D atomic layer of selenene structure (adapted with permission from Ref. [185], © IOP Publishing Ltd. 2017). (j) The top view and side view of tellurene structure (adapted with permission from Ref. [187], © American Chemical Society 2018).

2.3.3 Antimonene

Antimony has silver luster, dull, gray semi-metallic characteristics. Its layered structure is similar to one of BP to some extent, but the distance from the out-of-plane atom to the atom is short, which indicates that the interlayer interaction is stronger and hinders the mechanical spalling. There are three allotropes of bulk antimony, which are black antimony, gray antimony and explosive antimony. Gray antimony (β phase) is the most stable morphology of these three allotropes. Like gray arsenic, gray antimony has rhomboid structure and typical semiconductor characteristics, as shown in Fig. 2(d) [247]. After rapid cooling, the gray antimony can effectively form black antimony, which has higher chemical activity in the atmospheric environment. Under the action of heating or external stress, the explosive antimony can be converted into gray antimony [181]. The independent antimonene is a semiconductor with an indirect bandgap of 2.28 eV [182, 248–250]. Like arsenene, it can be converted from indirect bandgap semiconductor to direct bandgap semiconductor under biaxial strain [180]. Theoretical and experimental studies show that antimonene has many excellent properties, such as excellent thermal conductivity, high carrier mobility, high photonic absorption efficiency, strain-induced band transition and promising spin ion properties in the range of high frequency Vis light, which makes it possible to obtain potential applications in the field of photodetectors.

2.3.4 Bismuthene

Bismuth has a natural layered structure, while bulk bismuth is rhombic. Bismuthene has two kinds of allotropes, α-bismuthene and β-bismuthene. β-bismuthene's structure as shown in Figs. 2(e) and 2(f) [160]. Similar to antimonene, bismuthene has strong SOC, unique electron and ultra-fast photonic properties, which include nonlinear optical transmission, high temperature QSHE and ultra-fast saturated absorption. With a small direct bandgap of 0.5 eV, bismuthene has a stable low-buckle hexagonal structure and will become TIs under the action of external force [251, 252]. Based on DFT-SOC calculations, monolayer hexagonal buckled bismuthene is extraordinary in topology, besides, hexagonal buckled bismuthene on silicon substrate is also extraordinary in topology [183]. As the last and most important element of group V, bismuth will produce more significant QSHE and broad bulk bandgap because of its large atomic number [253, 254]. The carrier mobility of the bismuthene is also large, and has the superior photoluminescence property [255, 256]. These excellent properties make bismuthene very attractive and expected to to be widely used in optoelectronic devices. Previous researches have shown that bismuthene has stable topological properties, which is independent of the number of layers [257]. Therefore, bismuthene is expected to show strong topological properties at room temperature and maintain high structural stability, which makes bismuthene can be widely used in the next generation optoelectronic devices.

2.4 Group VI

Group VI includes selenium and tellurium. The 2D monolayer materials extracted from selenium and tellurium are called selenene and tellurene. Similar to other layered materials such as silicene, germanene, stanene and plumbene, they have chair-like buckle structures, which is not hexagonal but square. The topological insulators of selenene and tellurene have nontrivial edge states, which makes them widely used in the field of electronics. At present, there have been a lot of researches on these two materials, which are analyzed below.

2.4.1 Selenene

Selenium has both non-metallic and metallic properties. Selenium has many kinds of allotropes. Among them, three kinds of crystals (α monoclinic, β monoclinic, and grey triangle) are the most important, and also exist in the form of three amorphous solids. Some studies have shown that in α-Se and β-Se, the charge transport from the center to the external atoms is 0.18 and 0.04 e, respectively [184]. Besides, they have proved that monolayer α-Se has quite high carrier mobility and monolayer β-Se has large in-plane spontaneous polarization. Base on the DFT calculations in the generalized gradient approximation (GGA), some researchers have obtained the structure of selenene, as shown in Figs. 2(g)–2(i) [185]. Similar to the case of three dimensional (3D), 2D selenene atoms are easy to form double coor-dination bonds. Thus, the low-dimensional crystal structure of 2D selenene has different forms. The atomic ring is formed in the zero-dimensional (0D), and the spiral atomic chain is formed in the one-dimensional (1D). The force between the ring and the ring or between the chain and the chain is van der Waals force. 0D selenium atomic ring as shown in Fig. 2(g), and 1D selenium spiral atomic chain as shown in Fig. 2(h). They also developed a new layered structure of 2D selenene, as shown in Fig. 2(i). Similar to the structure of Xenes of group IV, this new structure presents a chair-like form, which shows that selenium atoms are arranged in a rectangular unit cell, and the atoms in the center of the new structure are tilted to one side. Unlike van der Waals forces in both 0D atomic rings and 1D spiral atomic chains, the forces between all atoms in the layer of the new layer structure are covalent bonds forces. Selenene has a very interesting electronic structure, and there are two gaped semi-Dirac cones in square Brillouin zone. In addition, selenene has many optical properties, such as high photo-conductivity, high piezoelectricity, thermoelectricity, nonlinear photoresponse and nontrivial topological properties [258–262]. These unique properties make it widely used in optoelectronic devices, especially photodetectors.

2.4.2 Tellurene

Tellurium is a kind of material with van der Waals force. Its spiral 1D atomic chain can be assembled into 1D filaments or 2D thin films (tellurene), which can be deposited by solution-based process [166, 263–266]. Bulk tellurium is a semiconductor with narrow bandgap of 0.34 eV. It has a triangular lattice, in which the spiral chain of a single tellurium atom is arranged together by weak bonds and spirals around the axis of the hexagonal basic element parallel to the direction of [0001]. On the same chain, each atom is connected to two adjacent atoms by covalent bonds. Tellurene has three tellurium atoms in a unit cell, as shown in Fig. 2(j) [187]. In addition, there is a kind of square tellurene structure, which is another crystal structure in tellurene, as shown in Fig. 2(i) [185]. Recently, some researchers have predicted a new type of monolayer tellurium with different structures, in which α-Te and β-Te have high carrier mobility, and its carrier mobility much higher than that of MoS_2 [267]. In particular, some people have synthesized β-Te and its direct bandgap is 1.47 eV [266, 268]. β-Te is more suitable for photovoltaic devices than α-Te with indirect bandgap of 0.75 eV. Tellurene has many important properties, such as semiconductor properties, photoconductive properties, thermoelectric properties and topological properties. Tellurene has a n-type and p-type mobility of up to 700 μm, and it's stable in the air [269]. Recent theoretical studies show that the absorption of light in low-layer tellurium is similar to

isotropism [188, 266]. For normal incident light, the efficiency of absorbing photons is about twice to three times that of phosphorene. Besides, the research results show that the absorption efficiency (that is, the absorbance of each layer) increases significantly with the decrease of the thickness of a small layer of tellurium layer, which is a kind of absorbance related to interlayer absorbance. This is due to inter-layer electronic hybrid and band dispersion associated with the thickness. With the increase of layer thickness, inter-layer electronic hybrid and band dispersion will become stronger. The excellent characteristics of highly isotropic absorbance and high carrier mobility show that tellurene has important applications in optoelectronic devices.

3 The preparation methods of 2D-Xenes

At present, there are many methods for preparing 2D-Xenes materials, which are generally divided into three categories: physical preparation methods, chemical preparation methods and other methods, all of which are summarized in Table 1.

Table 1 The preparations of 2D-Xenes

Group	Element	2D form	Materials synthesis	Thickness	Ref.
III	B	Borophene	MBE	Few-layer	[205, 206, 291–293]
			CVD	~ 0.8 nm	[352]
			Liquid-phase exfoliation	~ 1.8 nm, 20–50 nm	[83, 355, 356]
			Chemical exfoliation	Mono to few-layer	[371]
			Etching	15 nm	[83]
			Plasma-assisted synthesis	Multilayer	[379]
III	Ga	Gallenene	MBE	Mono to few-layer	[294, 295]
			solid-melt exfoliation	Few-layer	[215]
IV	Si	Silicene	MBE	Mono to muitilayer	[296–312]
			Chemical exfoliation	~ 0.37 nm, multilayer	[374, 375]
			Plasma-assisted synthesis	Multilayer	[378, 380]
IV	Ge	Germanene	Mechanical exfoliation	Few-layer	[86]
			MBE	Monolayer	[313–322]
			Plasma-assisted	Multilayer	[378, 381]
IV	Sn	Stanene	MBE	Mono to few-layer	[87, 323–325]
IV	Pb	Plumbene	MBE	Few-layer	[326]
V	P	Phosphorene	Mechanical exfoliation	Mono to muitilayer	[189, 240, 273–286]
			MBE	Monolayer	[327, 328]
			PLD	~ 2 nm	[350]
			CVD	~ 3.4 nm, Monolayer	[353, 354]
			Liquid-phase exfoliation	Mono to muitilayer	[191, 357–363]
			Wet-chemical synthesis	< 5 nm	[369]
			Chemical exfoliation	Few-layer	[372, 373]
			Etching	Monolayer	[377]
			Plasma-assisted synthesis	Monolayer, 4–50 nm	[378, 382, 383]
V	As	Arsenene	Mechanical exfoliation	Few-layer	[286, 287]
			MBE	Few-layer	[329]
			Liquid-phase exfoliation	5–12 nm, 33–49 nm	[364, 365]
V	As	Arsenene	Plasma-assisted synthesis	~ 14 nm	[384]
V	Sb	Antimonene	Mechanical exfoliation	Few-layer	[286–288]
			MBE	Mono to few-layer	[329–333]
			Liquid-phase exfoliation	~ 4 nm, 3–4.3 nm	[366, 367]
			Chemical exfoliation	31.6 nm, ~ 3.5 nm	[144, 376]
			Plasma-assisted synthesis	~ 5 nm	[385]
V	Bi	Bismuthene	Mechanical exfoliation	Few-layer	[286, 287]
			MBE	6–50 nm, few-layer	[334–338]
			Liquid-phase exfoliation	3.5–9.9 nm	[159, 368]
			Chemical exfoliation	4 nm	[160]
			Wet-chemical synthesis	—	[370]
VI	Se	Selenene	MBE	Few-layer	[339–346]
			Liquid-phase exfoliation	5–10 nm	[163]
VI	Te	Tellurene	MBE	2 nm	[347]
			PLD	6 nm	[351]
			Liquid-phase exfoliation	10 nm	[165]
			Wet-chemical synthesis	~ 6 nm, 7 nm, 12 nm	[166, 263–266]

3.1 Physical preparation methods

Physical preparation methods usually use optical and electrical techniques to evaporate materials in vacuum or noble gas, and then make atoms or molecules form nanoparticles. It also includes ball milling, spray and other mechanical processes. There is mechanical exfoliation, PVD, PLD, plasma-assisted process and so on.

3.1.1 *Mechanical exfoliation*

Graphene, as the first 2D nanomaterial, was exfoliated from the graphite block by mechanical exfoliation in 2004 [35]. Mechanical exfoliation is a simple and traditional physical preparation method, which has been widely used to obtain 2D nanoflakes [12, 270–272]. The method is usually carried out by adhesive tape to peel the bulk layered 2D materials repeatedly, so that it becomes a thin layered sheet, and then the adhesive tape attached to the layered sheet transfer and stay on the target substrate. The simple method has successfully produced some 2D-Xenes materials, such as germanene [86], phosphorene [189, 240, 273–286], arsenene [286, 287], antimonene [286–288] and bismuthene [286, 287].

3.1.2 *PVD*

PVD refers to the physical method of vaporizing the materials which wants to be a coating into an atom, molecule or ionizing it into an ion in a vacuum chamber. Under the action of a current bias voltage, the materials are attracted and deposited on the working surface to form a thin film deposition layer. Its main methods include vacuum evaporation, sputter coating, arc plasma plating, ion plating, and MBE [289, 290]. At present, PVD technology can not only deposit metal films, alloy films, but also compounds, ceramics, semiconductors, polymer films and so on. MBE method is used to prepare 2D-Xenes materials. In ultra-high vacuum environment, the source materials produce molecular beam through high temperature evaporation, glow discharge ionization, gas cracking, electron beam heating evaporation and so on. Then the molecular beam is sprayed on the substrate and reacts on the substrate surface. Finally, single crystal thin films are grown. The MBE method can be used to prepare all the 2D-Xenes materials includes borophene [205, 206, 291–293], gallenene [294, 295], silicene [296–312], germanene [313–322], stanene [87, 323–325], plumbene [326], phosphorene [327, 328], arsenene [329], antimonene [329–333], bismuthene [334–338], selenene [339–346] and tellurene [347]. In 2015, Mannix et al. made an electron beam evaporation using a high-purity boron source to successfully produce an atom-thin boron on an atomic level of clean Ag (111), as shown in Fig. 3(a) [205]. During the growth process, the boron flow is in the range of 0.01 monolayer/min to 0.1 monolayer/min, and the substrate temperature is held between 450 and 700 °C. After borophene was deposited, two different phases were found on the substrate by scanning tunneling microscopy (STM). As shown in Fig. 3(b), one is a kind of homogenous phase and the other is a kind of "striation" phase (marked with red and white arrows, respectively). They also obtained the dI/dV diagram of the electronic density of states (DOS) (where I and V are tunneling currents and voltages, respectively), as shown in Fig. 3(c). In the same year, Zhu et al. used MBE method to grow the stanene in the Bi_2Te_3 (111) [87]. The STM morphology of the substrate is shown in Fig. 3(d) [87], showing layer by layer of stanene. Figure 3(e) shows the STM morphology of large area stanene films [87]. Compared with the morphology

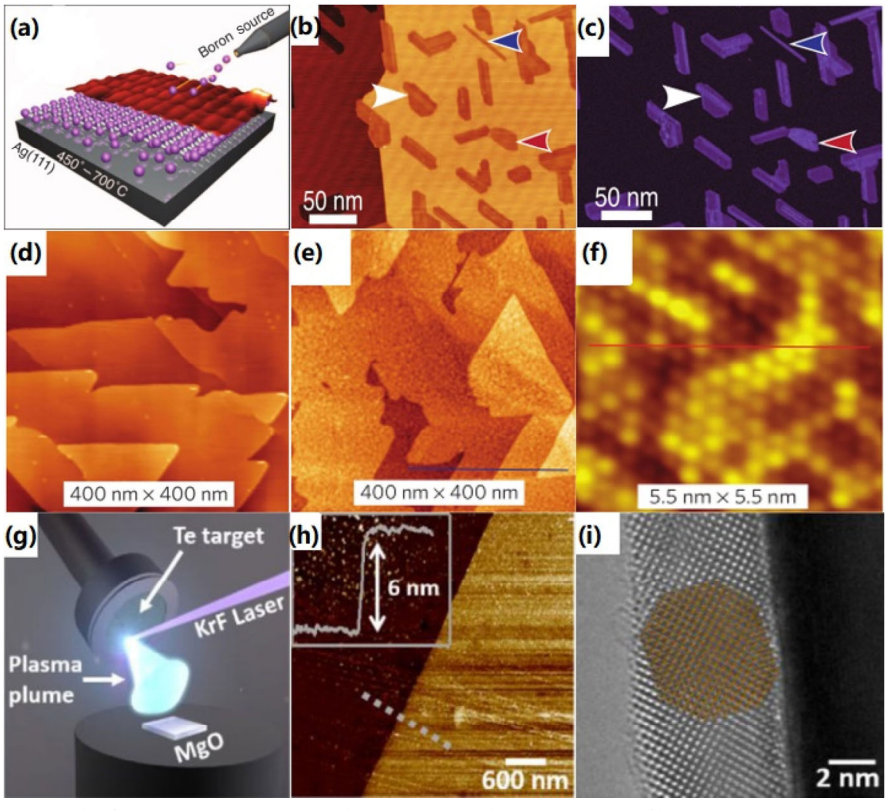

Figure 3 The preparation methods of borophene, stanene and tellurene. (a) The schematic diagram of boron atom growth on Ag(111). (b) STM topography of borophene. (c) The closed-loop dI/dV image of borophene (where I and V are tunneling current and voltage) (adapted with permission from Ref. [205], © The Authors, some rights reserved; exclusive licensee American Association for the Advancement of Science 2015). (d) STM topography of Bi_2Te_3(111) substrate. (e) Large area STM topography of stanene film. (f) Atomic resolution STM image of stanene (adapted with permission from Ref. [87], © Springer Nature 2015). (g) PLD diagram of tellurene. (h) AFM topography of tellurene. (i) HRTEM topography of tellurene (adapted with permission from Ref. [351], © IOP Publishing Ltd. 2019).

of Bi_2Te_3 (111) substrate, the morphology of the whole substrate surface is not interfered by the growth of stanene, and the step height of Bi_2Te_3 substrate can also be observed. The atom-resolved STM image of stanene (Fig. 3(f)) clearly shows the triangular lattice of stanene [87].

The advantage of MBE is that the source and substrate are heated and controlled respectively, and the growth temperature is low, which can form the hyperfine structure. It is easy to control the growth rate during the growth process, which is beneficial to the growth of multilayer heterogeneity, and the surface is in vacuum, which is conducive to real-time monitoring and detection. This is a kinetic process, which can grow crystals that are difficult to obtain by thermal equilibrium growth. However, it also has some shortcomings, such as complex equipment, large investment, slow extension growth rate and poor economic benefits. The parameters such as crystal smoothness, stability and purity are too strict, and defects and impurities will lead to high defect density on the surface of epitaxial films. Although it can obtain many new semiconductor materials, the atomic growth mechanism is still unclear.

3.1.3 PLD

PLD is a vacuum physical deposition technology, which focuses the high-power pulsed laser generated by the pulse laser on the surface of the target materials to generate high temperature and ablation on the surface of the target materials, and further generates a high-temperature and high-pressure plasma ($T > 10^4$ K), then the plasma-directed local expansion is deposited on the substrate, and finally a film is formed. The pulse deposition system typically includes a pulse laser, an optical path system (photo-optical scanner, a converging lens, a laser window, etc.), a deposition system (vacuum chamber, a vacuum pump, an inflation system, a target, a substrate heater), an auxiliary device (measurement and control device, a monitoring device, a motor cooling system) [348, 349]. At present, the PLD technology has synthesized the phosphorene [350] and tellurene [351]. In 2019, Apte et al. developed a tellurene film on a 1 cm × 1 cm single-crystal MgO (100) by PLD technology [351]. As shown in Fig. 3(g), the PLD process of the tellurene film shows that the tellurene film is continuous and appears flat under an optical microscope. The atomic force microscope (AFM) image is shown in Fig. 3(h) and it shows the thickness of the tellurene film is 6 nm. Besides, the high-resolution transmission electron microscope (HRTEM) image is shown in Fig. 3(i) and it also shows the thickness of the tellurene film is about 6 nm, which is same as the thickness of the sample measured by the AFM.

PLD technology has many advantages. First of all, it uses UV pulse laser with high photon energy and high energy density as the energy to produce plasma, so it is pollution-free and easy to control. Secondly, the ablation particles have high energy, which can accurately control the stoichiometry, realize the target film composition is close to consistent and simplify the work of controlling the film composition, especially suitable for the preparation of thin films with complex composition and high melting point. The process is simple and flexible, and there are many kinds of thin films that can be prepared. Of course, it also has some disadvantages. For example, it's not easy to prepare large-area films. And impurities on the surface of the thin film cause the film to be contaminated, and the uniformity of the prepared film is poor. For multicomponent compound films, if some cations have high vapor pressure, the equal stoichiometric growth of the films will not be guaranteed at high temperature.

3.2 Chemical preparation methods

Chemical preparation methods refer to the preparation of nanomaterials from molecules, atoms and ions through appropriate chemical reactions. The chemical preparation methods of 2D-Xenes materials mainly include CVD, liquid-phase exfoliation, wet-chemical synthesis and chemical exfoliation.

3.2.1 CVD

CVD is the most widely used technology to prepare 2D nanomaterials by the gas-phase method to date. The method is to control the nucleation growth process of the nanoparticle film by controlling the reaction gas pressure, the gas flow rate, the temperature of substrate materials and the like under the conditions of high temperature, plasma or laser-assisted conditions by the gas-phase reaction, or through the post-treatment of the films, the crystallization process of the amorphous films is controlled, and the nanostructured thin films are obtained. With CVD, borophene [352] and phosphorene [353, 354] have been successfully obtained. In 2015, Tai et al. used boron and boron oxide powder as the boron source to grow a large atomic thin borophene film on the copper (Cu) foil with the auxiliary gas of hydrogen [352]. The growth process of the borophene film is shown in Fig. 4(a). The borophene film was prepared by a self-made double-temperature-zone CVD furnace. Before the growth, the Cu foil was annealed at 1,000 °C for 1 h to make its surface smooth and expand the grain boundary. T_1 is set to 1,100 °C, and the boron dioxide (B_2O_2) vapor is obtained by annealing the mixture of B and B_2O_3. T_2 is set to 1,000 °C, and the borophene film is obtained by heating for 1 h. The AFM topography of the borophene film is shown in Fig. 4(b), and the thickness is 0.8 nm.

The advantages of CVD include the deposition device is simple, the reaction source materials needed for film formation are generally easy to obtain, and different chemical reactions can be selected for the preparation of a thin film. Consciously changing and adjusting the composition of reactants can also easily control the composition and characteristics of the film, so it is flexible. However, there are also some shortcomings, such as the deposition rate is not too high, and it is not as good as evaporation and ion plating, or even lower than the sputter coating. It is difficult for the substrate to deposit thin films locally or on a certain surface, which is not as convenient as PVD technology.

3.2.2 Liquid-phase exfoliation

Liquid-phase exfoliation is also one of the chemical methods to prepare 2D materials. By adding specific chemical solvents, such as N-methylpyrrolidone (NMP), dimethylformamide (DMF) or dimethyl sulfur oxide (DMSO), the energy is provided by means of ultrasonic assistance in order to weaken the van der waals force between the layers of the layered 2D materials without affecting the covalent bond in the materials layer. Finally, centrifugation is carried out to realize the exfoliation of 2D materials. The quality of 2D materials prepared by liquid-phase exfoliation is related to solvent selection, ultrasonic time and centrifugal rate. For example, the surface of the appropriate special solvent can match the 2D materials, and can provide enough interaction between the solvent and the 2D materials, as well as balance and satisfy the energy consumed by stripping the 2D materials. Choosing the right solvent can improve the peeling efficiency, stabilize them and prevent them from gathering again [355]. Some 2D-Xenes materials such as borophene [83, 355, 356], phosphorene [191, 357–363], arsenene [364, 365], antimonene [366, 367], bismuthene [159,

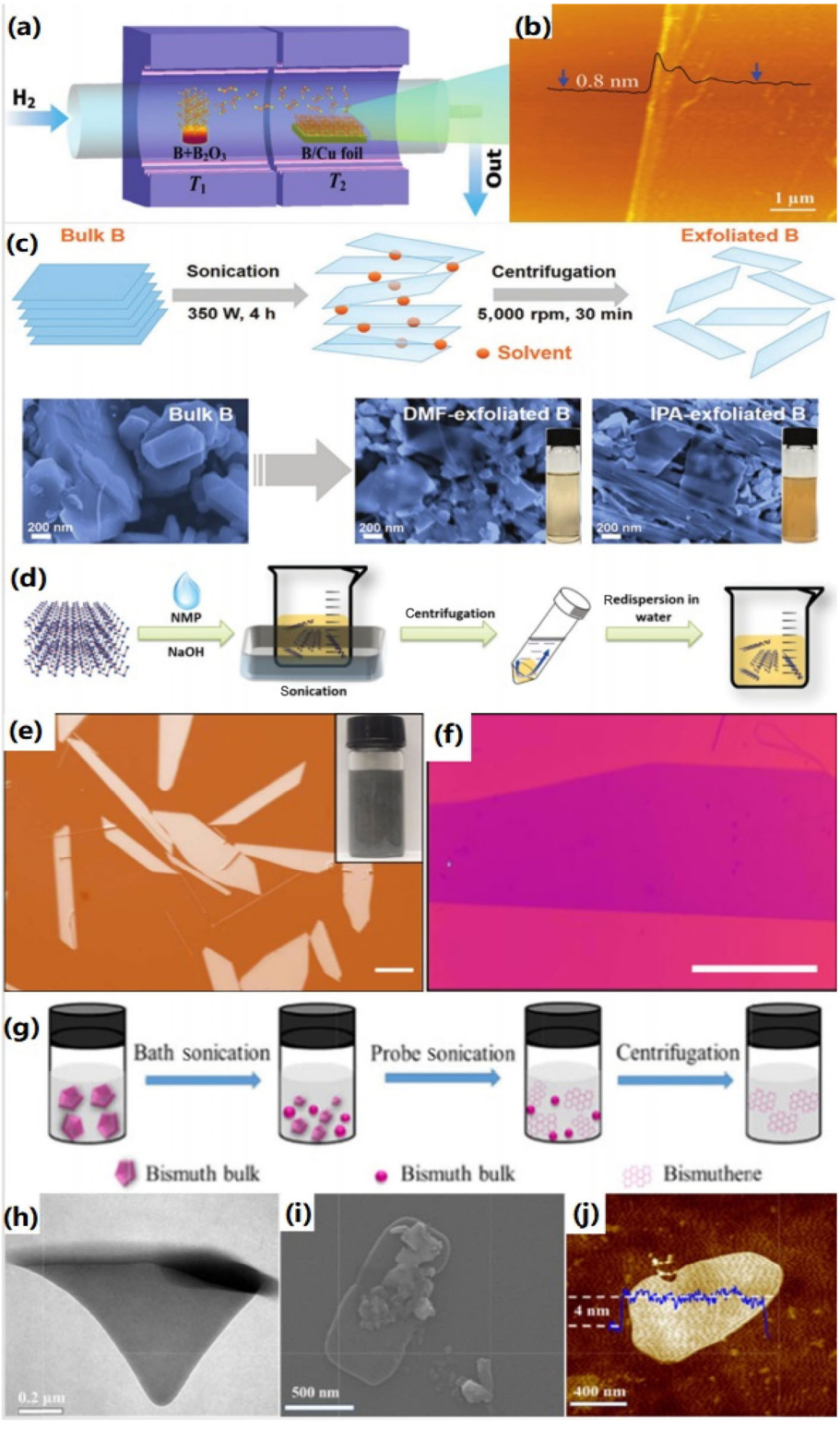

Figure 4 The preparation methods of borophene, phosphorene, tellurene and bismuthine. (a) The CVD growth schematic diagram of borophene film. (b) AFM topography of borophene film (adapted with permission from Ref. [352], © WILEY-VCH Verlag GmbH & Co. KGaA, Weinheim 2015). (c) Liquid-phase exfoliation schematic diagram of borophene film (adapted with permission from Ref. [356], © American Chemical Society 2018). (d) Liquid-phase exfoliation schematic diagram of phosphorene (adapted with permission from Ref. [191], © WILEY-VCH Verlag GmbH & Co. KGaA, Weinheim 2015). (e) The optical image of solution-grown tellurene. Insert map: the optical image of tellurene solution dispersion. (f) AFM topography of tellurene (adapted with permission from Ref. [266], © Macmillan Publishers Limited, part of Springer Nature 2018). (g) The preparation of bismuthene. (h) TEM images of bismuthene. (i) SEM image of bismuthene. (j) AFM image of bismuthene (adapted with permission from Ref. [160], © WILEY-VCH Verlag GmbH & Co. KGaA, Weinheim 2018).

368], selenene [163] and tellurene [165] , have been successfully synthesized by this method. In 2018, Li et al. prepared borophene by liquid-phase exfoliation, as shown in Fig. 4(c) [356]. They put bulk boron in DMF and isopropanol (IPA), and control the thickness and size of borophene by changing solvent type and centrifugal rate. The average thickness and area of borophene peeled by DMF are 1.8 nm (4 borophene layers) and 20,000 nm^2, respectively, while the thickness and area of borophene sheets peeled by IPA are 4.7 nm (11 borophene layers) and 1,800 nm^2, respectively. In addition, the basic NMP

solvent stripping method of phosphorene is shown in Fig. 4(d) [191]. The bulk BP is added to the saturated mixed solution of NaOH and NMP and then peeled off by ultrasound for 4 h. After ultrasonic treatment, phosphorene in the mixed solution is separated by means of centrifugation and move to water.

Liquid-phase exfoliation has the advantages of simple process, low cost, high concentration of suspension and stable dispersion system, which makes this method have a broad application prospect. However, it still has some shortcomings, such as the solvent is not volatile, the boiling point is high, the subsequent removal is difficult, and the yield of monolayer materials is low.

3.2.3 *Wet-chemical synthesis*

Wet-chemical synthesis is a process for the preparation of materials by chemical reaction in a liquid phase, in which surfactants in the liquid phase act to control the size, shape, morphology, and stability of the materials being prepared. At present, there are many wet-chemical synthesis methods for preparing nano-materials, such as precipitation method, spray pyrolysis method, sol-gel method, hydrothermal method, micro-emulsion method, etc. A few layers of BP were prepared by wet-chemical hydrothermal method [369]. Ultrathin bismuth nanosheets were also prepared by wet-chemical synthesis [370]. Tellurene was also synthesized by wet-chemical synthesis [166, 263–266]. For example, Wang et al. synthesized tellurene by wet-chemical synthesis [266]. In a typical process, sodium tellurite (Na_2TeO_3) and proper amount of polyvinylpyrrolidone (PVP) were put into double distilled water and stirred at room temperature to form a uniform solution. The solution was poured into a stainless-steel autoclave lined with polytetrafluoroethylene and then filled with ammonia and hydrazide hydrate (N_2H_2). The autoclave was sealed and maintained at the reaction temperature for a period of time. When the autoclave was cooled to room temperature, the silver ash solid product was precipitated by 5,000 rpm centrifugal precipitation and washed with distilled water for 5 min. Finally, tellurene was obtained. The optical image of tellurene in solution is shown in Fig. 4(e). The AFM morphology image is shown in Fig. 4(f).

The advantages of wet-chemical synthesis method are relatively low cost to achieve high yield and large-scale production of 2D nanomaterials, which is potentially suitable for industrial production. However, the synthesis is easily affected by the reaction stage, including reaction temperature, reaction time, precursor concentration and solvent, so the monolayer nanomaterials are difficult to be synthesized by wet-chemical synthesis method.

3.2.4 *Chemical exfoliation*

The chemical exfoliation method refers to putting the materials into a chemical solvent, and inserting a chemical solvent molecule between the inner layer and the layer of the materials so as to achieve the purpose of layer-by-layer separation. The chemical exfoliation method includes sonochemical exfoliation method and electrochemical exfoliation method. Borophene was prepared by sonochemical exfoliation [371]. A variety of solvents, such as DMF, acetone, IPA, water and ethylene glycol (EG), were used to synthesize freestanding borophene. The researchers used a rapid stripping method based on the principle of electrochemistry to obtain the layered phosphorene from the bulk BP [372]. Besides, some researchers obtained phosphorene from bulky BP by electrochemical cathode exfoliation [373]. In addition, some researchers prepared silicene by redox assisted chemical exfoliation [374]. Silicene has also been prepared by chemical exfoliation method [375]. Other researchers have prepared antimonene quantum dots (QDs) by electrochemical exfoliation [144, 376]. In 2017, with sonochemical exfoliation, bismuthene was prepared by Lu et al. and the synthesis process is shown in Fig. 4(g) [160]. The typical process of synthesis of bismuthene by sonochemical exfoliation is as follows: using IPA as raw materials, the bulk bismuth is first ground into bismuth powder, then the mixture solution of proper amount of IPA and bismuth is put into a spiral glass bottle with proper amount of IPA, and then the suspension obtained is centrifuged at 5,000 rpm for 20 min with probe ultrasound under ice bath for 10 h. The transmission electron microscopy (TEM) image of bismuthene as shown in Fig. 4(h), and it shows a lateral size of about 0.8 μm for bismuthene. The scanning electron microscope (SEM) image of bismuthene is shown in Fig. 4(i), showing the crystal structure of bismuthene. The AFM image of bismuthene is as shown in Fig. 4(j), and the height of 4 nm for bismuthene is presented.

The chemical exfoliation method has the advantages of easy control, low temperature in the synthesis process, high expand ability and low required cost. At the same time, the method also has some disadvantages, for example, it is difficult to control the quality of the control structure, the process is complicated, the reaction time is long, and the solvent used is difficult to remove and is not environment-friendly.

3.3 Other preparation methods

In addition to physical and chemical preparation methods, there are also other methods for the preparation of 2D-Xenes materials, such as etching and plasma-assisted synthesis.

3.3.1 *Etching*

Etching refers to the process of selectively removing unwanted materials from the surface of the materials by physical or chemical method. There are two basic etching processes in the semiconductor manufacturing process, which are dry etching and wet etching, respectively. The dry etching is to expose the surface of the silicon wafer to the plasma generated in the air, the plasma is through a window opened in the photoresist, and a physical or chemical reaction occurs with the silicon chip so as to remove the exposed surface materials. The wet etching is a material that reacts with the material on the surface of the silicon chip through the liquid chemical reagent, so as to achieve the effect of removing unwanted materials. Etching techniques have produced a number of 2D-Xenes materials, such as borophene [83] and phosphorene [377]. The researchers used a novel approach to the preparation of high-quality borophene [83]. The method combines thermal oxidation etching method and liquid-phase exfoliation method, in which the thermal oxidation etching method is an improvement method of dry etching. In this way, they prepared an ultra-thin borophene nanosheet, which shows the average size is 110 nm and the average thickness is 3 nm. In 2016, Pei et al. thinned phosphorene by dry etching to controllable produce high quality phosphorene with a specified number of layers, as shown in Figs. 5(a)–5(d) [377]. At first, phosphorene was etched by oxygen plasma, as shown in Fig. 5(a). In the process of oxygen plasma etching, the top layer of phosphorene is oxidized to P_xO_y, and forms a protective layer on this basis. Through further oxygen plasma etching, oxygen plasma can penetrate the P_xO_y layer so that oxidize underlying phosphorene layer, which make the phosphorene layer thinner and increase the thickness of P_xO_y. After oxygen plasma etching, there is a dynamic balance between the oxidation of phosphorene and the physical removal of P_xO_y layer, which makes the P_xO_y layer

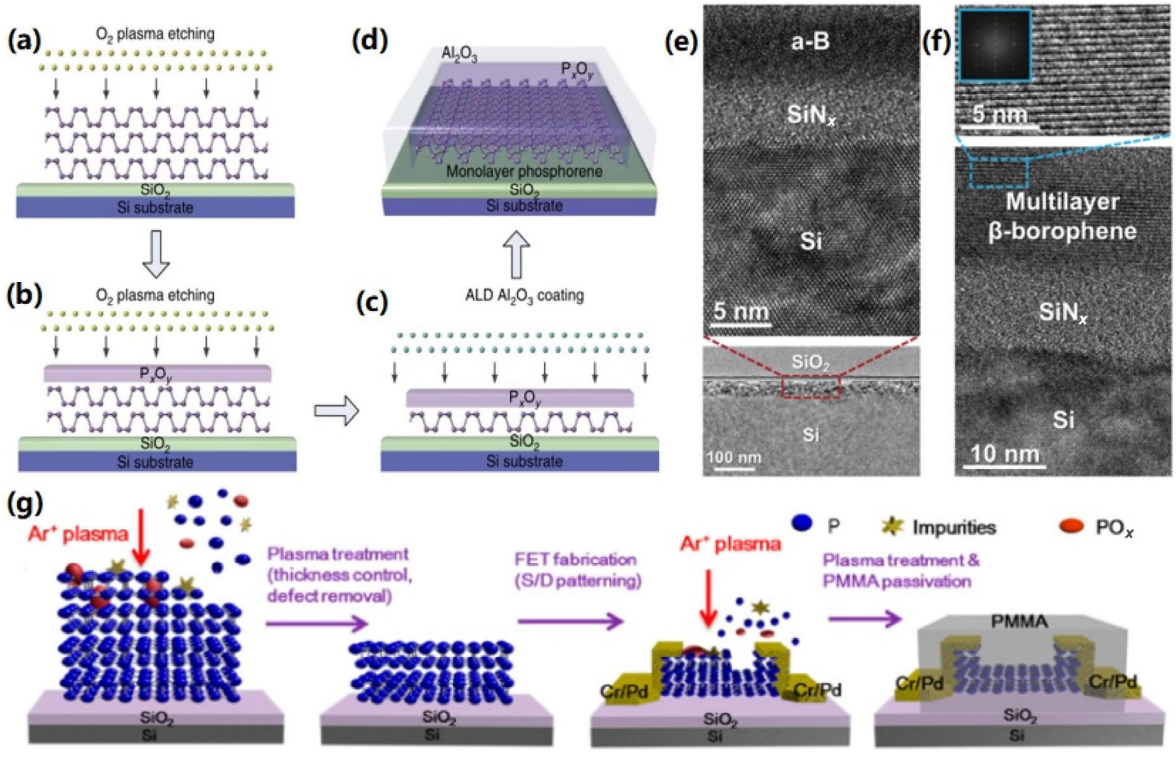

Figure 5 The preparation methods of phosphorene and borophene. (a)–(d) Etching process flow chart of phosphorene film (adapted with permission from Ref. [377], © Springer Nature 2016). (e) TEM image of boron injected substrate after nitrogen plasma immersion. (f) TEM image of multilayer β-borophene/SiN_x/p-type silicon layer structure (adapted with permission from Ref. [379], © WILEY-VCH Verlag GmbH & Co. KGaA, Weinheim 2016). (g) The thinning process of phosphorene film (adapted with permission from Ref. [383], © American Chemical Society 2015).

maintain constant thickness and the etching rate becomes constant, as shown in Fig. 5(b). Any specified number of layers or even monolayer phosphorene can be accurately manufactured because of constant etching rate, as shown in Fig. 5(c). Because phosphorene is unstable in air and easy to oxidize, an Al_2O_3 protective layer is deposited on phosphorene by atomic layer deposition (ALD) technique, as shown in Fig. 5(d).

Dry etching can realize anisotropy etching, and there is no need to use chemicals, but the cost is high and less used in microfluidic chip fabrication. Plasma may cause device damage. Wet etching is characterized by strong adaptability, uniform surface of the materials and less damage to the substrate, but the effect may not be good and the etched pattern is difficult to grasp.

3.3.2 *Plasma-assisted synthesis*

The plasma is a form of substance that is a major component of free electrons and charged ions, and it's referred to as the fourth state of the substance. It includes ions, electrons, atoms and molecules that are more reactive than the ground-state atoms or molecules, thus demonstrating the enormous potential for the preparation and improvement of 2D materials through energy-efficient and cost-effective method [378]. The plasma-assisted synthesis can be used to thin the 2D materials, and can also be used for auxiliary PVD, and can also be used for auxiliary CVD. The 2D-Xenes materials can be synthesized with the aid of plasma such as borophene [379], silicene [378, 380], germanene [378, 381], phosphorene [378, 382, 383], arsenene [384], and antimonene [385]. In 2016, Tsai et al. synthesized multilayer β-borophene on silicon substrate by plasma assisted process combined with boron ion implantation [379]. They first introduced boron ions into p-type silicon substrate by ion implantation machine, and then immersed the substrate in nitrogen plasma. The samples were annealed for 30 min after plasma immersion. The TEM images of boron injected substrate after nitrogen plasma immersion were obtained by using TEM to detect the annealed cross section structure, as shown in Fig. 5(e). The low rate image shows that the damage layer is produced after the substrate surface is bombarded by ions in the process of implantation. The high rate images show that the damage layer is uniformly covered by SiN_x and amorphous boron. After annealing, amorphous boron is recrystallized into crystal boron and multilayer borophene are produced, as shown in Fig. 5(f). In 2015, Jia et al. prepared few-layer phosphorene thin films with controllable thickness through modulating plasma treatment of phosphorene nanosheets [383]. Figure 5(g) shows the plasma treatment, the thinning process of phosphorene layer and the resulting unclean removal of phosphorene films surface. After the source/leakage electrode pattern, the exposed phosphorene thin films were treated by plasma and passivated by poly (methyl methacrylate) (PMMA). In order to control the thickness of the phosphorene films without destroying the morphology and crystal structure of the phosphorene films, the thickness of the phosphorene films is controlled by changing the plasma processing time.

The plasma-assisted synthesis has the important advantages of low temperature, rapid synthesis and high efficiency. These advantages result from unique plasma materials and a plasma-surface interaction created by ionization, excitation and dissociation of the source gas. By controlling the transfer of the plasma confinement, the plasma energy, the gaseous precursor and the ion energy to the materials and the surface, it is possible to control the materials morphology and structural uniformity. In addition, the presence of the strong electric field in the plasma shell can lead the 2D materials to grow in the vertical direction of the substrate, thereby synthesizing 2D materials with high crystal line and vertical orientation, which

is significant for applications requiring high surface area and communication porosity.

4 The working mechanisms of photodetectors

The photodetectors are based on the photoelectric effect, which is to convert the optical signal into an electrical signal, such as a photocurrent or a photovoltage. The working mechanisms of the photodetectors includes the photoconductive effect (PCE), the photovoltaic effect (PVE), the photogating effect (PGE), the photothermoeletric effect (PTE) and the photobolometric effect (PBE). According to the working mechanisms of photodetectors, photodetectors are divided into photon detector and thermal detector, in which the photon detector comprises photoelectric conductor, photodiode and photoelectric transistor [5, 386, 387]. In the following, the working mechanism of photodetectors based on 2D-Xenes will be introduced in this paper. Meanwhile, the working mechanisms and corresponding performance of these photodetectors are summarized in Table 2.

4.1 PCE

PCE means that, when the semiconductor is irradiated with light, photo-generated carriers are generated inside the semiconductor, and the concentration of carriers is increased, thereby increasing the conductivity of the semiconductor and

Table 2 Summary of photodetectors based on 2D-Xenes

Materials	Working mechanism	Spectral range	R (A/W)	EQE (%)	Response time (ms)	D^* (Jones)	Ref.
Borophene	PCE	UV	465	1.78×10^5	2.4×10^{-3}	4.91×10^{11}	[210]
Phosphorene	PCE	UV–Vis–NIR	9×10^4	10^6	1	3×10^{13}	[390]
Phosphorene	PCE	MIR	—	—	6.5×10^{-5}	—	[391]
Phosphorene	PCE	400–900 nm	7×10^6	1×10^9	—	—	[392]
			4.3×10^6	2×10^9	—	—	[392]
Phosphorene	PCE	Vis–IR	1.5×10^8	—	0.01	2.1×10^{10}	[276]
Phosphorene	PCE	MIR	51.83	—	—	—	[278]
Phosphorene	PCE	Vis	1.4×10^4	—	—	—	[382]
Phosphorene/InSe	PCE	Vis–NIR	53.8	1,020	22	—	[189]
Phosphorene	PGE	MIR	82	—	—	—	[396]
Phosphorene/Graphene	PGE	NIR	3.3×10^3	—	—	—	[112]
Phosphorene/Al	PVE	NIR	6.2×10^{-3}	—	13	1.04×10^{11}	[397]
Phosphorene	PVE	Vis–NIR	4.8×10^{-3}	—	1	—	[273]
Phosphorene/Se	PVE	Vis	15.33	2,993	150	—	[274]
Phosphorene	PVE	Vis–IR	230	—	4.8	—	[275]
Phosphorene	PVE	NIR	0.18	0.75	15	10^{11}–10^{13}	[277]
Phosphorene/MoS_2	PVE	Vis–NIR	—	—	0.013	—	[279]
Phosphorene/MoS_2	PVE	Vis	0.418	0.3	—	—	[280]
Phosphorene/ReS_2	PVE	UV	11,811	—	—	—	[282]
Phosphorene	PVE	Vis–NIR	0.1534	—	0.015	3.1×10^{11}	[283]
Phosphorene/WSe_2	PVE	Vis–IR	10^3, 0.5	100	0.8	10^{14}, 10^{10}	[284]
b-AsP	PVE/PTE	MIR	0.015–0.03	6.1	0.54	9.2×10^9	[399]
Phosphorene	PTE	Vis–MIR	0.35×10^{-3}	—	—	—	[402]
Phosphorene	PTE	THz	—	—	—	—	[281]
Phosphorene	PTE	NIR	53	—	—	—	[285]
Bismuthene	PVE	UV–Vis	294.9×10^{-6}		200	8.68×10^8	[159]
Bismuthene/n-Si	PVE	—	—	—	—	—	[335]
Selenene	PCE	0.21 mW/cm^2	263	—	100	—	[389]
Selenene	PCE	Vis	3.27×10^4	—	0.57	—	[340]
Selenene/TiO_2	PVE	Vis	0.1		1.4	6.2×10^{12}	[341]
Selenene/ZnO	PVE	UV	2.65×10^{-3}	—	0.69	—	[342]
Selenene/n-Si	PVE	UV–Vis	0.0374		0.235	10^{11}	[343]
Selenene	PCE	UV–IR	0.006	—	< 25	—	[346]
Selenene	PCE	UV–Vis	10.45×10^{-6}	—	—	—	[163]
Selenene/ReS_2	PVE	Vis	98	—	45	6×10^{10}	[344]
Selenene	PVE	UV–Vis	0.294	—	0.12	0.94×10^{13}	[345]
Selenene/Te nanotubes	PVE	UV–Vis–NIR	0.001	—	520	—	[165]
Tellurene	PCE	SWIR	13	—	—	2×10^9	[263]
Tellurene/Bi QDs	PVE	UV–Vis–NIR	142.79×10^{-6}	—	—	5.14×10^8	[264]
Tellurene	PGE	NIR	10^6	—	—	5×10^{13}	[266]
Tellurene	PCE	UV–Vis	13.4×10^{-6}	—	—	3.1×10^7	[164]

becoming easily conductive [355, 388]. As for the advantage of the PCE, that is, the difference of the movement velocity between two kinds of photo-generated carriers leads to higher photoconductive gain so that the corresponding photoresponsitivity (R) of the photodetectors are fine. Usually, the external quantum efficiency (EQE) of the photodetectors is over 100. When concerned the disadvantage of PCE, firstly, it mainly lies in bias voltage being applied to the devices, which can result in big dark current so as to exhaust the energy resource. Additionally, the response range is depended on the bandgap, so the photodetectors based on PCE mechanism tend not to detect IR range [5, 6, 355].

For example, Qin et al. reported a 2D backgate selenium nanosheet photodetector [389]. The schematic diagram of which is shown in Fig. 6(a). Figure 6(b) shows the functional relationship between I_{ds} and gate voltage V_g under different laser lighting power densities, indicating that the photocurrent response of the photodetector can be tuned by V_g. The photodetector also have strong photoresponse at very low laser lighting power, and its photocurrent can reach 54 nA. Figure 6(c) shows that the R of the photodetector can reach 263 A/W and linearly related to the lighting power, indicating that the generation of photocurrent depends on the photo-generated carrier. Figure 6(d) shows that photocurrent has slow response speed. The rising time is 0.10 s and the fall time is 0.12 s. Selenium nanosheets, as a kind of 2D materials formed by 1D van der Waals materials, are widely used in the fabrication of electronic and photoelectronic devices. Wu et al. reported a high-quality few-layer phosphorene photodetector with a large UV-response [390]. They proved for the first time that the phosphorene UV photodetector has an excellent detectivity (D^*) of 3×10^{13} Jones, and in addition, by setting the drain-source bias voltage (V_{ds}) of 3 V, the UV R can be made to be 9×10^4 A/W. Phosphorene is proven to be a powerful choice for future optoelectronic applications, especially as the most advanced UV photodetectors. Ryan J. Suess et al. reported a phosphorene IR photodetector that works with PCE [391]. The results of the autocorrelation test show that the PCE in the phosphorene is beneficial to the development of sensitive and fast IR detection platform. In addition, Huang et al. reported a high-performance broadband phosphorene photodetector, whose structure with the spectral wavelength in the range of 400 to 900 nm as shown in Fig. 6(e) [392]. Figure 6(f) shows a plot of the photocurrent from 250 mW/cm^2 to 50 μW/cm^2 at 20 and 300 K, respectively, for different incident light power densities at a wavelength of 633 nm. The results show that the photodetector has ultra-high sensitivity. Figures 6(g) and 6(h) show the photoresponse of the photodetector at a wavelength of 633 and 900 nm, respectively. When the wavelength is 633 nm, the R is 6.7×10^5 A/W. At a NIR region of 900 nm, when the temperature is 20 K, the R of 7×10^6 A/W was obtained, and an R of 10^3 A/W is obtained at 300 K. Figure 6(i) shows that the EQE tends to increase from 900 to 400 nm, which is due to the absorption of the energy of photons resulting in the PCE.

4.2 PGE

As a special case of PCE, the PGE shows the change of conductivity under light. There are two cases of this effect. In

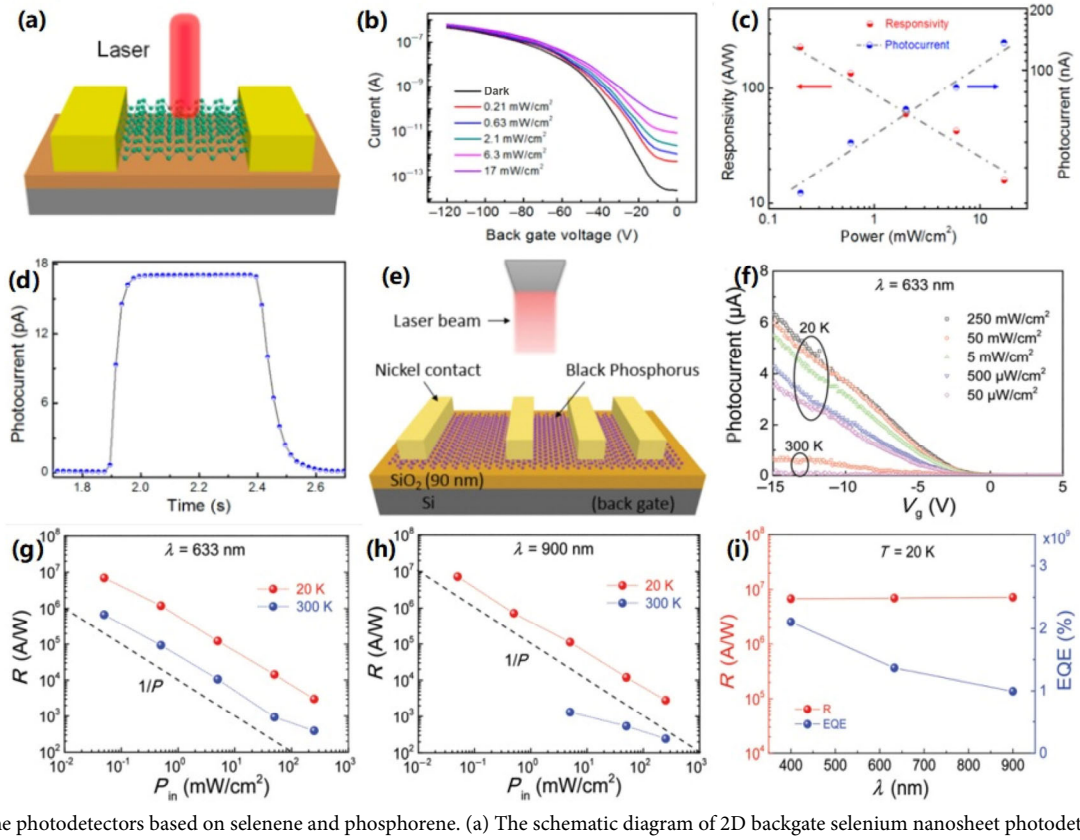

Figure 6 The photodetectors based on selenene and phosphorene. (a) The schematic diagram of 2D backgate selenium nanosheet photodetector. (b) The transfer curve of selenium nanosheet photodetector was measured at different laser lighting power densities at V_{ds} = 3 V. (c) The functional relationship between the photocurrent, R and the laser lighting power was measured at V_{ds} = 3 V and V_g = −80 V. (d) Typical rising or fall characteristics of photocurrent under laser illuminance switch (adapted with permission from Ref. [389], © American Chemical Society 2017). (e) The schematic diagram of broadband phosphorene photodetector. (f) The curve relationship between reverse V_g and photocurrent under different laser power densities. (g) and (h) The R of the photodetector at different incident laser power densities. The incident laser wavelength is 633 nm at G, and the incident laser wavelength is 900 nm at H. At 300 K, the device shows weak response to 900 nm incident laser, and at 20 K, they show very small difference. (i) EQE at different incident wavelengths (adapted with permission from Ref. [392], © WILEY-VCH Verlag GmbH & Co. KGaA, Weinheim 2016).

the first case, the semiconductor is irradiated by light, and two kinds of photo-generated carriers are produced under the excitation of light. One of the two photo-generated carriers is trapped in the local state at the defect or surface adsorption. In the other case, the generation of photo-generated carriers under light excitation occurs at the surface adsorbents or charge trap, so one kind of photo-generated carriers is transferred to the semiconductor as a conductive channel, so that the other photo-generated carriers are trapped in the surface adsorbents or trap. In both cases, the captured photo-generated carriers work as local gate, and can effectively modulate the conductivity of semiconductors caused by electrostatic interaction, so that the carriers in semiconductors cycle multiple times in the life cycle of captured photo-generated carriers, thus obtaining a higher gain [355, 393–395]. The advantage of PGE is analogue to that of the PCE. The trap resulting in the huge difference in the movement velocity between two kinds of carriers produces larger photoconductive gain so as to make the R of the devices is very high. And then, the disadvantage of PGE mainly can be divided into two points. One point is relatively bigger power consumption of the photodetectors based on PGE due to the applications of V_g. The other point is that dark current is usually bigger than that of PCE owing to PGE enhancing concentration of the carriers [5, 6, 355].

For example, Guo et al. reported a high gain IR phosphorene photodetector, the schematic diagram of which is shown in Fig. 7(a) [396]. Figure 7(b) shows that the absolute IR R of the source and drain bias voltages is 100 and 500 mV, respectively,

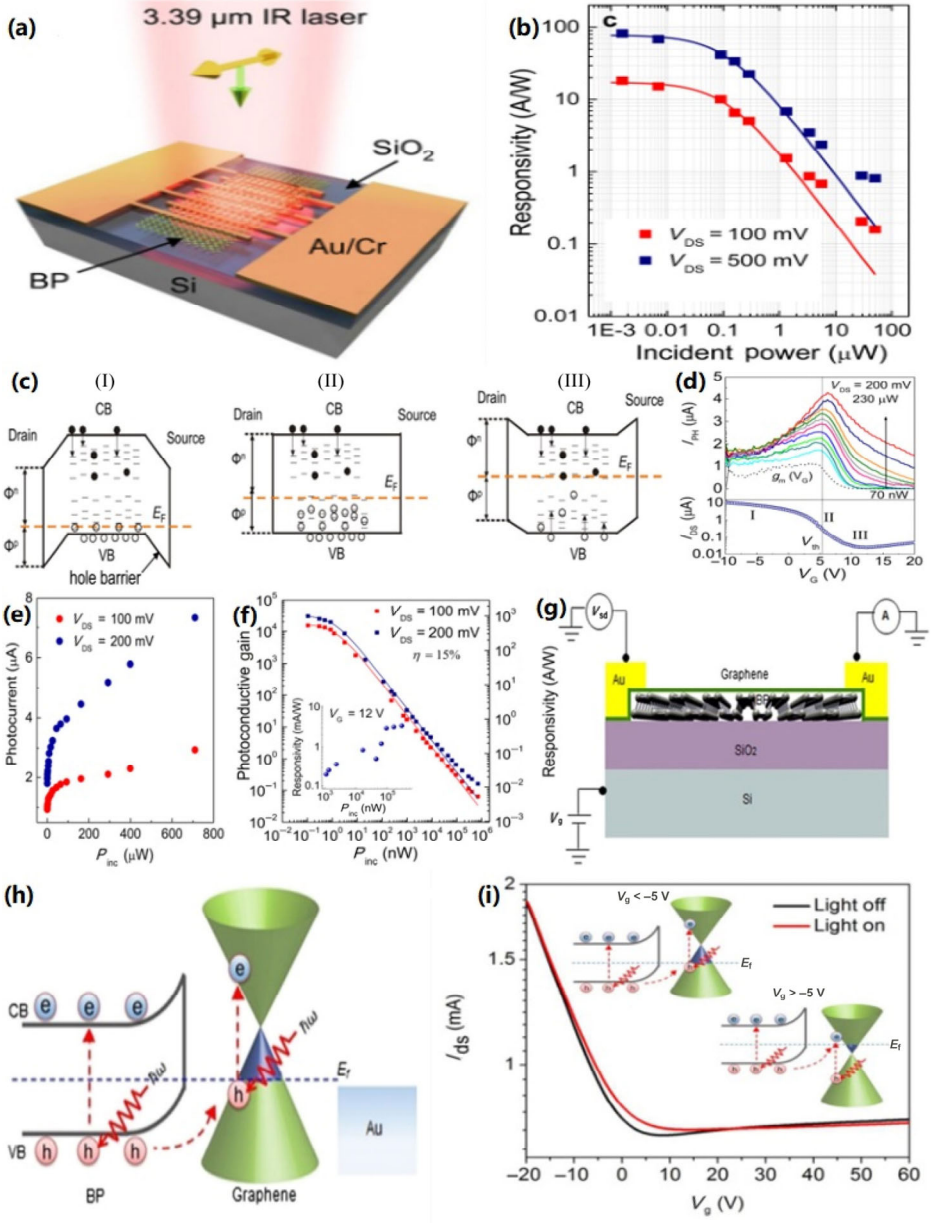

Figure 7 The photodetectors based on phosphorene. (a) The schematic diagram of the IR phosphorene photodetector. (b) V_{ds} is 100 and 500 mV, respectively, the variation curve of R with incident light power. (c) The energy band of the photodetector for (I) $V_g < V_{th}$, (II) $V_g \approx V_{th}$ and (III) $V_g > V_{th}$. (d) Upper panel: the variation curve of photocurrent with incident light power; down panel: transistor transfer characteristic curve of V_{ds} = 200 mV. (e) The relation diagram of R and incident light power of V_{ds} is 100 and 200 mV, respectively. (f) Variation curve of photoconductive gain with incident optical power of V_{ds} is 100 and 200 mV, respectively. Inset: V_g = 12 V, the relation graph of the photoconductive gain and the incident light power (adapted with permission from Ref. [396], © American Chemical Society 2016). (g) The schematic diagram of graphene-phosphorene heterojunction photodetector. (h) The band diagram of graphene-phosphorene heterojunction. Photoexcited hot carrier transport under zero V_g and illumination. (i) The transfer curve of graphene-phosphorene photodetector under the presence and absence of light (adapted with permission from Ref. [112], © American Chemical Society 2017).

with the change curve of the incident light power. When V_g = 3 V, the PGE is significantly reduced as photoresponse at higher incident light power. The maximum R is 82 A/W at a bias of 500 mV and incident light power of 1.6 nW. The photodetector is mainly operated by PGE, as shown in Figs. 7(a)–7(f). In addition, Liu et al. reported a graphene-phosphorene heterojunction photodetector with ultra-high R and long-term stability at an IR light wavelength, the structure of which is shown in Fig. 7(g) [112]. Under illumination, due to the presence of a built-in electric field between the phosphorene and the graphene, the phosphorene film generates a photo-generated electron or a hole pair, and the holes are transferred to the graphene, so that the electrons are still trapped in the phosphorene film. Thus, the phosphorene layer accumulates a large amount of negative charge and attracts more holes in the graphene, and the trapped photo-generated carriers work as a local gate, that is the PGE, thus the phototransistor requires a higher V_g to reach the neutral point (Figs. 7(h)–7(i)).

4.3 PVE

The PVE is based on the built-in electric field in the semiconductor, which separates the photo-generated carriers under the action of the built-in electric field, and promotes the photo-generated electrons and holes to move in the opposite direction. Photodetectors based on the principle of PVE is often called photodiode. It usually contains p-n photodiode formed by two kinds of semiconductor with opposite doping type and metal-semiconductor photodiode or semiconductor-semiconductor photodiode with Schottky barrier [355]. There are two advantages of the PVE. Firstly, the build-in electric field supplies the power, not needing the external circuit, which is benefit to save the energy resource and fit for lower power consumption system. Secondly, dark current is relatively lower, and the on/off ratio is relatively higher. With regard to the disadvantage of the PVE, it can be summarized to two points. To begin with, building the heterojunction is necessary for the photodetectors based on PVE, which directly brings about the sophisticated construction for the devices. Besides, lower R always exists in the photodetectors based on PVE [5, 6, 355].

For example, Liu et al. reported an Al-doped phosphorene homogeneous diode and the schematic diagram is shown in Fig. 8(a) [397]. Due to the built-in electric field at the p-n junction, the photo-generated carriers are effectively separated. During operation, no external bias voltage is applied and high-performance NIR PVE is generated. When the diode works, the recombination probability of photo-generated electron-hole is greatly reduced, which are better than those of photodetectors based on PCE (Figs. 8(a)–8(d)). Wang et al. prepared a high-performance self-powered UV–Vis broadband photodiode based on n-CdS/p-Se heterojunction and the structure is shown in Fig. 8(e) [398]. Based on the strong electric field and good contact produced by CdS/Se heterojunction, the photodiode produces obvious broadband optical response through PVE without external bias voltage (Figs. 8(f)–8(h)).

The above is about p-n photodiode based on PVE, and the following is about Schottky barrier photodiode based on PVE. Long et al. reported a LWIR photodetector based on black arsenic phosphorus/metal Schottky junction and the structure is shown in Fig. 8(i) [399]. Through the black arsenic phosphorus/metal Schottky junction, the electron-hole pair produced by light is separated on the junction surface of the photodetector, thus generating photocurrent (Figs. 8(j)–8(l)).

4.4 PTE

When nonuniform light is irradiated on semiconductors, the temperature gradient and temperature difference ΔT are produced at both sides of semiconductors due to light radiation, which is called PTE. According to Seebeck effect, the temperature difference leads to different voltage, which is photothermoelectric voltage V_{PTE}. The photothermoelectric voltage V_{PTE} is expressed by the formula $V_{PTE} = (S_1 - S_2)\cdot\Delta T$, where S_1, S_2 is the Seebeck coefficient of the two semiconductors. Due to the difference of thermoelectric voltage, photocurrent can also be generated at zero bias voltage [400, 401]. As for the advantage of the PTE, there are two points. Firstly, the corresponding photodetectors can detect IR range at room temperature. Secondly, the photodetectors based on PTE are cheaper than those of commercial IR photodetectors. The disadvantage of the PTE lies in that photodetectors are usually sensitive to environmental temperature and exhibit relatively lower R to UV and Vis range [5, 6, 355].

For example, Yuan et al. reported a polarization-sensitive broadband phosphorene photodetector based on vertical p-n junction, the structure of which is shown in Fig. 8(m) [402]. The photodetector operates based on two effects. The PTE plays a leading role in the photocurrent generation at the zero-source voltage and low V_{sd}. At the high V_{sd}, the PVE begins to take a leading role in the generation of the photocurrent (Figs. 8(n) and 8(o)). The black arsenic phosphorus based LWIR photodetector reported by Long et al. which was mentioned earlier, also works on the basis of PTE [399]. The photodetector has the advantages of good broadband and high response, fast speed and ultra-high speed anisotropic photoresponse.

4.5 How to distinguish these mechanisms?

The applied bias voltage is 0 V, if photocurrent is generated, it is PVE. The applied bias voltage is 0 V, if no photocurrent is generated, and then, please look at the transfer curve. Under illumination, if shifting appears in the transfer curve, it is PGE. If no shifting appears in the transfer curve, it is PCE. Under illumination, the current polarity exhibits change with the slow movement of the light spot from source to drain, it is PTE [5, 6, 355].

5 Summary and prospect

In this paper, based on the novel 2D single element materials-Xenes, the types of 2D-Xenes materials are introduced, and then their preparation methods are introduced. Finally, the working mechanisms of photodetectors based on 2D-Xenes materials are summarized. 2D-Xenes materials have many excellent properties such as high carrier mobility, layer-dependent bandgap, QSHE, SOC, topological properties, which make it possible to be widely used in photodetectors. At present, there are few studies on the photodetectors fabricated by 2D-Xenes materials, and the researchers are still trying to explore the applications of 2D-Xenes materials in the field of photodetectors. Because the researchers' reports on these 2D-Xenes materials are not deep enough, phosphorene is currently the most widely used in the field of photodetectors in these 2D-Xenes materials, while other materials are rarely used in the field of photodetectors.

According to the distribution of periodic table, these 2D-Xenes materials are mainly concentrated in group III, IV, V and VI. Borophene and gallenene are in group III; silicene, germanene, stanene and plumbene are in group IV; phosphorene, arsenene, antimonene and bismuthene are in group V; selenene and tellurene are in group VI. Among them, borophene has both non-metal properties and metal properties, and has large optical anisotropy. Besides, boron nanosheets have the

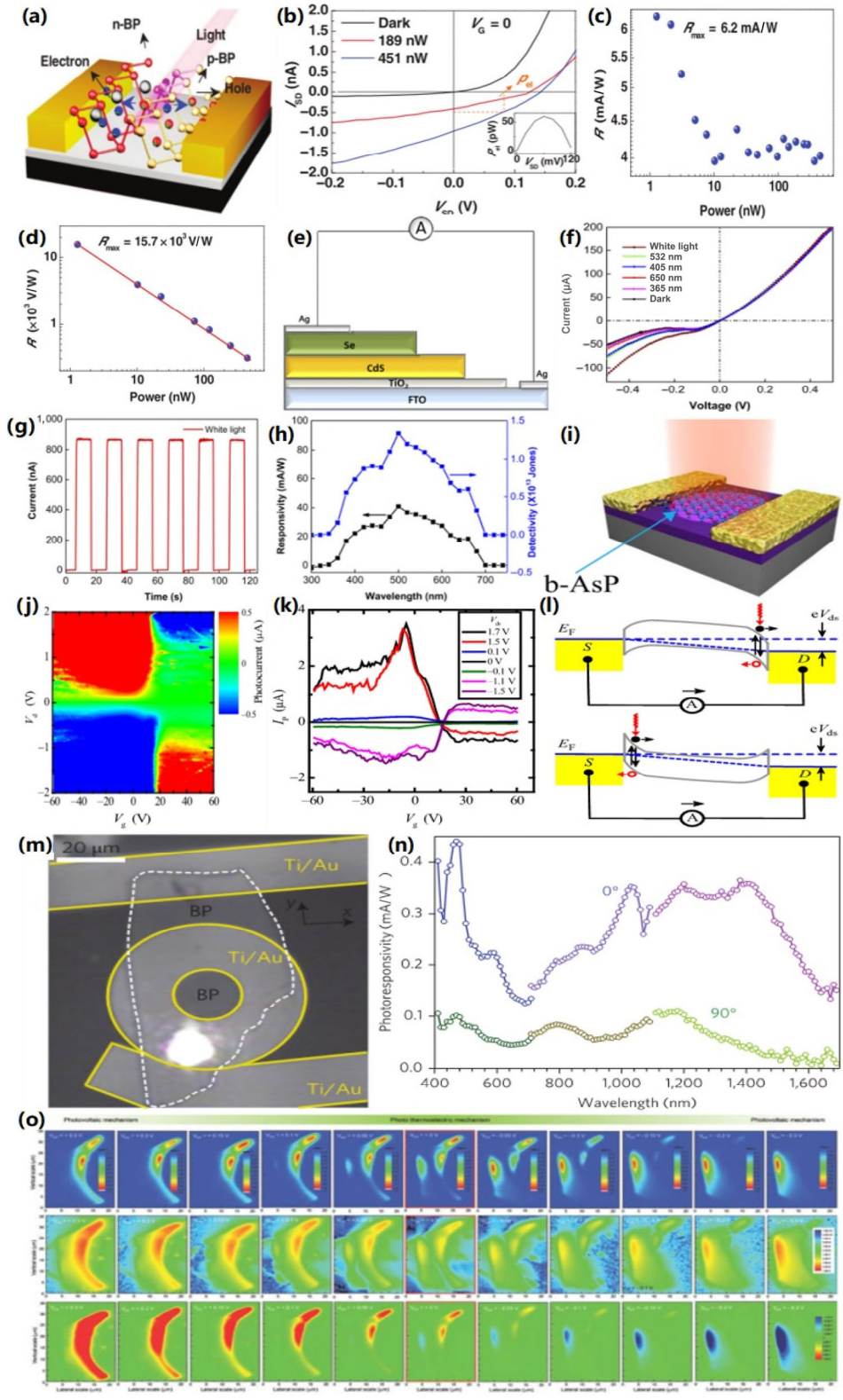

Figure 8 The photodetectors based on phosphorene. (a) The schematic diagram of the Al-doped phosphorene homogeneous diode. (b) The measurement curves of I_{sd} and V_{sd} in dark and light, respectively. (c) and (d) The function curve of R and incident light power (adapted with permission from Ref. [397], © WILEY-VCH Verlag GmbH & Co. KGaA, Weinheim 2017). (e) The schematic diagram of self-powered UV–Vis n-CdS/p-Se heterojunction broadband photodiode. (f) The schematic diagram of n-Cd/p-Se heterojunction photodiode at −0.5–0.5 V in dark and different light, respectively. (g) The time response of the device at zero bias in the white light illumination of 1 mW/cm^2. (h) R and D^* of the device at zero bias (adapted with permission from Ref. [398], © Author(s) 2018). (i) The schematic diagram of the LWIR photodetector based on black arsenic phosphorus/metal Schottky junction. (j) The schematic diagram of photocurrent under the function relationship of V_{ds} and V_g. (k) The schematic diagram of photocurrent and V_g at different bias voltages. (l) The energy structure schematic diagram of different doping types under zero bias voltage. Upper half: the device that works in P-type area. Bottom plate: the device that works in n-type area. The black horizontal arrow indicates the direction of the photocurrent caused by PVE (adapted with permission from Ref. [399], © The Authors, some rights reserved; exclusive licensee American Association for the Advancement of Science 2017). (m) The optical image of BP photodetector with an annular photocurrent collector. (n) The polarization dependence of the R of the BP sheet with the light illumination at the wavelength of 400–1,700 nm. (o) The photocurrent generation mechanism of the BP photodetector is determined by the photocurrent diagram of V_{ds} (adapted with permission from Ref. [402], © Macmillan Publishers Limited 2015).

characteristics of high crystallization, free of trap state, low electron-hole pair recombination barriers and so on. These excellent properties indicate that borophene has great applications in electronic and optoelectronics. However, borophene is not stable enough in air, so there is a method of hydrogenation to saturate hanging bonds, such as hydrogenated borophene. Some studies have shown that hydrogenated borophene has good current limiting effect and strong electron anisotropy. In addition, it can produce large photocurrent under light, so it can be greatly applied in the field of photodetectors. Gallenene has light carrier and high mobility, which indicates that gallium can also be used in photodetectors. In the group III, there are aluminum, indium, thallium and other elements, their single element 2D materials have not yet been developed. Based on the excellent optical properties of borophene and gallenene, single element 2D materials such as aluminum, indium and thallium are expected to be developed by researchers and widely used in photodetectors. The structures of silicene, germanene, stanene and plumbene are similar to those of graphene hexagonal honeycomb, and all of them have QSHE and strong SOC, and show nontrivial electronic state in topology. These excellent properties make them have important applications in the field of photodetectors. In the group V, phosphorene has many excellent properties, such as high carrier mobility, in-plane high anisotropy and tunable bandgap related to the number of layers, which makes phosphorene widely used in optoelectronics. Arsenene, antimonene and bismuthene all have high carrier mobility and broad bandgap, which is very important for broadband photoresponse, so arsenene, antimonene and bismuthene are expected to be widely applied to photodetectors. In the group VI, the SOC of selenene and tellurene opens up a large bandgap for them, and their TIs have nontrivial edge states. Thus, they are promising novel electronic and spin electron application materials, which are expected to be widely used in the field of photodetectors.

In the future, the application of these 2D-Xenes materials in the field of photodetectors is still a great challenge. First of all, the preparation methods of these 2D-Xenes materials are still relatively limited and are not produced in a large area, so it is necessary to develop a method that can produce high quality and large area 2D-Xenes materials. Secondly, some 2D-Xenes materials have very high chemical reaction activity and are easy to be oxidized in air, which makes it difficult to characterize the materials, so it is necessary to provide some methods to protect them from oxidation. Based on these 2D-Xenes materials, the fabrication process of photodetectors also needs to be explored constantly, which involves many problems such as device cost, mass production, stability and high quality. These emerging difficulties need to be solved by a lot of experiments and long-term researches.

Generally speaking, the research of photodetectors based on 2D-Xenes materials still needs to be explored. Through these novel 2D-Xenes materials, we construct photodetectors with different structures, such as homogeneous junction, heterojunction or Schottky junction, which can be used to improve R, internal and EQE, stability and D^*, expand the wavelength range of photoresponse, shorten the photoresponse time, and finally achieve high-performance photodetectors. Finally, the research of 2D-Xenes materials will continue, and it is believed that these materials will play an inestimable role in the preparation of new high-performance photodetectors in the future.

Acknowledgements

The research was partially supported by the Financial supports from the Science and Technology Development Fund (Nos. 007/2017/A1 and 132/2017/A3), Macao Special Administration Region (SAR), China, and the National Natural Science Foundation of China (Nos. 61875138, 61435010, and 61961136001), Guangdong Natural Science Foundation of China (No. 2019A1515010007) and Science, and Technology Innovation Commission of Shenzhen (Nos. JCYJ20190808175605495 and JCYJ20170811093453105). Authors also acknowledge the support from Instrumental Analysis Center of Shenzhen University (Xili Campus).

References

[1] Buscema, M.; Island, J. O.; Groenendijk, D. J.; Blanter, S. I.; Steele, G. A.; van der Zant, H. S. J.; Castellanos-Gomez, A. Photocurrent generation with two-dimensional van der Waals semiconductors. *Chem. Soc. Rev.* **2015**, *44*, 3691–3718.

[2] Ankah, G. N.; Büchele, P.; Poulsen, K.; Rauch, T.; Tedde, S. F.; Gimmler, C.; Schmidt, O.; Kraus, T. PbS quantum dot based hybrid-organic photodetectors for X-ray sensing. *Org. Electron.* **2016**, *33*, 201–206.

[3] Teng, F.; Hu, K.; Ouyang, W. X.; Fang, X. S. Photoelectric detectors based on inorganic p-type semiconductor materials. *Adv. Mater.* **2018**, *30*, 1706262.

[4] Long, M. S.; Wang, P.; Fang, H. H.; Hu, W. D. Progress, challenges, and opportunities for 2D material based photodetectors. *Adv. Funct. Mater.***2019**, *29*, 1803807.

[5] Koppens, F. H. L.; Mueller, T.; Avouris, P.; Ferrari, A. C.; Vitiello, M. S.; Polini, M. Photodetectors based on graphene, other two-dimensional materials and hybrid systems. *Nat.Nanotechnol.* **2014**, *9*, 780–793.

[6] Xie, C.; Yan, F. Flexible photodetectors based on novel functional materials. *Small* **2017**, *13*, 1701822.

[7] Wang, B.; Zhong, S. P.; Zhang, Z. B.; Zheng, Z. Q.; Zhang, Y. P.; Zhang, H. Broadband photodetectors based on 2D group IV_A metal chalcogenides semiconductors. *Appl. Mater. Today* **2019**, *15*, 115–138.

[8] Chen, H. Y.; Liu, H.; Zhang, Z. M.; Hu, K.; Fang, X. S. Nanostructured photodetectors: From ultraviolet to terahertz. *Adv. Mater.* **2016**, *28*, 403–433.

[9] Zhuge, F. W.; Zheng, Z.; Luo, P.; Lv, L.; Huang, Y.; Li, H. Q.; Zhai, T. Y. Nanostructured materials and architectures for advanced infrared photodetection. *Adv. Mater. Technol.* **2017**, *2*, 1700005.

[10] Su, L. X.; Yang, W.; Cai, J.; Chen, H. Y.; Fang, X. S. Self-powered ultraviolet photodetectors driven by built-in electric field. *Small* **2017**, *13*, 1701687.

[11] Wang, G. Y.; Zhang, Y. Z.; You, C. Y.; Liu, B. Y.; Yang, Y. H.; Li, H. J. W.; Cui, A. J.; Liu, D. M.; Yan, H. Two dimensional materials based photodetectors. *Infrared Phys. Technol.* **2018**, *88*, 149–173.

[12] Novoselov, K. S.; Jiang, D.; Schedin, F.; Booth, T. J.; Khotkevich, V. V.; Morozov, S. V.; Geim, A. K. Two-dimensional atomic crystals. *Proc. Natl. Acad. Sci. USA* **2005**, *102*, 10451–10453.

[13] Wang, Q. H.; Kalantar-Zadeh, K.; Kis, A.; Coleman, J. N.; Strano, M. S. Electronics and optoelectronics of two-dimensional transition metal dichalcogenides. *Nat. Nanotechnol.* **2012**, *7*, 699–712.

[14] Zhou, Y. H.; An, H. N.; Gao, C.; Zheng, Z. Q.; Wang, B. UV–Vis–NIR photodetector based on monolayer MoS_2. *Mater. Lett.* **2019**, *237*, 298–302.

[15] Zhou, Y. H.; Zhang, Z. B.; Xu, P.; Zhang, H.; Wang, B. UV–Visible photodetector based on i-type heterostructure of ZnO-QDs/monolayer MoS_2. *Nanoscale Res. Lett.* **2019**, *14*, 364.

[16] Zheng, Z. Q.; Yao, J. D.; Wang, B.; Yang, G. W. A flexible, transparent and high-performance gas sensor based on layer-materials for wearable technology. *Nanotechnology* **2017**, *28*, 415501.

[17] Zheng, Z. Q.; Yao, J. D.; Wang, B.; Yang, Y. B.; Yang, G. W.; Li, J. B. Self-assembly high-performance UV–Vis–NIR broadband β-In_2Se_3/si photodetector array for weak signal detection. *ACS Appl. Mater. Interfaces* **2017**, *9*, 43830–43837.

[18] Wang, B.; Jin, H. T.; Zheng, Z. Q.; Zhou, Y. H.; Gao, C. Low-temperature and highly sensitive C_2H_2 sensor based on Au decorated ZnO/In_2O_3 belt-tooth shape nano-heterostructures. *Sens. Actuators B Chem.* **2017**, *244*, 344–356.

[19] Zheng, Z. Q.; Jin, H. T.; Ouyang, G.; Wang, B. Field emission and growth mechanism of ZnO microrods array with nanospikes fabricated by thermal evaporation. *Mater. Lett.* **2016**, *170*, 210–212.
[20] Zheng, Z. Q.; Yao, J. D.; Wang, B.; Yang, G. W. Light-controlling, flexible and transparent ethanol gas sensor based on ZnO nanoparticles for wearable devices. *Sci. Rep.* **2015**, *5*, 11070.
[21] Zheng, Z. Q.; Wang, B.; Yao, J. D.; Yang, G. W. Light-controlled C_2H_2 gas sensing based on Au–ZnO nanowires with plasmon-enhanced sensitivity at room temperature. *J. Mater. Chem. C* **2015**, *3*, 7067–7074.
[22] Zheng, Z. Q.; Zhu, L. F.; Wang, B. In_2O_3 nanotower hydrogen gas sensors based on both schottky junction and thermoelectronic emission. *Nanoscale Res. Lett.* **2015**, *10*, 293.
[23] Wang, B.; Jin, X.; Wu, H. Y.; Zheng, Z. Q.; Ouyang, Z. B. 3D resonator based on luminescence enhanced by both polarized, size-dependent whispering gallery modes and Fabry–Pérot waveguide modes in individual ZnO micro-and nanonails. *Nanoscale* **2014**, *6*, 5338–5342.
[24] Wang, B.; Zheng, Z. Q.; Zhu, L. F.; Yang, Y. H.; Wu, H. Y. Self-assembled and Pd decorated Zn_2SnO_4/ZnO wire-sheet shape nano-heterostructures networks hydrogen gas sensors. *Sens. Actuators B Chem.* **2014**, *195*, 549–561.
[25] Wang, B.; Zheng, Z. Q.; Wu, H. Y.; Zhu, L. F. Field emission properties and growth mechanism of In_2O_3 nanostructures. *Nanoscale Res. Lett.* **2014**, *9*, 111.
[26] Wang, B.; Jin, X.; Ouyang, Z. B.; Xu, P. Field emission properties originated from 2D electronics gas successively tunneling for 1D heterostructures of ZnO nanobelts decorated with In_2O_3 nanoteeth. *J. Nanopart. Res.* **2012**, *14*, 1008.
[27] Wang, B.; Jin, X.; Ouyang, Z. B. Synthesis, characterization and cathodoluminescence of self-assembled 1D ZnO/In_2O_3 nano-heterostructures. *Crystengcomm* **2012**, *14*, 6888–6903.
[28] Wang, B.; Jin, X.; Wu, H. Y.; Zheng, Z. Q. Whispering gallery and Fabry–Pérot modes enhanced luminescence from individual ZnO micro mushroom. *J. Appl. Phys.* **2013**, *113*, 034313.
[29] Wang, B.; Wu, H. Y.; Zheng, Z. Q.; Yang, Y. H. Field emission and photoluminescence of ZnO nanocombs. *Appl. Phys. A* **2013**, *113*, 549–556.
[30] Wang, B.; Jin, X.; Ouyang, Z. B.; Xu, P. Photoluminescence and field emission of 1D ZnO nanorods fabricated by thermal evaporation. *Appl. Phys. A* **2012**, *108*, 195–200.
[31] Wang, B.; Li, I. L.; Xu, P.; Xing, L. W. Fabrication and photoluminescence of the SnO_2 plate-shape nanostructures and chrysanthemum-shape nanostructures. *Rev. Adv. Mater. Sci.* **2013**, *33*, 164–170.
[32] Xu, M. S.; Liang, T.; Shi, M. M.; Chen, H. Z. Graphene-like two-dimensional materials. *Chem. Rev.* **2013**, *113*, 3766–3798.
[33] Chimene, D.; Alge, D. L.; Gaharwar, A. K. Two-dimensional nanomaterials for biomedical applications: Emerging trends and future prospects. *Adv. Mater.* **2015**, *27*, 7261–7284.
[34] Zhang, H. Ultrathin two-dimensional nanomaterials. *ACS Nano* **2015**, *9*, 9451–9469.
[35] Novoselov, K. S.; Geim, A. K.; Morozov, S. V.; Jiang, D.; Zhang, Y.; Dubonos, S. V.; Grigorieva, I. V.; Firsov, A. A. Electric field effect in atomically thin carbon films. *Science* **2004**, *306*, 666–669.
[36] Bao, Q. L.; Zhang, H.; Wang, Y.; Ni, Z. H.; Yan, Y. L.; Shen, Z. X.; Loh, K. P.; Tang, D. Y. Atomic-layer graphene as a saturable absorber for ultrafast pulsed lasers. *Adv. Funct. Mater.* **2009**, *19*, 3077–3083.
[37] Bao, Q. L.; Zhang, H.; Wang, B.; Ni, Z. H.; Lim, C. H. Y. X.; Wang, Y.; Tang, D. Y.; Loh, K. P. Broadband graphene polarizer. *Nat. Photonics* **2011**, *5*, 411–415.
[38] Zhang, H.; Bao, Q. L.; Tang, D. Y.; Zhao, L. M.; Loh, K. Large energy soliton erbium-doped fiber laser with a graphene-polymer composite mode locker. *Appl. Phys. Lett.* **2009**, *95*, 141103.
[39] Zhang, H.; Tang, D. Y.; Zhao, L. M.; Bao, Q. L.; Loh, K. P. Large energy mode locking of an erbium-doped fiber laser with atomic layer graphene. *Opt. Express* **2009**, *17*, 17630–17635.
[40] Zhang, H.; Tang, D. Y.; Knize, R. J.; Zhao, L. M.; Bao, Q. L.; Loh, K. P. Graphene mode locked, wavelength-tunable, dissipative soliton fiber laser. *Appl. Phys. Lett.* **2010**, *96*, 111112.
[41] Zhang, H.; Virally, S.; Bao, Q. L.; Ping, L. K.; Massar, S.; Godbout, N.; Kockaert, P. Z-scan measurement of the nonlinear refractive index of graphene. *Opt. Lett.* **2012**, *37*, 1856–1858.
[42] Bao, Q. L.; Zhang, H.; Yang, J. X.; Wang, S.; Tang, D. Y.; Jose, R.; Ramakrishna, S.; Lim, C. T.; Loh, K. P. Graphene-polymer nanofiber membrane for ultrafast photonics. *Adv. Funct. Mater.* **2010**, *20*, 782–791.
[43] Bao, Q. L.; Zhang, H.; Ni, Z. H.; Wang, Y.; Polavarapu, L.; Shen, Z. X.; Xu, Q. H.; Tang, D. Y.; Loh, K. P. Monolayer graphene as a saturable absorber in a mode-locked laser. *Nano Res.* **2011**, *4*, 297–307.
[44] Zhang, H.; Tang, D. Y.; Zhao, L. M.; Bao, Q. L.; Loh, K. P.; Lin, B.; Tjin, S. C. Compact graphene mode-locked wavelength-tunable erbium-doped fiber lasers: From all anomalous dispersion to all normal dispersion. *Laser Phys. Lett.* **2010**, *7*, 591–596.
[45] Zheng, Z. W.; Zhao, C. J.; Lu, S. B.; Chen, Y.; Li, Y.; Zhang, H.; Wen, S. C. Microwave and optical saturable absorption in graphene. *Opt. Express* **2012**, *20*, 23201–23214.
[46] Zhao, L. M.; Tang, D. Y.; Zhang, H.; Wu, X.; Bao, Q. L.; Loh, K. P. Dissipative soliton operation of an ytterbium-doped fiber laser mode locked with atomic multilayer graphene. *Opt. Lett.* **2010**, *35*, 3622–3624.
[47] Ponraj, J. S.; Xu, Z. Q.; Dhanabalan, S. C.; Mu, H. R.; Wang, Y. S.; Yuan, J.; Li, P. F.; Thakur, S.; Ashrafi, M.; Mccoubrey, K. et al. Photonics and optoelectronics of two-dimensional materials beyond graphene. *Nanotechnology* **2016**, *27*, 462001.
[48] Wang, Z. T.; Chen, Y.; Zhao, C. J.; Zhang, H.; Wen, S. C. Switchable dual-wavelength synchronously Q-switched erbium-doped fiber laser based on graphene saturable absorber. *IEEE Photonics J.* **2012**, *4*, 869–876.
[49] Song, Y. F.; Li, L.; Zhang, H.; Shen, D. Y.; Tang, D. Y.; Loh, K. P. Vector multi-soliton operation and interaction in a graphene mode-locked fiber laser. *Opt. Express* **2013**, *21*, 10010–10018.
[50] Zhang, H.; Tang, D. Y.; Zhao, L. M.; Bao, Q. L.; Loh, K. P. Vector dissipative solitons in graphene mode locked fiber lasers. *Opt. Commun.* **2010**, *283*, 3334–3338.
[51] Li, H. J.; Wang, L. L.; Zhang, H.; Huang, Z. R.; Sun, B.; Zhai, X.; Wen, S. C. Graphene-based mid-infrared, tunable, electrically controlled plasmonic filter. *Appl. Phys. Express* **2014**, *7*, 024301.
[52] Song, Y. F.; Zhang, H.; Tang, D. Y.; Shen, D. Y. Polarization rotation vector solitons in a graphene mode-locked fiber laser. *Opt. Express* **2012**, *20*, 27283–27289.
[53] Miao, L. L.; Jiang, Y. Q.; Lu, S. B.; Shi, B. X.; Zhao, C. J.; Zhang, H.; Wen, S. C. Broadband ultrafast nonlinear optical response of few-layers graphene: Toward the mid-infrared regime. *Photonics Res.* **2015**, *3*, 214–219.
[54] Zheng, G. P.; Chen, Y.; Huang, H. H.; Zhao, C. J.; Lu, S. B.; Chen, S. Q.; Zhang, H.; Wen, S. C. Improved transfer quality of CVD-grown graphene by ultrasonic processing of target substrates: Applications for ultra-fast laser photonics. *ACS Appl. Mater. Interfaces* **2013**, *5*, 10288–10293.
[55] Wang, Z. T.; Zou, Y. H.; Chen, Y.; Wu, M.; Zhao, C. J.; Zhang, H.; Wen, S. C. Graphene sheet stacks for Q-switching operation of an erbium-doped fiber laser. *Laser Phys. Lett.* **2013**, *10*, 075102.
[56] Chen, X.; Wang, Y.; Xiang, Y. J.; Jiang, G. B.; Wang, L. L.; Bao, Q. L.; Zhang, H.; Liu, Y.; Wen, S. C.; Fan, D. Y. A broadband optical modulator based on a graphene hybrid plasmonic waveguide. *J. Lightw. Technol.* **2016**, *34*, 4948–4953.
[57] Shivananju, B. N.; Bao, X. Z.; Yu, W. Z.; Yuan, J.; Mu, H. R.; Sun, T.; Xue, T. Y.; Zhang, Y. P.; Liang, Z. Z.; Kan, R. F.et al. Graphene heterostructure integrated optical fiber Bragg grating for light motion tracking and ultrabroadband photodetection from 400 nm to 10.768 μm. *Adv. Funct. Mater.* **2019**, *29*, 1807274.
[58] Mu, H. R.; Wang, Z. T.; Yuan, J.; Xiao, S.; Chen, C. Y.; Chen, Y.; Chen, Y.; Song, J. C.; Wang, Y. S.; Xue, Y. Z.et al. Graphene-Bi_2Te_3 heterostructure as saturable absorber for short pulse generation. *ACS Photonics* **2015**, *2*, 832–841.
[59] Han, M. M.; Zhang, S. M.; Li, X. L.; Zhang, H. X.; Yang, H.; Yuan, T. Polarization dynamic patterns of vector solitons in a graphene mode-locked fiber laser. *Opt. Express* **2015**, *23*, 2424–2435.
[60] Song, Y. F.; Liang, Z. M.; Zhang, H.; Zhang, Q.; Zhao, L. M.; Shen, D. Y.; Tang, D. Y. Period-doubling and quadrupling bifurcation of vector soliton bunches in a graphene mode locked fiber laser. *IEEE Photonics J.* **2017**, *9*, 4502308.

[61] Castro Neto, A. H.; Guinea, F.; Peres, N. M. R.; Novoselov, K. S.; Geim, A. K. The electronic properties of graphene. *Rev. Mod. Phys.* **2009**, *81*, 109–162.
[62] Kim, K.; Choi, J. Y.; Kim, T.; Cho, S. H.; Chung, H. J. A role for graphene in silicon-based semiconductor devices. *Nature* **2011**, *479*, 338–344.
[63] Bolotin, K. I.; Sikes, K. J.; Jiang, Z.; Klima, M.; Fudenberg, G.; Hone, J.; Kim, P.; Stormer, H. L. Ultrahigh electron mobility in suspended graphene. *Solid State Commun.* **2008**, *146*, 351–355.
[64] Novoselov, K. S.; Fal'ko, V. I.; Colombo, L.; Gellert, P. R.; Schwab, M. G.; Kim, K. A roadmap for graphene. *Nature* **2012**, *490*, 192–200.
[65] Zhang, Y. P.; Wu, Z. X.; Cao, Y. Y.; Zhang, H. Y. Optical properties of one-dimensional Fibonacci quasi-periodic graphene photonic crystal. *Opt. Commun.* **2015**, *338*, 168–173.
[66] Du, X.; Skachko, I.; Duerr, F.; Luican, A.; Andrei, E. Y. Fractional quantum Hall effect and insulating phase of Dirac electrons in graphene. *Nature* **2009**, *462*, 192–195.
[67] Nair, R. R.; Blake, P.; Grigorenko, A. N.; Novoselov, K. S.; Booth, T. J.; Stauber, T.; Peres, N. M. R.; Geim, A. K. Fine structure constant defines visual transparency of graphene. *Science* **2008**, *320*, 1308.
[68] Mueller, T.; Xia, F. N.; Freitag, M.; Tsang, J.; Avouris, P. Role of contacts in graphene transistors: A scanning photocurrent study. *Phys. Rev. B* **2009**, *79*, 245430.
[69] Mueller, T.; Xia, F. N.; Avouris, P. Graphene photodetectors for high-speed optical communications. *Nat. Photonics* **2010**, *4*, 297–301.
[70] Mak, K. F.; Shan, J. Photonics and optoelectronics of 2D semiconductor transition metal dichalcogenides. *Nat. Photonics* **2016**, *10*, 216–226.
[71] Kuc, A.; Zibouche, N.; Heine, T. Influence of quantum confinement on the electronic structure of the transition metal sulfide TS_2. *Phys. Rev. B* **2011**, *83*, 245213.
[72] Jiang, S. L.; Xie, C. Y.; Gu, Y.; Zhang, Q. H.; Wu, X. X.; Sun, Y. L.; Li, W.; Shi, Y. P.; Zhao, L. Y.; Pan, S. Y. et al. Anisotropic growth and scanning tunneling microscopy identification of ultrathin even-layered $PdSe_2$ ribbons. *Small* **2019**, *15*, 1902789.
[73] Kim, S.; Maassen, J.; Lee, J.; Kim, S. M.; Han, G.; Kwon, J.; Hong, S.; Park, J.; Liu, N.; Park, Y. C.et al. Interstitial Mo-assisted photovoltaic effect in multilayer $MoSe_2$phototransistors. *Adv. Mater.* **2018**, *30*, 1705542.
[74] Cao, G. Y.; Shang, A. X.; Zhang, C.; Gong, Y. P.; Li, S. J.; Bao, Q. L.; Li, X. F. Optoelectronic investigation of monolayer MoS_2/WSe_2 vertical heterojunction photoconversion devices. *Nano Energy* **2016**, *30*, 260–266.
[75] Zheng, W. H.; Jiang, Y.; Hu, X. L.; Li, H. L.; Zeng, Z. X. S.; Wang, X.; Pan, A. L. Light emission properties of 2D transition metal dichalcogenides: Fundamentals and applications. *Adv. Opt. Mater.* **2018**, *6*, 1800420.
[76] Tian, H.; Chin, M. L.; Najmaei, S.; Guo, Q. S.; Xia, F. N.; Wang, H.; Dubey, M. Optoelectronic devices based on two-dimensional transition metal dichalcogenides. *Nano Res.* **2016**, *9*, 1543–1560.
[77] Cao, G. Y.; An, Y. D.; Bao, Q. L.; Li, X. F. Physics and optoelectronic simulation of photodetectors based on 2D materials. *Adv. Opt. Mater.* **2019**, *7*, 1900410.
[78] Jiang, S. L.; Zhang, Z. P.; Zhang, N.; Huan, Y. H.; Gong, Y.; Sun, M. X.; Shi, J. P.; Xie, C. Y.; Yang, P. F.; Fang, Q. Y. et al. Application of chemical vapor-deposited monolayer $ReSe_2$ in the electrocatalytic hydrogen evolution reaction. *Nano Res.* **2018**, *11*, 1787–1797.
[79] Jiang, S. L.; Hong, M.; Wei, W.; Zhao, L. Y.; Zhang, N.; Zhang, Z. P.; Yang, P. F.; Gao, N.; Zhou, X. B.; Xie, C.Y. et al. Direct synthesis and *in situ* characterization of monolayer parallelogrammic rhenium diselenide on gold foil. *Commun. Chem.* **2018**, *1*, 17.
[80] Xie, Y.; Zhang, B.; Wang, S. X.; Wang, D.; Wang, A. Z.; Wang, Z. Y.; Yu, H. H.; Zhang, H. J.; Chen, Y. X.; Zhao, M. W. et al. Ultrabroadband MoS_2 photodetector with spectral response from 445 to 2,717 nm. *Adv. Mater.* **2017**, *29*, 1605972.
[81] Zhou, M.; Chen, X. B.; Li, M. L.; Du, A. J. Widely tunable and anisotropic charge carrier mobility in monolayer tin(II) selenide using biaxial strain: A first-principles study. *J. Mater. Chem. C* **2017**, *5*, 1247–1254.
[82] Takeda, K.; Shiraishi, K. Theoretical possibility of stage corrugation in Si and Ge analogs of graphite. *Phys. Rev. B* **1994**, *50*, 14916–14922.
[83] Ji, X. Y.; Kong, N.; Wang, J. Q.; Li, W. L.; Xiao, Y. L.; Gan, S. T.; Zhang, Y.; Li, Y. J.; Song, X. R.; Xiong, Q. Q.et al. A novel top-down synthesis of ultrathin 2D boron nanosheets for multimodal imaging-guided cancer therapy. *Adv. Mater.* **2018**, *30*, 1803031.
[84] Guzmán-Verri, G. G.; Voon, L. C. L. Y. Electronic structure of silicon-based nanostructures. *Phys. Rev. B* **2007**, *76*, 075131.
[85] Ni, Z. Y.; Liu, Q. H.; Tang, K. C.; Zheng, J. X.; Zhou, J.; Qin, R.; Gao, Z. X.; Yu, D. P.; Lu, J. Tunable bandgap in silicene and germanene. *Nano Lett.* **2012**, *12*, 113–118.
[86] Bianco, E.; Butler, S.; Jiang, S. S.; Restrepo, O. D.; Windl, W.; Goldberger, J. E. Stability and exfoliation of germanane: A germanium graphane analogue. *ACS Nano* **2013**, *7*, 4414–4421.
[87] Zhu, F. F.; Chen, W. J.; Xu, Y.; Gao, C. L.; Guan, D. D.; Liu, C. H.; Qian, D.; Zhang, S. C.; Jia, J. F. Epitaxial growth of two-dimensional stanene. *Nat. Mater.* **2015**, *14*, 1020–1025.
[88] Chen, Y.; Jiang, G. B.; Chen, S. Q.; Guo, Z. N.; Yu, X. F.; Zhao, C. J.; Zhang, H.; Bao, Q. L.; Wen, S. C.; Tang, D. Y. et al. Mechanically exfoliated black phosphorus as a new saturable absorber for both Q-switching and mode-locking laser operation. *Opt. Express* **2015**, *23*, 12823–12833.
[89] Sun, Z. B.; Xie, H. H.; Tang, S. Y.; Yu, X. F.; Guo, Z. N.; Shao, J. D.; Zhang, H.; Huang, H.; Wang, H. Y.; Chu, P. K. Ultrasmall black phosphorus quantum dots: Synthesis and use as photothermal agents. *Angew. Chem., Int. Ed.* **2015**, *54*, 11526–11530.
[90] Lu, S. B.; Miao, L. L.; Guo, Z. N.; Qi, X.; Zhao, C. J.; Zhang, H.; Wen, S. C.; Tang, D. Y.; Fan, D. Y. Broadband nonlinear optical response in multi-layer black phosphorus: An emerging infrared and mid-infrared optical material. *Opt. Express* **2015**, *23*, 11183–11194.
[91] Tao, W.; Zhu, X. B.; Yu, X. H.; Zeng, X. W.; Xiao, Q. L.; Zhang, X. D.; Ji, X. Y.; Wang, X. S.; Shi, J. J.; Zhang, H. et al. Black phosphorus nanosheets as a robust delivery platform for cancer theranostics. *Adv. Mater.* **2017**, *29*, 1603276.
[92] Luo, Z. C.; Liu, M.; Guo, Z. N.; Jiang, X. F.; Luo, A. P.; Zhao, C. J.; Yu, X. F.; Xu, W. C.; Zhang, H. Microfiber-based few-layer black phosphorus saturable absorber for ultra-fast fiber laser. *Opt. Express* **2015**, *23*, 20030–20039.
[93] Qin, Z. P.; Xie, G. Q.; Zhang, H.; Zhao, C. J.; Yuan, P.; Wen, S. C.; Qian, L. J. Black phosphorus as saturable absorber for the Q-switched Er: ZBLAN fiber laser at 2.8 μm. *Opt. Express* **2015**, *23*, 24713–24718.
[94] Mu, H. R.; Lin, S. H.; Wang, Z. C.; Xiao, S.; Li, P. F.; Chen, Y.; Zhang, H.; Bao, H. F.; Lau, S. P.; Pan, C. X.et al. Black phosphorus-polymer composites for pulsed lasers. *Adv. Opt. Mater.* **2015**, *3*, 1447–1453.
[95] Ma, J.; Lu, S. B.; Guo, Z. N.; Xu, X. D.; Zhang, H.; Tang, D. Y.; Fan, D. Y. Few-layer black phosphorus based saturable absorber mirror for pulsed solid-state lasers. *Opt. Express* **2015**, *23*, 22643–22648.
[96] Qiu, M.; Wang, D.; Liang, W. Y.; Liu, L. P.; Zhang, Y.; Chen, X.; Sang, D. K.; Xing, C. Y.; Li, Z. J.; Dong, B. Q. et al. Novel concept of the smart NIR-light-controlled drug release of black phosphorus nanostructure for cancer therapy. *Proc. Natl. Acad. Sci. USA* **2018**, *115*, 501–506.
[97] Xu, Y. H.; Wang, Z. T.; Guo, Z. N.; Huang, H.; Xiao, Q. L.; Zhang, H.; Yu, X. F. Solvothermal synthesis and ultrafast photonics of black phosphorus quantum dots. *Adv. Opt. Mater.* **2016**, *4*, 1223–1229.
[98] Jiang, Q. Q.; Xu, L.; Chen, N.; Zhang, H.; Dai, L. M.; Wang, S. Y. Facile synthesis of black phosphorus: An efficient electrocatalyst for the oxygen evolving reaction. *Angew. Chem., Int. Ed.* **2016**, *55*, 13849–13853.
[99] Dhanabalan, S. C.; Ponraj, J. S.; Guo, Z. N.; Li, S. J.; Bao, Q. L.; Zhang, H. Emerging trends in phosphorene fabrication towards next generation devices. *Adv. Sci.* **2017**, *4*, 1600305.
[100] Ren, X. H.; Zhou, J.; Qi, X.; Liu, Y. D.; Huang, Z. Y.; Li, Z. J.; Ge, Y. Q.; Dhanabalan, S. C.; Ponraj, J. S.; Wang, S. Y. et al. Few-layer black phosphorus nanosheets as electrocatalysts for highly efficient oxygen evolution reaction. *Adv. Energy Mater.* **2017**, *7*, 1700396.
[101] Xing, C. Y.; Jing, G. H.; Liang, X.; Qiu, M.; Li, Z. J.; Cao, R.; Li, X. J.; Fan, D. Y.; Zhang, H. Graphene oxide/black phosphorus nanoflake aerogels with robust thermo-stability and significantly enhanced photothermal properties in air. *Nanoscale* **2017**, *9*, 8096–8101.
[102] Zhou, Y.; Zhang, M. X.; Guo, Z. N.; Miao, L. L.; Han, S. T.; Wang, Z. Y.; Zhang, X. W.; Zhang, H.; Peng, Z. C. Recent advances in

black phosphorus-based photonics, electronics, sensors and energy devices. *Mater. Horiz.* **2017**, *4*, 997–1019.

[103] Du, J.; Zhang, M.; Guo, Z.; Chen, J.; Zhu, X.; Hu, G.; Peng, P.; Zheng, Z.; Zhang, H. Phosphorene quantum dot saturable absorbers for ultrafast fiber lasers. *Sci. Rep.* **2017**, *7*, 42357.

[104] Qiu, M.; Ren, W. X.; Jeong, T.; Won, M.; Park, G. Y.; Sang, D. K.; Liu, L. P.; Zhang, H.; Kim, J. S. Omnipotent phosphorene: A next-generation, two-dimensional nanoplatform for multidisciplinary biomedical applications. *Chem. Soc. Rev.* **2018**, *47*, 5588–5601.

[105] Zheng, J. L.; Yang, Z. H.; Si, C.; Liang, Z. M.; Chen, X.; Cao, R.; Guo, Z. N.; Wang, K.; Zhang, Y.; Ji, J. H. et al. Black phosphorus based all-optical-signal-processing: Toward high performances and enhanced stability. *ACS Photonics* **2017**, *4*, 1466–1476.

[106] Song, Y. F.; Chen, S.; Zhang, Q.; Li, L.; Zhao, L. M.; Zhang, H.; Tang, D. Y. Vector soliton fiber laser passively mode locked by few layer black phosphorus-based optical saturable absorber. *Opt. Express* **2016**, *24*, 25933–25942.

[107] Tang, X.; Liang, W. Y.; Zhao, J. L.; Li, Z. J.; Qiu, M.; Fan, T. J.; Luo, C. S.; Zhou, Y.; Li, Y.; Guo, Z. N. et al. Fluorinated phosphorene: Electrochemical synthesis, atomistic fluorination, and enhanced stability. *Small* **2017**, *13*, 1702739.

[108] Chen, X. H.; Xu, G. H.; Ren, X. H.; Li, Z. J.; Qi, X.; Huang, K.; Zhang, H.; Huang, Z. Y.; Zhong, J. X. A black/red phosphorus hybrid as an electrode material for high-performance Li-ion batteries and supercapacitors. *J. Mater. Chem. A* **2017**, *5*, 6581–6588.

[109] Pan, Y. Y.; Dan, Y.; Wang, Y. Y.; Ye, M.; Zhang, H.; Quhe, R. G.; Zhang, X. Y.; Li, J. Z.; Guo, W. L.; Yang, L. et al. Schottky barriers in bilayer phosphorene transistors. *ACS Appl. Mater. Interfaces* **2017**, *9*, 12694–12705.

[110] Qiu, M.; Sun, Z. T.; Sang, D. K.; Han, X. G.; Zhang, H.; Niu, C. M. Current progress in black phosphorus materials and their applications in electrochemical energy storage. *Nanoscale* **2017**, *9*, 13384–13403.

[111] Zheng, J. L.; Tang, X.; Yang, Z. H.; Liang, Z. M.; Chen, Y. X.; Wang, K.; Song, Y. F.; Zhang, Y.; Ji, J. H.; Liu, Y. et al. Few-layer phosphorene-decorated microfiber for all-optical thresholding and optical modulation. *Adv. Opt. Mater.* **2017**, *5*, 1700026.

[112] Liu, Y.; Shivananju, B. N.; Wang, Y. S.; Zhang, Y. P.; Yu, W. Z.; Xiao, S.; Sun, T.; Ma, W. L.; Mu, H. R.; Lin, S. H. et al. Highly efficient and air-stable infrared photodetector based on 2D layered graphene-black phosphorus heterostructure. *ACS Appl. Mater. Interfaces* **2017**, *9*, 36137–36145.

[113] Wang, Z. T.; Xu, Y. H.; Dhanabalan, S. C.; Sophia, J.; Zhao, C. J.; Xu, C. W.; Xiang, Y. J.; Li, J. Q.; Zhang, H. Black phosphorus quantum dots as an efficient saturable absorber for bound soliton operation in an erbium doped fiber laser. *IEEE Photonics J.* **2016**, *8*, 1503310.

[114] Pawliszewska, M.; Ge, Y. Q.; Li, Z. J.; Zhang, H.; Sotor, J. Fundamental and harmonic mode-locking at 2.1 μm with black phosphorus saturable absorber. *Opt. Express* **2017**, *25*, 16916–16921.

[115] Xu, Y. H.; Jiang, X. F.; Ge, Y. Q.; Guo, Z. N.; Zeng, Z. K.; Xu, Q. H.; Zhang, H.; Yu, X. F.; Fan, D. Y. Size-dependent nonlinear optical properties of black phosphorus nanosheets and their applications in ultrafast photonics. *J. Mater. Chem. C* **2017**, *5*, 3007–3013.

[116] Liu, J. J.; Liu, J.; Guo, Z. N.; Zhang, H.; Ma, W. W.; Wang, J. Y.; Su, L. B. Dual-wavelength Q-switched Er: SrF_2 laser with a black phosphorus absorber in the mid-infrared region. *Opt. Express* **2016**, *24*, 30289–30295.

[117] Yin, F.; Hu, K.; Chen, S.; Wang, D. Y.; Zhang, J. N.; Xie, M. S.; Yang, D.; Qiu, M.; Zhang, H.; Li, Z. G. Black phosphorus quantum dot based novel siRNA delivery systems in human pluripotent teratoma PA-1 cells. *J. Mater. Chem. B* **2017**, *5*, 5433–5440.

[118] Xu, Y. H.; Wang, W. X.; Ge, Y. Q.; Guo, H. Y.; Zhang, X. J.; Chen, S.; Deng, Y. H.; Lu, Z. G.; Zhang, H. Stabilization of black phosphorous quantum dots in PMMA nanofiber film and broadband nonlinear optics and ultrafast photonics application. *Adv. Funct. Mater.* **2017**, *27*, 1702437.

[119] Luo, S. J.; Zhao, J. L.; Zou, J. F.; He, Z. L.; Xu, C. W.; Liu, F. W.; Huang, Y.; Dong, L.; Wang, L.; Zhang, H. Self-standing polypyrrole/black phosphorus laminated film: Promising electrode for flexible supercapacitor with enhanced capacitance and cycling stability. *ACS Appl. Mater. Interfaces* **2018**, *10*, 3538–3548.

[120] Ge, Y. Q.; Chen, S.; Xu, Y. J.; He, Z. L.; Liang, Z. M.; Chen, Y. X.; Song, Y. F.; Fan, D. Y.; Zhang, K.; Zhang, H. Few-layer selenium-doped black phosphorus: Synthesis, nonlinear optical properties and ultrafast photonics applications. *J. Mater. Chem. C* **2017**, *5*, 6129–6135.

[121] Tan, Y.; Guo, Z. N.; Ma, L. A.; Zhang, H.; Akhmadaliev, S.; Zhou, S. Q.; Chen, F. Q-switched waveguide laser based on two-dimensional semiconducting materials: Tungsten disulfide and black phosphorous. *Opt. Express* **2016**, *24*, 2858–2866.

[122] Xu, Y. J.; Yuan, J.; Zhang, K.; Hou, Y.; Sun, Q.; Yao, Y. M.; Li, S. J.; Bao, Q. L.; Zhang, H.; Zhang, Y. G. Field-induced n-doping of black phosphorus for CMOS compatible 2D logic electronics with high electron mobility. *Adv. Funct. Mater.* **2017**, *27*, 1702211.

[123] Wang, Y. Z.; Zhang, F.; Tang, X.; Chen, X.; Chen, Y. X.; Huang, W. C.; Liang, Z. M.; Wu, L. M.; Ge, Y. Q.; Song, Y. F. et al. All-optical phosphorene phase modulator with enhanced stability under ambient conditions. *Laser Photonics Rev.* **2018**, *12*, 1800016.

[124] Liu, S. X.; Li, Z. J.; Ge, Y. Q.; Wang, H. D.; Yue, R.; Jiang, X. T.; Li, J. Q.; Wen, Q.; Zhang, H. Graphene/phosphorene nano-heterojunction: Facile synthesis, nonlinear optics, and ultrafast photonics applications with enhanced performance. *Photonics Res.* **2017**, *5*, 662–668.

[125] Liu, J. M.; Chen, Y.; Li, Y.; Zhang, H.; Zheng, S. Q.; Xu, S. X. Switchable dual-wavelength Q-switched fiber laser using multilayer black phosphorus as a saturable absorber. *Photonics Res.* **2018**, *6*, 198–203.

[126] Zhou, J.; Li, Z. J.; Ying, M.; Liu, M. X.; Wang, X. M.; Wang, X. Y.; Cao, L. W.; Zhang, H.; Xu, G. X. Black phosphorus nanosheets for rapid microRNA detection. *Nanoscale* **2018**, *10*, 5060–5064.

[127] Jiang, X. F.; Zeng, Z. K.; Li, S.; Guo, Z. N.; Zhang, H.; Huang, F.; Xu, Q. H. Tunable broadband nonlinear optical properties of black phosphorus quantum dots for femtosecond laser pulses. *Materials* **2017**, *10*, 210.

[128] Luo, M. M.; Fan, T. J.; Zhou, Y.; Zhang, H.; Mei, L. 2D black phosphorus-based biomedical applications. *Adv. Funct. Mater.* **2019**, *29*, 1808306.

[129] Zhang, M.; Wu, Q.; Zhang, F.; Chen, L. L.; Jin, X. X.; Hu, Y. W.; Zheng, Z.; Zhang, H. 2D black phosphorus saturable absorbers for ultrafast photonics. *Adv. Opt. Mater.* **2019**, *7*, 1800224.

[130] Liang, X.; Ye, X. Y.; Wang, C.; Xing, C. Y.; Miao, Q. W.; Xie, Z. J.; Chen, X. L.; Zhang, X. D.; Zhang, H.; Mei, L. Photothermal cancer immunotherapy by erythrocyte membrane-coated black phosphorus formulation. *J. Control. Release* **2019**, *296*, 150–161.

[131] Fan, T. J.; Zhou, Y. S.; Qiu, M.; Zhang, H. Black phosphorus: A novel nanoplatform with potential in the field of bio-photonic nanomedicine. *J. Innov. Opt. Health Sci.* **2018**, *11*, 1830003.

[132] Zhang, J. N.; Chen, S.; Ma, Y.; Wang, D. Y.; Zhang, J.; Wang, Y. D.; Li, W. J.; Yu, Z. Q.; Zhang, H.; Yin, F. et al. Organosilicon modification to enhance the stability of black phosphorus nanosheets under ambient conditions. *J. Mater. Chem. B* **2018**, *6*, 4065–4070.

[133] Tang, S. N.; He, Z. L.; Liang, G. W.; Chen, S.; Ge, Y. Q.; Sang, D. K.; Lu, J. X.; Lu, S. B.; Wen, Q.; Zhang, H. Pulse duration dependent nonlinear optical response in black phosphorus dispersions. *Opt. Commun.* **2018**, *406*, 244–248.

[134] Huang, H.; Xiao, Q. L.; Wang, J. H.; Yu, X. F.; Wang, H. Y.; Zhang, H.; Chu, P. K. Black phosphorus: A two-dimensional reductant for *in situ* nanofabrication. *NPJ 2D Mater. Appl.* **2017**, *1*, 20.

[135] Qiu, M.; Singh, A.; Wang, D.; Qu, J. L.; Swihart, M.; Zhang, H.; Prasad, P. N. Biocompatible and biodegradable inorganic nano-structures for nanomedicine: Silicon and black phosphorus. *NanoToday* **2019**, *25*, 135–155.

[136] Li, C.; Liu, J.; Guo, Z. N.; Zhang, H.; Ma, W. W.; Wang, J. Y.; Xu, X. D.; Su, L. B. Black phosphorus saturable absorber for a diode-pumped passively Q-switched Er: CaF_2 mid-infrared laser. *Opt. Commun.* **2018**, *406*, 158–162.

[137] Sharma, A.; Wen, B.; Liu, B. Q.; Myint, Y. W.; Zhang, H.; Lu, Y. R. Defect engineering in few-layer phosphorene. *Small* **2018**, *14*, 1704556.

[138] Li, Z. J.; Xu, H.; Shao, J. D.; Jiang, C.; Zhang, F.; Lin, J.; Zhang, H.; Li, J. Q.; Huang, P. Polydopamine-functionalized black phosphorus quantum dots for cancer theranostics. *Appl. Mater. Today* **2019**, *15*, 297–304.

[139] Tang, X.; Chen, H.; Ponraj, J. S.; Dhanabalan, S. C.; Xiao, Q. L.; Fan, D. Y.; Zhang, H. Fluorination-enhanced ambient stability and electronic tolerance of black phosphorus quantum dots. *Adv. Sci.* **2018**, *5*, 1800420.

[140] Sang,D. K.; Wang, H. D.; Guo, Z. N.; Xie, N.; Zhang, H. Recent developments in stability and passivation techniques of phosphorene toward next-generation device applications. *Adv. Funct. Mater.* **2019**, *29*, 1903419.

[141] Wang, Y. Y.; Huang, P.; Ye, M.; Quhe, R. G.; Pan, Y. Y.; Zhang, H.; Zhong, H. X.; Shi, J. J.; Lu, J. Many-body effect, carrier mobility, and device performance of hexagonal arsenene and antimonene. *Chem. Mater.* **2017**, *29*, 2191–2201.

[142] Wang, Y. Y.; Ye, M.; Weng, M. Y.; Li, J. Z.; Zhang, X. Y.; Zhang, H.; Guo, Y.; Pan, Y. Y.; Xiao, L.; Liu, J. K. et al. Electrical contacts in monolayer arsenene devices. *ACS Appl. Mater. Interfaces* **2017**, *9*, 29273–29284.

[143] Tao, W.; Ji, X. Y.; Xu, X. D.; Islam, M. A.; Li, Z. J.; Chen, S.; Saw, P. E.; Zhang, H.; Bharwani, Z.; Guo, Z. L. et al. Antimonene quantum dots: Synthesis and application as near-infrared photothermal agents for effective cancer therapy. *Angew. Chem., Int. Ed.* **2017**, *56*, 11896–11900.

[144] Lu, L.; Tang, X.; Cao, R.; Wu, L. M.; Li, Z. J.; Jing, G. H.; Dong, B. Q.; Lu, S. B.; Li, Y.; Xiang, Y. J. et al. Broadband nonlinear optical response in few-layer antimonene and antimonene quantum dots: A promising optical Kerr media with enhanced stability. *Adv. Opt. Mater.* **2017**, *5*,1700301.

[145] Song, Y. F.; Liang, Z. M.; Jiang, X. T.; Chen, Y. X.; Li, Z. J.; Lu, L.; Ge, Y. Q.; Wang, K.; Zheng, J. L.; Lu, S. B. et al. Few-layer antimonene decorated microfiber: Ultra-short pulse generation and all-optical thresholding with enhanced long term stability. *2D Mater.* **2017**, *4*, 045010.

[146] Tao, W.; Ji, X. Y.; Zhu, X. B.; Li, L.; Wang, J. Q.; Zhang, Y.; Saw, P. E.; Li, W. L.; Kong, N.; Islam, M. A. et al. Two-dimensional antimonene-based photonic nanomedicine for cancer theranostics. *Adv. Mater.* **2018**, *30*, 1802061.

[147] Xue, T. Y.; Liang, W. Y.; Li, Y. W.; Sun, Y. H.; Xiang, Y. J.; Zhang, Y. P.; Dai, Z. G.; Duo, Y. H.; Wu, L. M.; Qi, K. et al. Ultrasensitive detection of miRNA with an antimonene-based surface plasmon resonance sensor. *Nat. Commun.* **2019**, *10*, 28.

[148] Song, Y. F.; Chen, Y. X.; Jiang, X. T.; Liang, W. Y.; Wang, K.; Liang, Z. M.; Ge, Y. Q.; Zhang, F.; Wu, L. M.; Zheng, J. L. et al. Nonlinear few-layer antimonene-based all-optical signal processing: Ultrafast optical switching and high-speed wavelength conversion. *Adv. Opt. Mater.* **2018**, *6*, 1701287.

[149] Wang, Y. Z.; Huang, W. C.; Wang, C.; Guo, J.; Zhang, F.; Song, Y. F.; Ge, Y. Q.; Wu, L. M.; Liu, J.; Li, J. Q. et al. An all-optical, actively Q-switched fiber laser by an antimonene-based optical modulator. *Laser Photonics Rev.* **2019**, *13*, 1800313.

[150] Zhang, G. J.; Tang, X.; Fu, X.; Chen, W. C.; Shabbir, B.; Zhang, H.; Liu, Q.; Gong, M. L. 2D group-VA fluorinated antimonene: Synthesis and saturable absorption. *Nanoscale* **2019**, *11*, 1762–1769.

[151] Tang, X.; Hu, L.; Fan, T. W.; Zhang, L.; Zhu, L. P.; Li, H.; Liu, H. L.; Liang, J. Y.; Wang, K. D.; Li, Z. J. et al. Robust above-room-temperature ferromagnetism in few-layer antimonene triggered by nonmagnetic adatoms. *Adv. Funct. Mater.* **2019**, *29*, 1808746.

[152] Song, Y. F.; Chen, Y. X.; Jiang, X. T.; Liang, Z. M.; Liang, W. Y.; Ge, Y. Q.; Zhang, H. Few-layer antimonene decorated microfiber as an all optical thresholder and wavelength converter for optical signal processing. In *Proceedings of Asia Communications and Photonics Conference 2017*. Guangzhou, China, 2017.

[153] Zhang, F.; Jiang, X. T.; He, Z. L.; Liang, W. Y.; Xu, S. X.; Zhang, H. Third-order nonlinear optical responses and carrier dynamics in antimonene. *Opt. Mater.* **2019**, *95*, 109209.

[154] Lu, L.; Wang, W. H.; Wu, L. M.; Jiang, X. T.; Xiang, Y. J.; Li, J. Q.; Fan, D. Y.; Zhang, H. All-optical switching of two continuous waves in few layer bismuthene based on spatial cross-phase modulation. *ACS Photonics* **2017**, *4*, 2852–2861.

[155] Guo, B.; Wang, S. H.; Wu, Z. X.; Wang, Z. X.; Wang, D. H.; Huang, H.; Zhang, F.; Ge, Y. Q.; Zhang, H. Sub-200 fs soliton mode-locked fiber laser based on bismuthene saturable absorber. *Opt. Express* **2018**, *26*, 22750–22760.

[156] Chai, T.; Li, X. H.; Feng, T. C.; Guo, P. L.; Song, Y. F.; Chen, Y. X.; Zhang, H. Few-layer bismuthene for ultrashort pulse generation in a dissipative system based on an evanescent field. *Nanoscale* **2018**, *10*, 17617–17622.

[157] Huang, H.; Ren, X. H.; Li, Z. J.; Wang, H. D.; Huang, Z. Y.; Qiao, H.; Tang, P. H.; Zhao, J. L.; Liang, W. Y.; Ge, Y. Q. et al. Two-dimensional bismuth nanosheets as prospective photo-detector with tunable optoelectronic performance. *Nanotechnology* **2018**, *29*, 235201.

[158] Su, X. C.; Wang, Y. R.; Zhang, B. T.; Zhang, H.; Yang, K. J.; Wang, R. H.; He, J. L. Bismuth quantum dots as an optical saturable absorber for a 1.3 μm Q-switched solid-state laser. *Appl. Opt.* **2019**, *58*, 1621–1625.

[159] Xing, C. Y.; Huang, W. C.; Xie, Z. J.; Zhao, J. L.; Ma, D. T.; Fan, T. J.; Liang, W. Y.; Ge, Y. Q.; Dong, B. Q.; Li, J. Q. et al. Ultrasmall bismuth quantum dots: Facile liquid-phase exfoliation, characterization, and application in high-performance UV−Vis photodetector. *ACS Photonics* **2018**, *5*, 621–629.

[160] Lu, L.; Liang, Z. M.; Wu, L. M.; Chen, Y. X.; Song, Y. F.; Dhanabalan, S. C.; Ponraj, J. S.; Dong, B. Q.; Xiang, Y. J.; Xing, F. et al. Few-layer bismuthene: Sonochemical exfoliation, nonlinear optics and applications for ultrafast photonics with enhanced stability. *Laser Photonics Rev.* **2018**, *12*, 1870012.

[161] Wang, Y. Z.; Huang, W. C.; Zhao, J. L.; Huang, H.; Wang, C.; Zhang, F.; Liu, J.; Li, J. Q.; Zhang, M.; Zhang, H. A bismuthene-based multifunctional all-optical phase and intensity modulator enabled by photothermal effect. *J. Mater. Chem. C* **2019**, *7*, 871–878.

[162] Xing, C. Y.; Xie, Z. J.; Liang, Z. M.; Liang, W. Y.; Fan, T. J.; Ponraj, J. S.; Dhanabalan, S. C.; Fan, D. Y.; Zhang, H. 2D nonlayered selenium nanosheets: Facile synthesis, photoluminescence, and ultrafast photonics. *Adv. Opt. Mater.* **2017**, *5*, 1700884.

[163] Fan, T. J.; Xie, Z. J.; Huang, W. C.; Li, Z. J.; Zhang, H. Two-dimensional non-layered selenium nanoflakes: Facile fabrications and applications for self-powered photo-detector. *Nanotechnology* **2019**, *30*, 114002.

[164] Wu, L. M.; Huang, W. C.; Wang, Y. Z.; Zhao, J. L.; Ma, D. T.; Xiang, Y. J.; Li, J. Q.; Ponraj, J. S.; Dhanabalan, S. C.; Zhang, H. 2D tellurium based high-performance all-optical nonlinear photonic devices. *Adv. Funct. Mater.* **2019**, *29*, 1806346.

[165] Xie, Z. J.; Xing, C. Y.; Huang, W. C.; Fan, T. J.; Li, Z. J.; Zhao, J. L.; Xiang, Y. J.; Guo, Z. N.; Li, J. Q.; Yang, Z. G. et al. Ultrathin 2D nonlayered tellurium nanosheets: Facile liquid-phase exfoliation, characterization, and photoresponse with high performance and enhanced stability. *Adv. Funct. Mater.* **2018**, *28*, 1705833.

[166] Huang, W. C.; Zhang, Y.; You, Q.; Huang, P.; Wang, Y. Z.; Huang, Z. N.; Ge, Y. Q.; Wu, L. M.; Dong, Z. J.; Dai, X. Y. et al. Enhanced photodetection properties of tellurium@selenium roll-to-roll nanotube heterojunctions. *Small* **2019**, *15*, 1900902.

[167] Xing, C. Y.; Huang, D. Z.; Chen, S. Y.; Huang, Q. C.; Zhou, C. H.; Peng, Z. C.; Li, J. G.; Zhu, X.; Liu, Y. Z.; Liu, Z. P. et al. Engineering lateral heterojunction of selenium-coated tellurium nanomaterials toward highly efficient solar desalination. *Adv. Sci.* **2019**, *6*, 1900531.

[168] Guo, J.; Zhao, J. L.; Huang, D. Z.; Wang, Y. Z.; Zhang, F.; Ge, Y. Q.; Song, Y. F.; Xing, C. Y.; Fan, D. Y.; Zhang, H. Two-dimensional tellurium-polymer membrane for ultrafast photonics. *Nanoscale* **2019**, *11*, 6235–6242.

[169] Yan, J. H.; Zhang, X. Y.; Pan, Y. Y.; Li, J. Z.; Shi, B. W.; Liu, S. Q.; Yang, J.; Song, Z. G.; Zhang, H.; Ye, M. et al. Monolayer tellurene-metal contacts. *J. Mater. Chem. C* **2018**, *6*, 6153–6163.

[170] Molle, A. Xenes: A new emerging two-dimensional materials platform for nanoelectronics. *ECS Trans.* **2016**, *75*, 163–173.

[171] Molle, A.; Goldberger, J.; Houssa, M.; Xu, Y.; Zhang, S. C.; Akinwande, D. Buckled two-dimensional Xene sheets. *Nat. Mater.* **2017**, *16*, 163–169.

[172] Zhang, Z. H.; Yang, Y.; Penev, E. S.; Yakobson, B. I. Elasticity, flexibility, and ideal strength of borophenes. *Adv. Funct. Mater.* **2017**, *27*, 1605059.

[173] Bernasconi, M.; Chiarotti, G. L.; Tosatti, E. *Ab initio* calculations of structural and electronicproperties of gallium solid-state phases. *Phys. Rev. B* **1995**, *52*, 9988–9998.

[174] Shao, Z. G.; Ye, X. S.; Yang, L.; Wang, C. L. First-principles calculation of intrinsic carrier mobility of silicene. *J. Appl. Phys.* **2013**, *114*, 093712.
[175] Liu, N. N.; Bo, G. Y.; Liu, Y. N.; Xu, X.; Du, Y.; Dou, S. X. Recent progress on germanene and functionalized germanene: Preparation, characterizations, applications, and challenges. *Small* **2019**, *15*, 1805147.
[176] Huang, S. X.; Ling, X. Black phosphorus: Optical characterization, properties and applications. *Small* **2017**, *13*, 1700823.
[177] Pauling, L.; Simonetta, M. Bond orbitals and bond energy in elementary phosphorus. *J. Chem. Phys.* **1952**, *20*, 29–34.
[178] Hart, R. R.; Robin, M. B.; Kuebler, N. A. 3p orbitals, bent bonds, and the electronic spectrum of the P_4 molecule. *J. Chem. Phys.* **1965**, *42*, 3631–3638.
[179] Pumera, M.; Sofer, Z. 2D monoelemental arsenene, antimonene, and bismuthene: Beyond black phosphorus. *Adv. Mater.* **2017**, *29*, 1605299.
[180] Zhang, S. L.; Yan, Z.; Li, Y. F.; Chen, Z. F.; Zeng, H. B. Atomically thin arsenene and antimonene: Semimetal-semiconductor and indirect-direct band-gap transitions. *Angew. Chem., Int. Ed.* **2015**, *54*, 3112–3115.
[181] Zhang, S. L.; Guo, S. Y.; Chen, Z. F.; Wang, Y. L.; Gao, H. J.; Gómez-Herrero, J.; Ares, P.; Zamora, F.; Zhu, Z.; Zeng, H. B. Recent progress in 2D group-VA semiconductors: From theory to experiment. *Chem. Soc. Rev.* **2018**, *47*, 982–1021.
[182] Lee, J.; Tian, W. C.; Wang, W. L.; Yao, D. X. Two-dimensional pnictogen honeycomb lattice: Structure, on-site spin-orbit coupling and spin polarization. *Sci. Rep.* **2015**, *5*, 11512.
[183] Kadioglu, Y.; Kilic, S. B.; Demirci, S.; Akturk, O. Ü.; Aktürk, E.; Ciraci, S. Modification of electronic structure, magnetic structure, and topological phase of bismuthene by point defects. *Phys. Rev. B* **2017**, *96*, 245424.
[184] Wang, D.; Tang, L. M.; Jiang, X. X.; Tan, J. Y.; He, M. D.; Wang, X. J.; Chen, K. Q. High bipolar conductivity and robust in-plane spontaneous electric polarization in selenene. *Adv. Electron. Mater.* **2019**, *5*, 1800475.
[185] Xian, L. D.; Pérez Paz, A.; Bianco, E.; Ajayan, P. M.; Rubio, A. Square selenene and tellurene: Novel group VI elemental 2D materials with nontrivial topological properties. *2D Mater.* **2017**, *4*, 041003.
[186] Xiang, Y.; Gao, S. J.; Xu, R. G.; Wu, W. Z.; Leng, Y. S. Phase transition in two-dimensional tellurene under mechanical strain modulation. *Nano Energy* **2019**, *58*, 202–210.
[187] Sharma, S.; Singh, N.; Schwingenschlogl, U. Two-dimensional tellurene as excellent thermoelectric material.*ACS Appl. Energy Mater.* **2018**, *1*, 1950–1954.
[188] Wu, W. Z.; Qiu, G.; Wang, Y. X.; Wang, R. X.; Ye, P. D. Tellurene: Its physical properties, scalable nanomanufacturing, and device applications. *Chem. Soc. Rev.* **2018**, *47*, 7203–7212.
[189] Cao, R.; Wang, H. D.; Guo, Z. N.; Sang, D. K.; Zhang, L. Y.; Xiao, Q. L.; Zhang, Y. P.; Fan, D. Y.; Li, J. Q.; Zhang, H. Black phosphorous/indium selenide photoconductive detector for visible and near-infrared light with high sensitivity. *Adv. Opt. Mater.* **2019**, *7*, 1900020.
[190] Yin, Y. L.; Cao, R.; Guo, J. S.; Liu, C. Y.; Li, J.; Feng, X. L.; Wang, H. D.; Du, W.; Qadir, A.; Zhang, H. et al. High-speed and high-responsivity hybrid silicon/black-phosphorus waveguide photodetectors at 2 μm. *Laser Photonics Rev.* **2019**, *13*, 1900032.
[191] Guo, Z. N.; Zhang, H.; Lu, S. B.; Wang, Z. T.; Tang, S. Y.; Shao, J. D.; Sun, Z. B.; Xie, H. H.; Wang, H. Y.; Yu, X. F. et al. From black phosphorus to phosphorene: Basic solvent exfoliation, evolution of Raman scattering, and applications to ultrafast photonics. *Adv. Funct. Mater.* **2015**, *25*, 6996–7002.
[192] Li, J. F.; Luo, H. Y.; Zhai, B.; Lu, R. G.; Guo, Z. N.; Zhang, H.; Liu, Y. Black phosphorus: A two-dimension saturable absorption material for mid-infrared Q-switched and mode-locked fiber lasers. *Sci. Rep.* **2016**, *6*, 30361.
[193] Kong, L. C.; Qin, Z. P.; Xie, G. Q.; Guo, Z. N.; Zhang, H.; Yuan, P.; Qian, L. J. Black phosphorus as broadband saturable absorber for pulsed lasers from 1 to 2.7 μm wavelength. *Laser Phys. Lett.* **2016**, *13*, 045801.
[194] Ren, X. H.; Li, Z. J.; Huang, Z. Y.; Sang, D.; Qiao, H.; Qi, X.; Li, J. Q.; Zhong, J. X.; Zhang, H. Environmentally robust black phosphorus nanosheets in solution: Application for self-powered photodetector. *Adv. Funct. Mater.* **2017**, *27*, 1606834.
[195] Chu, Z. Z.; Liu, J.; Guo, Z. N.; Zhang, H. 2 μm passively Q-switched laser based on black phosphorus. *Opt. Mater. Express* **2016**, *6*, 2374–2379.
[196] Wang, H. D.; Sang, D. K.; Guo, Z. N.; Cao, R.; Zhao, J. L.; Shah, M. N. U.; Fan, T. J.; Fan, D. Y.; Zhang, H. Black phosphorus-based field effect transistor devices for Ag ions detection. *Chin. Phys. B* **2018**, *27*, 087308.
[197] Guo, Z. N.; Chen, S.; Wang, Z. Z.; Yang, Z. Y.; Liu, F.; Xu, Y. H.; Wang, J. H.; Yi, Y.; Zhang, H.; Liao, L. et al. Metal-ion-modified black phosphorus with enhanced stability and transistor performance. *Adv. Mater.* **2017**, *29*, 1703811.
[198] Rahman, M. Z.; Kwong, C. W.; Davey, K.; Qiao, S. Z. 2D phosphorene as a water splitting photocatalyst: Fundamentals to applications. *Energy Environ. Sci.* **2016**, *9*, 709–728.
[199] Sun, Z. B.; Zhao, Y. T.; Li, Z. B.; Cui, H. D.; Zhou, Y. Y.; Li, W. H.; Tao, W.; Zhang, H.; Wang, H. Y.; Chu, P. K. et al. TiL_4-coordinated black phosphorus quantum dots as an efficient contrast agent for *in vivo* photoacoustic imaging of cancer. *Small* **2017**, *13*, 1602896.
[200] Tao, W.; Kong, N.; Ji, X. Y.; Zhang, Y. P.; Sharma, A.; Ouyang, J.; Qi, B. W.; Wang, J. Q.; Xie, N.; Kang, C. et al. Emerging two-dimensional monoelemental materials (Xenes) for biomedical applications. *Chem. Soc. Rev.* **2019**, *48*, 2891–2912.
[201] Sergeeva, A. P.; Popov, I. A.; Piazza, Z. A.; Li, W. L.; Romanescu, C.; Wang, L. S.; Boldyrev, A. I. Understanding boron through size-selected clusters: Structure, chemical bonding, and fluxionality. *Acc. Chem. Res.* **2014**, *47*, 1349–1358.
[202] Zhai, H. J.; Kiran, B.; Li, J.; Wang, L. S. Hydrocarbon analogues of boron clusters – planarity, aromaticity and antiaromaticity. *Nat. Mater.* **2003**, *2*, 827–833.
[203] Zhai, H. J.; Zhao, Y. F.; Li, W. L.; Chen, Q.; Bai, H.; Hu, H. S.; Piazza, Z. A.; Tian, W. J.; Lu, H. G.; Wu, Y. B. et al. Observation of an all-boron fullerene. *Nat. Chem.* **2014**, *6*, 727–731.
[204] Liu, H. S.; Gao, J. F.; Zhao, J. J. From boron cluster to two-dimensional boron sheet on Cu(111) surface: Growth mechanism and hole formation. *Sci. Rep.* **2013**, *3*, 3238.
[205] Mannix, A. J.; Zhou, X. F.; Kiraly, B.; Wood, J. D.; Alducin, D.; Myers, B. D.; Liu, X. L.; Fisher, B. L.; Santiago, U.; Guest, J. R. et al. Synthesis of borophenes: Anisotropic, two-dimensional boron polymorphs. *Science* **2015**, *350*, 1513–1516.
[206] Feng, B. J.; Zhang, J.; Zhong, Q.; Li, W. B.; Li, S.; Li, H.; Cheng, P.; Meng, S.; Chen, L.; Wu, K. H. Experimental realization of two-dimensional boron sheets. *Nat. Chem.* **2016**, *8*, 563–568.
[207] Oganov, A. R.; Chen, J. H.; Gatti, C.; Ma, Y. Z.; Ma, Y. M.; Glass, C. W.; Liu, Z. X.; Yu, T.; Kurakevych, O. O.; Solozhenko, V. L. Ionic high-pressure form of elemental boron. *Nature* **2009**, *457*, 863–867.
[208] Ogitsu, T.; Schwegler, E.; Galli, G. β-Rhombohedral boron: At the crossroads of the chemistry of boron and the physics of frustration. *Chem. Rev.* **2013**, *113*, 3425–3449.
[209] Peng, B.; Zhang, H.; Shao, H. Z.; Xu, Y. F.; Zhang, R. J.; Zhua, H. Y. The electronic, optical, and thermodynamic properties of borophene from first-principles calculations. *J. Mater. Chem. C* **2016**, *4*, 3592–3598.
[210] Xu, J. Q.; Chang, Y. Y.; Gan, L.; Ma, Y.; Zhai, T. Y. Ultrathin single-crystalline boron nanosheets for enhanced electro-optical performances. *Adv. Sci.* **2015**, *2*, 1500023.
[211] Bosio, L. Crystalstructures of Ga(II) and Ga(III). *J. Chem. Phys.* **1978**, *68*, 1221–1223.
[212] Kenichi, T.; Kazuaki, K.; Masao, A. High-pressure bct-fcc phase transition in Ga. *Phys. Rev. B* **1998**, *58*, 2482–2486.
[213] Schulte, O.; Holzapfel, W. B. Effect of pressure on the atomic volume of Ga and Tl up to 68 GPa. *Phys. Rev. B* **1997**, *55*, 8122–8128.
[214] Steenbergen, K. G.; Gaston, N. First-principles melting of gallium clusters down to nine atoms: Structural and electronic contributions to melting. *Phys. Chem. Chem. Phys.* **2013**, *15*, 15325–15332.
[215] Kochat, V.; Samanta, A.; Zhang, Y.; Bhowmick, S.; Manimunda, P.; Asif, S. A. S.; Stender, A. S.; Vajtai, R.; Singh, A. K.; Tiwary, C. S. et al. Atomically thin gallium layers from solid-melt exfoliation.

Sci. Adv. **2018**, *4*, e1701373.
[216] Krawiec, M. Functionalization of group-14 two-dimensional materials. *J. Phys. Condens. Matter* **2018**, *30*, 233003.
[217] Pulci, O.; Gori, P.; Marsili, M.; Garbuio, V.; Del Sole, R.; Bechstedt, F. Strong excitons in novel two-dimensional crystals: Silicane and germanane. *EPL* **2012**, *98*, 37004.
[218] Voon, L. C. L. Y.; Zhu, J. J.; Schwingenschlogl, U. Silicene: Recent theoretical advances. *Appl. Phys. Rev.* **2016**, *3*, 040802.
[219] Cahangirov, S.; Topsakal, M.; Aktürk, E.; Şahin, H.; Ciraci, S. Two- and one-dimensional honeycomb structures of silicon and germanium. *Phys. Rev. Lett.* **2009**, *102*, 236804.
[220] Houssa, M.; Pourtois, G.; Afanas'ev, V. V.; Stesmans, A. Can silicon behave like graphene? A first-principles study. *Appl. Phys. Lett.* **2010**, *97*, 112106.
[221] Zhao, J. J.; Liu, H. S.; Yu, Z. M.; Quhe, R. G.; Zhou, S.; Wang, Y. Y.; Liu, C. C.; Zhong, H. X.; Han, N. N.; Lu, J. et al. Rise of silicene: A competitive 2D material. *Prog. Mater. Sci.* **2016**, *83*, 24–151.
[222] Drummond, N. D.; Zólyomi, V.; Fal'ko, V. I. Electrically tunable band gap in silicene. *Phys. Rev. B* **2012**, *85*, 075423.
[223] Cai, Y. M.; Chuu, C. P.; Wei, C. M.; Chou, M. Y. Stability and electronic properties of two-dimensional silicene and germanene on graphene. *Phys. Rev. B* **2013**, *88*, 245408.
[224] Kaloni, T. P.; Schwingenschlögl, U. Stability of germanene under tensile strain. *Chem. Phys. Lett.* **2013**, *583*, 137–140.
[225] Xu, Y.; Tang, P. Z.; Zhang, S. C. Large-gap quantum spin Hall states in decorated stanene grown on a substrate. *Phys. Rev. B* **2015**, *92*, 081112.
[226] Vogg, G.; Brandt, M. S.; Stutzmann, M. Polygermyne—A prototype system for layered germanium polymers. *Adv. Mater.* **2000**, *12*, 1278–1281.
[227] Ma, Y. D.; Dai, Y.; Niu, C. W.; Huang, B. B. Halogenated two-dimensional germanium: Candidate materials for being of Quantum Spin Hall state. *J. Mater. Chem.* **2012**, *22*, 12587–12591.
[228] Li, Y. F.; Chen, Z. F. Tuning electronic properties of germanane layers by external electric field and biaxial tensile strain: A computational study. *J. Phys. Chem. C* **2014**, *118*, 1148–1154.
[229] Si, C.; Liu, J. W.; Xu, Y.; Wu, J.; Gu, B. L.; Duan, W. H. Functionalized germanene as a prototype of large-gap two-dimensional topological insulators. *Phys. Rev. B* **2014**, *89*, 115429.
[230] Sahoo, S. K.; Wei, K. H. A perspective on recent advances in 2D stanene nanosheets. *Adv. Mater. Interfaces* **2019**, *6*, 1900752.
[231] Liu, X. H.; Wang, Y.; Li, F.; Li, Y. F. Two-dimensional stanane: Strain-tunable electronic structure, high carrier mobility, and pronounced light absorption. *Phys. Chem. Chem. Phys.* **2016**, *18*, 14638–14643.
[232] Lu, P. F.; Wu, L. Y.; Yang, C. G.; Liang, D.; Quhe, R. G.; Guan, P. F.; Wang, S. M. Quasiparticle and optical properties of strained stanene and stanane. *Sci. Rep.* **2017**, *7*, 3912.
[233] Yu, X. L.; Huang, L.; Wu, J. S.From a normal insulator to a topological insulator in plumbene. *Phys. Rev. B* **2017**, *95*, 125113.
[234] Zhao, H.; Zhang, C. W.; Ji, W. X.; Zhang, R. W.; Li, S. S.; Yan, S. S.; Zhang, B. M.; Li, P.; Wang, P. J. Unexpected giant-gap quantum spin hall insulator in chemically decorated plumbene monolayer. *Sci. Rep.* **2016**, *6*, 20152.
[235] Zhao, H.; Ji, W. X.; Zhang, C. W.; Li, P.; Li, F.; Wang, P. J.; Zhang, R. W. First-principles prediction of a giant-gap quantum spin Hall insulator in Pb thin film. *Phys. Chem. Chem. Phys.* **2016**, *18*, 31862–31868.
[236] Hultgren, R.; Gingrich, N. S.; Warren, B. E.The atomic distribution in red and black phosphorus and the crystal structure of black phosphorus. *J. Chem. Phys.* **1935**, *3*, 351–355.
[237] Brown, A.; Rundqvist, S. Refinement of the crystal structure of black phosphorus. *Acta Crystallogr.* **1965**, *19*, 684–685.
[238] Thurn, H.; Kerbs, H. Crystal structure of violet phosphorus. *Angew. Chem., Int. Ed.* **1966**, *5*, 1047–1048.
[239] Xia, F. N.; Wang, H.; Jia, Y. C. Rediscovering black phosphorus as an anisotropic layered material for optoelectronics and electronics. *Nat. Commun.* **2014**, *5*, 4458.
[240] Li, L. K.; Yu, Y. J.; Ye, G. J.; Ge, Q. Q.; Ou, X. D.; Wu, H.; Feng, D. L.; Chen, X. H.; Zhang, Y. B. Black phosphorus field-effect transistors. *Nat. Nanotechnol.* **2014**, *9*, 372–377.
[241] Lu, J. P.; Carvalho, A.; Wu, J.; Liu, H. W.; Tok, E. S.; Neto, A. H. C.; Özyilmaz, B.; Sow, C. H. Enhanced photoresponse from phosphorene-phosphorene-suboxide junction fashioned by focused laser micromachining. *Adv. Mater.* **2016**, *28*, 4090–4096.
[242] Zhang, C. D.; Lian, J. C.; Yi, W.; Jiang, Y. H.; Liu, L. W.; Hu, H.; Xiao, W. D.; Du, S. X.; Sun, L. L.; Gao, H. J. Surface structures of black phosphorus investigated with scanning tunneling microscopy. *J. Phys. Chem. C* **2009**, *113*, 18823–18826.
[243] Takao, Y.; Asahina, H.; Morita, A. Electronicstructure of black phosphorus in tightbinding approach. *J. Phys. Soc. Jpn.* **1981**, *50*, 3362–3369.
[244] Liu, H.; Neal, A. T.; Zhu, Z.; Luo, Z.; Xu, X. F.; Tománek, D.; Ye, P. D. Phosphorene: An unexplored 2D semiconductor with a high hole mobility. *ACS Nano* **2014**, *8*, 4033–4041.
[245] Tran, V.; Soklaski, R.; Liang, Y. F.; Yang, L. Layer-controlled band gap and anisotropic excitons in few-layer black phosphorus. *Phys. Rev. B* **2014**, *89*, 235319.
[246] Qiao, J. S.; Kong, X. H.; Hu, Z. X.; Yang, F.; Ji, W. High-mobility transport anisotropy and linear dichroism in few-layer black phosphorus. *Nat. Commun.* **2014**, *5*, 4475.
[247] Ji, J. P.; Song, X. F.; Liu, J. Z.; Yan, Z.; Huo, C. X.; Zhang, S. L.; Su, M.; Liao, L.; Wang, W. H.; Ni, Z. H. et al. Two-dimensional antimonene single crystals grown by van der Waals epitaxy. *Nat. Commun.* **2016**, *7*, 13352.
[248] Akturk, O. Ü.; Özçelik, V. O.; Ciraci, S. Single-layer crystalline phases of antimony: Antimonenes. *Phys. Rev. B* **2015**, *91*, 235446.
[249] Wang, G. X.; Pandey, R.; Karna, S. P. Atomically thin group V elemental films: Theoretical investigations of antimonene allotropes. *ACS Appl. Mater. Interfaces* **2015**, *7*, 11490–11496.
[250] Singh, D.; Gupta, S. K.; Sonvane, Y.; Lukačević, I. Antimonene: A monolayer material for ultraviolet optical nanodevices. *J. Mater. Chem. C* **2016**, *4*, 6386–6390.
[251] Cheng, L.; Liu, H. J.; Tan, X. J.; Zhang, J.; Wei, J.; Lv, H. Y.; Shi, J.; Tang, X. F. Thermoelectric properties of a monolayer bismuth. *J. Phys. Chem. C* **2014**, *118*, 904–910.
[252] Freitas, R. R. Q.; Rivelino, R.; de Brito Mota, F.; de Castilho, C. M. C.; Kakanakova-Georgieva, A.; Gueorguiev, G. K. Topological insulating phases in two-dimensional bismuth-containing single layers preserved by hydrogenation. *J. Phys. Chem. C* **2015**, *119*, 23599–23606.
[253] Xiao, S. H.; Wei, D. H.; Jin, X. F. Bi(111) thin film with insulating interior but metallic surfaces. *Phys. Rev. Lett.* **2012**, *109*, 166805.
[254] Glass, S.; Reis, F.; Bauernfeind, M.; Aulbach, J.; Scholz, M. R.; Adler, F.; Dudy, L.; Li, G.; Claessen, R.; Schäfer, J. Atomic-scale mapping of layer-by-layer hydrogen etching and passivation of SiC(0001) substrates. *J. Phys. Chem. C* **2016**, *120*, 10361–10367.
[255] Zhang, S. L.; Xie, M. Q.; Li, F. Y.; Yan, Z.; Li, Y. F.; Kan, E. J.; Liu, W.; Chen, Z. F.; Zeng, H. B. Semiconducting Group 15 monolayers: A broad range of band gaps and high carrier mobilities. *Angew. Chem., Int. Ed.* **2016**, *55*, 1666–1669.
[256] Hussain, N.; Liang, T. X.; Zhang, Q. Y.; Anwar, T.; Huang, Y.; Lang, J. L.; Huang, K.; Wu, H. Ultrathin Bi nanosheets with superior photoluminescence. *Small* **2017**, *13*, 1701349.
[257] Liu, Z.; Liu, C. X.; Wu, Y. S.; Duan, W. H.; Liu, F.; Wu, J. Stable nontrivial Z_2 topology in ultrathin Bi (111) films: A first-principles study. *Phys. Rev. Lett.* **2011**, *107*, 136805.
[258] Kasap, S.; Frey, J. B.; Belev, G.; Tousignant, O.; Mani, H.; Laperriere, L.; Reznik, A.; Rowlands, J. A. Amorphous selenium and its alloys from early xeroradiography to high resolution X-ray image detectors and ultrasensitive imaging tubes. *Phys. Status Solidi B* **2009**, *246*, 1794–1805.
[259] Lee, T. I.; Lee, S.; Lee, E.; Sohn, S.; Lee, Y.; Lee, S.; Moon, G.; Kim, D.; Kim, Y. S.; Myoung, J. M. et al. High-power density piezoelectric energy harvesting using radially strained ultrathin trigonal tellurium nanowire assembly. *Adv. Mater.* **2013**, *25*, 2920–2925.
[260] Abad, B.; Rull-Bravo, M.; Hodson, S. L.; Xu, X. F.; Martin-Gonzalez, M. Thermoelectric properties of electrodeposited tellurium films and the sodium lignosulfonate effect. *Electrochim. Acta* **2015**, *169*, 37–45.
[261] Sridharan, K.; Ollakkan, M. S.; Philip, R.; Park, T. J. Non-hydrothermal synthesis and optical limiting properties of one-dimensional Se/C, Te/C and Se-Te/C core-shell nanostructures.

Carbon **2013**, *63*, 263–273.
[262] Wang, R. P.; Su, X. Q.; Bulla, D.; Wang, T.; Gai, X.; Yang, Z. Y.; Madden, S.; Luther-Davies, B. Identifying the best chalcogenide glass compositions for the application in mid-infrared waveguides. In *Proceedings of SPIE9444*, *International Seminaron Photonics*, *Optics*, *and its Applications*, Bali, Indonesia, **2015**.
[263] Pradhan, A.; Roy, A.; Tripathi, S.; Som, A.; Sarkar, D.; Mishra, J. K.; Roy, K.; Pradeep, T.; Ravishankar, N.; Ghosh, A. Ultra-high sensitivity infra-red detection and temperature effects in a graphene-tellurium nanowire binary hybrid. *Nanoscale* **2017**, *9*, 9284–9290.
[264] Amani, M.; Tan, C. L.; Zhang, G.; Zhao, C. S.; Bullock, J.; Song, X. H.; Kim, H.; Shrestha, V. R.; Gao, Y.; Crozier, K. B. et al. Solution-synthesized high-mobility tellurium nanoflakes for short-wave infrared photodetectors. *ACS Nano* **2018**, *12*, 7253–7263.
[265] Zhang, Y.; Zhang, F.; Wu, L. M.; Zhang, Y. P.; Huang, W. C.; Tang, Y. F.; Hu, L. P.; Huang, P.; Zhang, X. W.; Zhang, H. Van der Waals integration of bismuth quantum dots-decorated tellurium nanotubes (Te@Bi) heterojunctions and plasma-enhanced optoelectronic applications. *Small* **2019**, *15*, 1903233.
[266] Wang, Y. X.; Qiu, G.; Wang, R. X.; Huang, S. Y.; Wang, Q. X.; Liu, Y. Y.; Du, Y. C.; Goddard III, W. A.; Kim, M. J.; Xu, X. F. et al. Field-effect transistors made from solution-grown two-dimensional tellurene. *Nat*. *Electron*. **2018**, *1*, 228–236.
[267] Zhu, Z. L.; Cai, X. L.; Yi, S.; Chen, J. L.; Dai, Y. W.; Niu, C. Y.; Guo, Z. X.; Xie, M. H.; Liu, F.; Cho, J. H.et al. Multivalency-driven formation of Te-based monolayer materials: A combined first-principles and experimental study. *Phys*. *Rev*. *Lett*. **2017**, *119*, 106101.
[268] Huang, X. C.; Guan, J. Q.; Lin, Z. J.; Liu, B.; Xing, S. Y.; Wang, W. H.; Guo, J. D. Epitaxial growth and band structure of Te film on graphene. *Nano Lett*. **2017**, *17*, 4619–4623.
[269] Du, Y. C.; Qiu, G.; Wang, Y. X.; Si, M. W.; Xu, X. F.; Wu, W. Z.; Ye, P. D. One-dimensional van der Waals material tellurium: Raman spectroscopy under strain and magneto-transport. *Nano Lett*. **2017**, *17*, 3965–3973.
[270] Jones, A. M.; Yu, H. Y.; Ghimire, N. J.; Wu, S. F.; Aivazian, G.; Ross, J. S.; Zhao, B.; Yan, J. Q.; Mandrus, D. G.; Xiao, D. et al. Optical generation of excitonic valley coherence in monolayer WSe_2. *Nat*. *Nanotechnol*. **2013**, *8*, 634–638.
[271] Georgiou, T.; Jalil, R.; Belle, B. D.; Britnell, L.; Gorbachev, R. V.; Morozov, S. V.; Kim, Y. J.; Gholinia, A.; Haigh, S. J.; Makarovsky, O. et al. Vertical field-effect transistor based on graphene-WS_2 heterostructures for flexible and transparent electronics. *Nat*. *Nanotechnol*. **2013**, *8*, 100–103.
[272] Li, Y. L.; Rao, Y.; Mak, K. F.; You, Y. M.; Wang, S. Y.; Dean, C. R.; Heinz, T. F. Probing symmetry properties of few-layer MoS_2 and h-BN by optical second-harmonic generation. *Nano Lett*. **2013**, *13*, 3329–3333.
[273] Buscema, M.; Groenendijk, D. J.; Blanter, S. I.; Steele, G. A.; van der Zant, H. S. J.; Castellanos-Gomez, A. Fast and broadband photoresponse of few-layer black phosphorus field-effect transistors. *Nano Lett*. **2014**, *14*, 3347–3352.
[274] Xu, Y. J.; Yuan, J.; Fei, L. F.; Wang, X. L.; Bao, Q. L.; Wang, Y.; Zhang, K.; Zhang, Y. G. Selenium-doped black phosphorus for high-responsivity 2D photodetectors. *Small* **2016**, *12*, 5000–5007.
[275] Liu, Y.; Sun, T.; Ma, W. L.; Yu, W. Z.; Nanjunda, S. B.; Li, S. J.; Bao, Q. L. Highly responsive broadband black phosphorus photodetectors. *Chin*. *Opt*. *Lett*. **2018**, *16*, 020002.
[276] Xiong, X.; Li, X. F.; Huang, M. Q.; Li, T. Y.; Gao, T. T.; Wu, Y. Q. High performance black phosphorus electronic and photonic devices with HfLaO dielectric. *IEEE Electr*. *Device Lett*. **2018**, *39*, 127–130.
[277] Yu, X. C.; Zhang, S. L.; Zeng, H. B.; Wang, Q. J. Lateral black phosphorene P-N junctions formed via chemical doping for high performance near-infrared photodetector. *Nano Energy* **2016**, *25*, 34–41.
[278] Chen, X. L.; Lu, X. B.; Deng, B. C.; Sinai, O.; Shao, Y. C.; Li, C.; Yuan, S. F.; Tran, V.; Watanabe, K.; Taniguchi, T. et al. Widely tunable black phosphorus mid-infrared photodetector. *Nat*. *Commun*. **2017**, *8*, 1672.
[279] Walmsley, T. S.; Chamlagain, B.; Rijal, U.; Wang, T. J.; Zhou, Z. X.; Xu, Y. Q. Gate-tunable photoresponse time in black phosphorus-MoS_2 heterojunctions. *Adv*. *Opt*. *Mater*. **2019**, *7*, 1800832.
[280] Deng, Y. X.; Luo, Z.; Conrad, N. J.; Liu, H.; Gong, Y. J.; Najmaei, S.; Ajayan, P. M.; Lou, J.; Xu, X. F.; Ye, P. D. Black phosphorus-monolayer MoS_2 van der Waals heterojunction p-n diode. *ACS Nano* **2014**, *8*, 8292–8299.
[281] Viti, L.; Hu, J.; Coquillat, D.; Knap, W.; Tredicucci, A.; Politano, A.; Vitiello, M. S. Black phosphorus terahertz photodetectors. *Adv*. *Mater*. **2015**, *27*, 5567–5572.
[282] Cao, S. W.; Xing, Y. H.; Han, J.; Luo, X.; Lv, W. X.; Lv, W. M.; Zhang, B. S.; Zeng, Z. M. Ultrahigh-photoresponsive UV photodetector based on a BP/ReS_2 heterostructure p-n diode. *Nanoscale* **2018**, *10*, 16805–16811.
[283] Ye, L.; Li, H.; Chen, Z. F.; Xu, J. B. Near-infrared photodetector based on MoS_2/black phosphorus heterojunction. *ACS Photonics* **2016**, *3*, 692–699.
[284] Ye, L.; Wang, P.; Luo, W. J.; Gong, F.; Liao, L.; Liu, T. D.; Tong, L.; Zang, J. F.; Xu, J. B.; Hu, W. D. Highly polarization sensitive infrared photodetector based on black phosphorus-on-WSe_2 photogate vertical heterostructure. *Nano Energy* **2017**, *37*, 53–60.
[285] Miao, J. S.; Song, B.; Li, Q.; Cai, L.; Zhang, S. M.; Hu, W. D.; Dong, L. X.; Wang, C. Photothermal effect induced negative photoconductivity and high responsivity in flexible black phosphorus transistors. *ACS Nano* **2017**, *11*, 6048–6056.
[286] Mayorga-Martinez, C. C.; Gusmao, R.; Sofer, Z.; Pumera, M. Pnictogen-based enzymatic phenol biosensors: Phosphorene, arsenene, antimonene, and bismuthene. *Angew*. *Chem*., *Int*. *Ed*. **2019**, *58*, 134–138.
[287] Gusmão, R.; Sofer, Z.; Bouša, D.; Pumera, M. Pnictogen (As, Sb, Bi) nanosheets for electrochemical applications are produced by shear exfoliation using kitchen blenders. *Angew*. *Chem*., *Int*. *Ed*. **2017**, *56*, 14417–14422.
[288] Ares, P.; Aguilar-Galindo, F.; Rodriguez-San-Miguel, D.; Aldave, D. A.; Díaz-Tendero, S.; Alcami, M.; Martin, F.; Gómez-Herrero, J.; Zamora, F. Mechanical isolation of highly stable antimonene under ambient conditions. *Adv*. *Mater*. **2016**, *28*, 6332–6336.
[289] Helmersson, U.; Lattemann, M.; Bohlmark, J.; Ehiasarian, A. P.; Gudmundsson, J. T. Ionized physical vapor deposition (IPVD): A review of technology and applications. *Thin Solid Films* **2006**, *513*, 1–24.
[290] Fortunato, E.; Barquinha, P.; Martins, R. Oxide semiconductor thin-film transistors: A review of recent advances. *Adv*. *Mater*. **2012**, *24*, 2945–2986.
[291] Zhong, Q.; Kong, L. J.; Gou, J.; Li, W. B.; Sheng, S. X.; Yang, S.; Cheng, P.; Li, H.; Wu, K. H.; Chen, L. Synthesis of borophene nanoribbons on Ag(110) surface. *Phys*. *Rev*. *Mater*. **2017**, *1*, 021001.
[292] Wu, R. T.; Drozdov, I. K.; Eltinge, S.; Zahl, P.; Ismail-Beigi, S.; Božović, I.; Gozar, A. Large-area single-crystal sheets of borophene on Cu(111) surfaces. *Nat*. *Nanotechnol*. **2019**, *14*, 44–49.
[293] Kiraly, B.; Liu, X. L.; Wang, L. Q.; Zhang, Z. H.; Mannix, A. J.; Fisher, B. L.; Yakobson, B. I.; Hersam, M. C.; Guisinger, N. P. Borophene synthesis on Au(111). *ACS Nano* **2019**, *13*, 3816–3822.
[294] Xing, Y.; Zhang, H. M.; Fu, H. L.; Liu, H. W.; Sun, Y.; Peng, J. P.; Wang, F.; Lin, X.; Ma, X. C.; Xue, Q. K. et al. Quantum Griffiths singularity of superconductor-metal transition in Ga thin films. *Science* **2015**, *350*, 542–545.
[295] Tao, M. L.; Tu, Y. B.; Sun, K.; Wang, Y. L.; Xie, Z. B.; Liu, L.; Shi, M. X.; Wang, J. Z. Gallenene epitaxially grown on Si(111). *2D Mater*. **2018**, *5*, 035009.
[296] Lalmi, B.; Oughaddou, H.; Enriquez, H.; Kara, A.; Vizzini, S.; Ealet, B.; Aufray, B. Epitaxial growth of a silicene sheet. *Appl*. *Phys*. *Lett*. **2010**, *97*, 223109.
[297] Vogt, P.; De Padova, P.; Quaresima, C.; Avila, J.; Frantzeskakis, E.; Asensio, M. C.; Resta, A.; Ealet, B.; Le Lay, G. Silicene: Compelling experimental evidence for graphenelike two-dimensional silicon. *Phys*. *Rev*. *Lett*. **2012**, *108*, 155501.
[298] Feng, B. J.; Ding, Z. J.; Meng, S.; Yao, Y. G.; He, X. Y.; Cheng, P.; Chen, L.; Wu, K. H. Evidence of silicene in honeycomb structures of silicon on Ag(111). *Nano Lett*. **2012**, *12*, 3507–3511.
[299] Lin, C. L.; Arafune, R.; Kawahara, K.; Tsukahara, N.; Minamitani, E.; Kim, Y.; Takagi, N.; Kawai, M. Structure of silicene grown on Ag(111). *Appl*. *Phys*. *Express* **2012**, *5*, 045802.
[300] Jamgotchian, H.; Colignon, Y.; Hamzaoui, N.; Ealet, B.; Hoarau, J.

Y.; Aufray, B.; Bibérian, J. P. Growth of silicene layers on Ag(111): Unexpected effect of the substrate temperature. *J. Phys. Condens. Matter* **2012**, *24*, 172001.
[301] Chen, L.; Liu, C. C.; Feng, B. J.; He, X. Y.; Cheng, P.; Ding, Z. J.; Meng, S.; Yao, Y. G.; Wu, K. H. Evidence for Dirac fermions in a honeycomb lattice based on silicon. *Phys. Rev. Lett.* **2012**, *109*, 056804.
[302] Enriquez, H.; Vizzini, S.; Kara, A.; Lalmi, B.; Oughaddou, H. Silicene structures on silver surfaces. *J. Phys. Condens. Matter* **2012**, *24*, 314211.
[303] Resta, A.; Leoni, T.; Barth, C.; Ranguis, A.; Becker, C.; Bruhn, T.; Vogt, P.; Le Lay, G. Atomic structures of silicene layers grown on Ag(111): Scanning tunneling microscopy and noncontact atomic force microscopy observations. *Sci. Rep.* **2013**, *3*, 3298.
[304] Sone, J.; Yamagami, T.; Aoki, Y.; Nakatsuji, K.; Hirayama, H. Epitaxial growth of silicene on ultra-thin Ag(111) films. *New J. Phys.* **2014**, *16*, 095004.
[305] Tao, L.; Cinquanta, E.; Chiappe, D.; Grazianetti, C.; Fanciulli, M.; Dubey, M.; Molle, A.; Akinwande, D. Silicene field-effect transistors operating at room temperature. *Nat. Nanotechnol.* **2015**, *10*, 227–231.
[306] Grazianetti, C.; Chiappe, D.; Cinquanta, E.; Fanciulli, M.; Molle, A. Nucleation and temperature-driven phase transitions of silicene superstructures on Ag(111). *J. Phys. Condens. Matter* **2015**, *27*, 255005.
[307] Fleurence, A.; Friedlein, R.; Ozaki, T.; Kawai, H.; Wang, Y.; Yamada-Takamura, Y. Experimental evidence for epitaxial silicene on diboride thin films. *Phys. Rev. Lett.* **2012**, *108*, 245501.
[308] Aizawa, T.; Suehara, S.; Otani, S. Silicene on zirconium carbide (111). *J. Phys. Chem. C* **2014**, *118*, 23049–23057.
[309] Chiappe, D.; Scalise, E.; Cinquanta, E.; Grazianetti, C.; van den Broek, B.; Fanciulli, M.; Houssa, M.; Molle, A. Two-dimensional Si nanosheets with local hexagonal structure on a MoS_2 surface. *Adv. Mater.* **2014**, *26*, 2096–2101.
[310] Podsiadly-Paszkowska, A.; Krawiec, M. Dirac fermions in silicene on Pb(111) surface. *Phys. Chem. Chem. Phys.* **2015**, *17*, 2246–2251.
[311] Morishita, T.; Spencer, M. J. S.; Kawamoto, S.; Snook, I. K. A new surface and structure for silicene: Polygonal silicene formation on the Al(111) surface. *J. Phys. Chem. C* **2013**, *117*, 22142–22148.
[312] Bhattacharya, A.; Bhattacharya, S.; Das, G. P. Exploring semiconductor substrates for silicene epitaxy. *Appl. Phys. Lett.* **2013**, *103*, 123113.
[313] Derivaz, M.; Dentel, D.; Stephan, R.; Hanf, M. C.; Mehdaoui, A.; Sonnet, P.; Pirri, C. Continuous germanene layer on Al(111). *Nano Lett.* **2015**, *15*, 2510–2516.
[314] Stephan, R.; Hanf, M. C.; Derivaz, M.; Dentel, D.; Asensio, M. C.; Avila, J.; Mehdaoui, A.; Sonnet, P.; Pirri, C. Germanene on Al(111): Interface electronic states and charge transfer. *J. Phys. Chem. C* **2016**, *120*, 1580–1585.
[315] Dávila, M. E.; Xian, L.; Cahangirov, S.; Rubio, A.; Le Lay, G. Germanene: A novel two-dimensional germanium allotrope akin to graphene and silicene. *New J. Phys.* **2014**, *16*, 095002.
[316] Dávila, M. E.; Le Lay, G. Few layer epitaxial germanene: A novel two-dimensional Dirac material. *Sci. Rep.* **2016**, *6*, 20714.
[317] Bampoulis, P.; Zhang, L.; Safaei, A.; van Gastel, R.; Poelsema, B.; Zandvliet, H. J. W. Germanene termination of Ge_2Pt crystals on Ge(110). *J. Phys. Condens. Matter* **2014**, *26*, 442001.
[318] Acun, A.; Zhang, L.; Bampoulis, P.; Farmanbar, M.; van Houselt, A.; Rudenko, A. N.; Lingenfelder, M.; Brocks, G.; Poelsema, B.; Katsnelson, M. I. et al. Germanene: The germanium analogue of graphene. *J. Phys. Condens. Matter* **2015**, *27*, 443002.
[319] Zhang, L.; Bampoulis, P.; Rudenko, A. N.; Yao, Q.; van Houselt, A.; Poelsema, B.; Katsnelson, M. I.; Zandvliet, H. J. W. Structural and electronic properties of germanene on MoS_2. *Phys. Rev. Lett.* **2016**, *117*, 256804.
[320] Gou, J.; Zhong, Q.; Sheng, S. X.; Li, W. B.; Cheng, P.; Li, H.; Chen, L.; Wu, K. H. Strained monolayer germanene with 1×1 lattice on Sb(111). *2D Mater.* **2016**, *3*, 045005.
[321] Massara, N.; Marjaoui, A.; Stephan, R.; Hanf, M. C.; Derivaz, M.; Dentel, D.; Hajjar-Garreau, S.; Mehdaoui, A.; Diani, M.; Sonnet, P.et al. Experimental molecular adsorption: Electronic buffer effect of germanene on Al(111). *2D Mater.* **2019**, *6*, 035016.
[322] Ni, Z. Y.; Minamitani, E.; Ando, Y.; Watanabe, S. Germanene and stanene on two-dimensional substrates: Dirac cone and Z_2 invariant. *Phys. Rev. B* **2017**, *96*, 075427.
[323] Gao, J. F.; Zhang, G.; Zhang, Y. W. Exploring Ag(111) substrate for epitaxially growing monolayer stanene: A first-principles study. *Sci. Rep.* **2016**, *6*, 29107.
[324] Gou, J.; Kong, L. J.; Li, H.; Zhong, Q.; Li, W. B.; Cheng, P.; Chen, L.; Wu, K. H. Strain-induced band engineering in monolayer stanene on Sb(111). *Phys. Rev. Mater.* **2017**, *1*, 054004.
[325] Deng, J. L.; Xia, B. Y.; Ma, X. C.; Chen, H. Q.; Shan, H.; Zhai, X. F.; Li, B.; Zhao, A. D.; Xu, Y.; Duan, W. H. et al. Epitaxial growth of ultraflat stanene with topological band inversion. *Nat. Mater.* **2018**, *17*, 1081–1086.
[326] Yuhara, J.; He, B. J.; Matsunami, N.; Nakatake, M.; Le Lay, G. Graphene's latest cousin: Plumbene epitaxial growth on a "nano watercube". *Adv. Mater.* **2019**, *31*, 1901017.
[327] Zhang, J. L.; Zhao, S. T.; Han, C.; Wang, Z. Z.; Zhong, S.; Sun, S.; Guo, R.; Zhou, X.; Gu, C. D.; Di Yuan, K. et al. Epitaxial growth of single layer blue phosphorus: A new phase of two-dimensional phosphorus. *Nano Lett.* **2016**, *16*, 4903–4908.
[328] Zhang, J. L.; Zhao, S. T.; Sun, S.; Niu, T. C.; Zhou, X.; Gu, C. D.; Han, C.; Di Yuan, K.; Guo, R.; Wang, L. et al. Phosphorus nanostripe arrays on Cu(110): A case study to understand the substrate effect on the phosphorus thin film growth. *Adv. Mater. Interfaces* **2017**, *4*, 1601167.
[329] Fortin-Deschenes, M.; Moutanabbir, O. Recovering the semiconductor properties of the epitaxial group V 2D materials antimonene and arsenene. *J. Phys. Chem. C* **2018**, *122*, 9162–9168.
[330] Fortin-Deschênes, M.; Waller, O.; Menteş, T. O.; Locatelli, A.; Mukherjee, S.; Genuzio, F.; Levesque, P. L.; Hébert, A.; Martel, R.; Moutanabbir, O. Synthesis of antimonene on germanium. *Nano Lett.* **2017**, *17*, 4970–4975.
[331] Mao, Y. H.; Zhang, L. F.; Wang, H. L.; Shan, H.; Zhai, X. F.; Hu, Z. P.; Zhao, A. D.; Wang, B. Epitaxial growth of highly strained antimonene on Ag(111). *Front. Phys.* **2018**, *13*, 138106.
[332] Chen, H. A.; Sun, H.; Wu, C. R.; Wang, Y. X.; Lee, P. H.; Pao, C. W.; Lin, S. Y. Single-crystal antimonene films prepared by molecular beam epitaxy: Selective growth and contact resistance reduction of the 2D material heterostructure. *ACS Appl. Mater. Interfaces* **2018**, *10*, 15058–15064.
[333] Wu, X.; Shao, Y.; Liu, H.; Feng, Z. L.; Wang, Y. L.; Sun, J. T.; Liu, C.; Wang, J. O.; Liu, Z. L.; Zhu, S. Y. et al. Epitaxial growth and air-stability of monolayer antimonene on $PdTe_2$. *Adv. Mater.* **2017**, *29*, 1605407.
[334] Walker, E. S.; Na, S. R.; Jung, D.; March, S. D.; Kim, J. S.; Trivedi, T.; Li, W.; Tao, L.; Lee, M. L.; Liechti, K. M. et al. Large-area dry transfer of single-crystalline epitaxial bismuth thin films. *Nano Lett.* **2016**, *16*, 6931–6938.
[335] Ismail, R. A.; Hassoon, K. I.; Abdulrazzaq, O. A. Elicitation of barrier height of rapid thermal annealed Bi-nSi Schottky photodetector using various methods: A comparative study. *Optik* **2019**, *188*, 46–51.
[336] Nagao, T.; Sadowski, J. T.; Saito, M.; Yaginuma, S.; Fujikawa, Y.; Kogure, T.; Ohno, T.; Hasegawa, Y.; Hasegawa, S.; Sakurai, T. Nanofilm allotrope and phase transformation of ultrathin Bi film on Si(111)-7 × 7. *Phys. Rev. Lett.* **2004**, *93*, 105501.
[337] Nagao, T.; Yaginuma, S.; Saito, M.; Kogure, T.; Sadowski, J. T.; Ohno, T.; Hasegawa, S.; Sakurai, T. Strong lateral growth and crystallization via two-dimensional allotropic transformation of semi-metal Bi film. *Surf. Sci.* **2005**, *590*, 247–252.
[338] Kammler, M.; Horn-von Hoegen, M. Low energy electron diffraction of epitaxial growth of bismuth on Si(111). *Surf.Sci.* **2005**, *576*, 56–60.
[339] Pan, S. W.; Qi, D. F.; Chen, S. Y.; Li, C.; Huang, W.; Lai, H. K. Se ultrathin film growth on Si(100) substrate and its application in Ti/n-Si(100) ohmic contact. *Acta Phys. Sin.* **2011**, *60*, 712–716.
[340] Luo, L. B.; Yang, X. B.; Liang, F. X.; Jie, J. S.; Li, Q.; Zhu, Z. F.; Wu, C. Y.; Yu, Y. Q.; Wang, L. Transparent and flexible selenium nanobelt-based visible light photodetector. *Crystengcomm* **2012**, *14*, 1942–1947.
[341] Zheng, L. X.; Hu, K.; Teng, F.; Fang, X. S. Novel UV–visible photodetector in photovoltaic mode with fast response and ultrahigh photosensitivity employing Se/TiO_2nanotubes heterojunction. *Small*

2017, *13*, 1602448.
[342] Hu, K.; Teng, F.; Zheng, L. X.; Yu, P. P.; Zhang, Z. M.; Chen, H. Y.; Fang, X. S. Binary response Se/ZnO p-n heterojunction UV photodetector with high on/off ratio and fast speed. *Laser Photonics Rev*. **2017**, *11*, 1600257.
[343] Yang, W.; Hu, K.; Teng, F.; Weng, J. H.; Zhang, Y.; Fang, X. S. High-performance silicon-compatible large-area UV-to-visible broadband photodetector based on integrated lattice-matched type II Se/n-Si heterojunctions. *Nano Lett*. **2018**, *18*, 4697–4703.
[344] Qin, J. K.; Yan, H.; Qiu, G.; Si, M. W.; Miao, P.; Duan, Y. Q.; Shao, W. Z.; Zhen, L.; Xu, C. Y.; Ye, P. D. Hybrid dual-channel phototransistor based on 1D t-Se and 2D ReS_2 mixed-dimensional heterostructures. *Nano Res*. **2019**, *12*, 669–674.
[345] Chang, Y.; Chen, L.; Wang, J. Y.; Tian, W.; Zhai, W.; Wei, B. B. Self-powered broadband schottky junction photodetector based on a single selenium microrod. *J. Phys. Chem. C* **2019**, *123*, 21244–21251.
[346] Chen, Y. Z.; You, Y. T.; Chen, P. J.; Li, D. P.; Su, T. Y.; Lee, L.; Shih, Y. C.; Chen, C. W.; Chang, C. C.; Wang, Y. C. et al. Environmentally and mechanically stable selenium 1D/2D hybrid structures for broad-range photoresponse from ultraviolet to infrared wavelengths. *ACS Appl. Mater. Interfaces* **2018**, *10*, 35477–35486.
[347] Chen, J. L.; Dai, Y. W.; Ma, Y. Q.; Dai, X. Q.; Ho, W.; Xie, M. H. Ultrathin β-tellurium layers grown on highly oriented pyrolytic graphite by molecular-beam epitaxy. *Nanoscale* **2017**, *9*, 15945–15948.
[348] Hegazy, M.; Refaat, T.; Abedin, N.; Elsayed-Ali, H. Quantum-dot infrared photodetector fabricated by pulsed laser deposition technique. *J. Laser Micro/Nanoen*. **2006**, *1*, 111–114.
[349] Carter, A. C.; Horwitz, J. S.; Chrisey, D. B.; Pond, J. M.; Kirchoefer, S. W.; Chang, W. T. Pulsed laser deposition of ferroelectric thin films for room temperature active microwave electronics. *Integr. Ferroelectr*. **1997**, *17*, 273–285.
[350] Yang, Z. B.; Hao, J. H.; Yuan, S. G.; Lin, S. H.; Yau, H. M.; Dai, J. Y.; Lau, S. P. Field-effect transistors based on amorphous black phosphorus ultrathin films by pulsed laser deposition. *Adv. Mater*. **2015**, *27*, 3748–3754.
[351] Apte, A.; Bianco, E.; Krishnamoorthy, A.; Yazdi, S.; Rao, R.; Glavin, N.; Kumazoe, H.; Varshney, V.; Roy, A.; Shimojo, F. et al. Polytypism in ultrathin tellurium. *2D Mater*. **2019**, *6*, 015013.
[352] Tai, G. A.; Hu, T. S.; Zhou, Y. G.; Wang, X. F.; Kong, J. Z.; Zeng, T.; You, Y. C.; Wang, Q. Synthesis of atomically thin boron films on copper foils. *Angew. Chem., Int. Ed*. **2015**, *54*, 15473–15477.
[353] Sofer, Z.; Sedmidubsky, D.; Huber, Š.; Luxa, J.; Bouša, D.; Boothroyd, C.; Pumera, M. Layered black phosphorus: Strongly anisotropic magnetic, electronic, and electron-transfer properties. *Angew. Chem., Int. Ed*. **2016**, *55*, 3382–3386.
[354] Smith, J. B.; Hagaman, D.; Ji, H. F. Growth of 2D black phosphorus film from chemical vapor deposition. *Nanotechnology* **2016**, *27*, 215602.
[355] Xie, C.; Mak, C.; Tao, X. M.; Yan, F. Photodetectors based on two-dimensional layered materials beyond graphene. *Adv. Funct. Mater*. **2017**, *27*, 1603886.
[356] Li, H. L.; Jing, L.; Liu, W. W.; Lin, J. J.; Tay, R. Y.; Tsang, S. H.; Teo, E. H. T. Scalable production of few-layer boron sheets by liquid-phase exfoliation and their superior supercapacitive performance. *ACS Nano* **2018**, *12*, 1262–1272.
[357] Brent, J. R.; Savjani, N.; Lewis, E. A.; Haigh, S. J.; Lewis, D. J.; O'Brien, P. Production of few-layer phosphorene by liquid exfoliation of black phosphorus. *Chem. Commun*. **2014**, *50*, 13338–13341.
[358] Yasaei, P.; Kumar, B.; Foroozan, T.; Wang, C. H.; Asadi, M.; Tuschel, D.; Indacochea, J. E.; Klie, R. F.; Salehi-Khojin, A. High-quality black phosphorus atomic layers by liquid-phase exfoliation. *Adv. Mater*. **2015**, *27*, 1887–1892.
[359] Hanlon, D.; Backes, C.; Doherty, E.; Cucinotta, C. S.; Berner, N. C.; Boland, C.; Lee, K.; Harvey, A.; Lynch, P.; Gholamvand, Z. et al. Liquid exfoliation of solvent-stabilized few-layer black phosphorus for applications beyond electronics. *Nat. Commun*. **2015**, *6*, 8563.
[360] Kang, J.; Wood, J. D.; Wells, S. A.; Lee, J. H.; Liu, X. L.; Chen, K. S.; Hersam, M. C. Solvent exfoliation of electronic-grade, two-dimensional black phosphorus. *ACS Nano***2015**, *9*, 3596–3604.
[361] Kang, J.; Wells, S. A.; Wood, J. D.; Lee, J. H.; Liu, X. L.; Ryder, C. R.; Zhu, J.; Guest, J. R.; Husko, C. A.; Hersam, M. C. Stable aqueous dispersions of optically and electronically active phosphorene. *Proc. Natl. Acad. Sci. USA* **2016**, *113*, 11688–11693.
[362] Wang, H.; Yang, X. Z.; Shao, W.; Chen, S. C.; Xie, J. F.; Zhang, X. D.; Wang, J.; Xie, Y. Ultrathin black phosphorus nanosheets for efficient singlet oxygen generation. *J. Am. Chem. Soc*. **2015**, *137*, 11376–11382.
[363] Woomer, A. H.; Farnsworth, T. W.; Hu, J.; Wells, R. A.; Donley, C. L.; Warren, S. C. Phosphorene: Synthesis, scale-up, and quantitative optical spectroscopy. *ACS Nano* **2015**, *9*, 8869–8884.
[364] Beladi-Mousavi, S. M.; Pourrahimi, A. M.; Sofer, Z.; Pumera, M. Atomically thin 2D-arsenene by liquid-phased exfoliation: Toward selective vapor sensing. *Adv. Funct. Mater*. **2019**, *29*, 1807004.
[365] Qi, Z. H.; Hu, Y.; Jin, Z.; Ma, J. Tuning the liquid-phase exfoliation of arsenic nanosheets by interaction with various solvents. *Phys. Chem. Chem. Phys*. **2019**, *21*, 12087–12090.
[366] Gibaja, C.; Rodriguez-San-Miguel, D.; Ares, P.; Gómez-Herrero, J.; Varela, M.; Gillen, R.; Maultzsch, J.; Hauke, F.; Hirsch, A.; Abellán, G. et al. Few-layer antimonene by liquid-phase exfoliation. *Angew. Chem., Int. Ed*. **2016**, *55*, 14345–14349.
[367] Gu, J. N.; Du, Z. G.; Zhang, C.; Ma, J. G.; Li, B.; Yang, S. B. Liquid-phase exfoliated metallic antimony nanosheets toward high volumetric sodium storage. *Adv. Energy Mater*. **2017**, *7*, 1700447.
[368] Yang, Q. Q.; Liu, R. T.; Huang, C.; Huang, Y. F.; Gao, L. F.; Sun, B.; Huang, Z. P.; Zhang, L.; Hu, C. X.; Zhang, Z. Q. et al. 2D bismuthene fabricated via acid-intercalated exfoliation showing strong nonlinear near-infrared responses for mode-locking lasers. *Nanoscale* **2018**, *10*, 21106–21115.
[369] Zhang, Y. Y.; Rui, X. H.; Tang, Y. X.; Liu, Y. Q.; Wei, J. Q.; Chen, S.; Leow, W. R.; Li, W. L.; Liu, Y. J.; Deng, J. Y. et al. Wet-chemical processing of phosphorus composite nanosheets for high-rate and high-capacity lithium-ion batteries. *Adv. Energy Mater*. **2016**, *6*, 1502409.
[370] Kumar, P.; Singh, J.; Pandey, A. C. Rational low temperature synthesis and structural investigations of ultrathin bismuth nanosheets. *RSC Adv*. **2013**, *3*, 2313–2317.
[371] Ranjan, P.; Sahu, T. K.; Bhushan, R.; Yamijala, S. S. R. K. C.; Late, D. J.; Kumar, P.; Vinu, A. Freestanding borophene and its hybrids. *Adv. Mater*. **2019**, *31*, 1900353.
[372] Ambrosi, A.; Sofer, Z.; Pumera, M. Electrochemical exfoliation of layered black phosphorus into phosphorene. *Angew. Chem., Int. Ed*. **2017**, *56*, 10443–10445.
[373] Xiao, H.; Zhao, M.; Zhang, J. J.; Ma, X. F.; Zhang, J.; Hu, T. J.; Tang, T.; Jia, J. F.; Wu, H. S. Electrochemical cathode exfoliation of bulky black phosphorus into few-layer phosphorene nanosheets. *Electrochem. Commun*. **2018**, *89*, 10–13.
[374] Tchalala, M. R.; Ali, M. A.; Enriquez, H.; Kara, A.; Lachgar, A.; Yagoubi, S.; Foy, E.; Vega, E.; Bendounan, A.; Silly, M. G. et al. Silicon sheets by redox assisted chemical exfoliation. *J. Phys. Condens. Matter* **2013**, *25*, 442001.
[375] Nakano, H.; Mitsuoka, T.; Harada, M.; Horibuchi, K.; Nozaki, H.; Takahashi, N.; Nonaka, T.; Seno, Y.; Nakamura, H. Soft synthesis of single-crystal silicon monolayer sheets. *Angew. Chem., Int. Ed*. **2006**, *45*, 6303–6306.
[376] Li, F. W.; Xue, M. Q.; Li, J. Z.; Ma, X. L.; Chen, L.; Zhang, X. J.; MacFarlane, D. R.; Zhang, J. Unlocking the electrocatalytic activity of antimony for CO_2 reduction by two-dimensional engineering of the bulk material. *Angew. Chem., Int. Ed*. **2017**, *56*, 14718–14722.
[377] Pei, J. J.; Gai, X.; Yang, J.; Wang, X. B.; Yu, Z. F.; Choi, D. Y.; Luther-Davies, B.; Lu, Y. R. Producing air-stable monolayers of phosphorene and their defect engineering. *Nat. Commun*. **2016**, *7*, 10450.
[378] Han, Z. J.; Murdock, A. T.; Seo, D. H.; Bendavid, A. Recent progress in plasma-assisted synthesis and modification of 2D materials. *2D Mater*. **2018**, *5*, 032002.
[379] Tsai, H. S.; Hsiao, C. H.; Lin, Y. P.; Chen, C. W.; Ouyang, H.; Liang, J. H. Fabrication of multilayer borophene on insulator structure. *Small* **2016**, *12*, 5251–5255.
[380] Tsai, H. S.; Hsiao, C. H.; Chen, C. W.; Ouyang, H.; Liang, J. H. Synthesis of nonepitaxial multilayer silicene assisted by ion implantation. *Nanoscale* **2016**, *8*, 9488–9492.

[381] Tsai, H. S.; Chen, Y. Z.; Medina, H.; Su, T. Y.; Chou, T. S.; Chen, Y. H.; Chueh, Y. L.; Liang, J. H. Direct formation of large-scale multi-layered germanene on Si substrate. *Phys*. *Chem*. *Chem*. *Phys*. **2015**, *17*, 21389–21393.

[382] Kang, D. H.; Jeon, M. H.; Jang, S. K.; Choi, W. Y.; Kim, K. N.; Kim, J.; Lee, S.; Yeom, G. Y.; Park, J. H. Self-assembled layer (SAL)-based doping on black phosphorus (BP) transistor and photodetector. *ACS Photonics* **2017**, *4*, 1822–1830.

[383] Jia, J. Y.; Jang, S. K.; Lai, S.; Xu, J.; Choi, Y. J.; Park, J. H.; Lee, S. Plasma-treated thickness-controlled two-dimensional black phosphorus and its electronic transport properties. *ACS Nano* **2015**, *9*, 8729–8736.

[384] Tsai, H. S.; Wang, S. W.; Hsiao, C. H.; Chen, C. W.; Ouyang, H.; Chueh, Y. L.; Kuo, H. C.; Liang, J. H. Direct synthesis and practical bandgap estimation of multilayer arsenene nanoribbons. *Chem*. *Mater*. **2016**, *28*, 425–429.

[385] Tsai, H. S.; Chen, C. W.; Hsiao, C. H.; Ouyang, H.; Liang, J. H. The advent of multilayer antimonene nanoribbons with room temperature orange light emission. *Chem*. *Commun*. **2016**, *52*, 8409–8412.

[386] Li, J. H.; Niu, L. Y.; Zheng, Z. J.; Yan, F. Photosensitive graphene transistors. *Adv*. *Mater*. **2014**, *26*, 5239–5273.

[387] Sun, Z. H.; Chang, H. X. Graphene and graphene-like two-dimensional materials in photodetection: Mechanisms and methodology. *ACS Nano* **2014**, *8*, 4133–4156.

[388] Lauer, R. B.; Williams, F. Photoelectronic properties of graded composition crystals of II-VI semiconductors. *J*. *Appl*. *Phys*. **1971**, *42*, 2904–2910.

[389] Qin, J. K.; Qiu, G.; Jian, J.; Zhou, H.; Yang, L. M.; Charnas, A.; Zemlyanov, D. Y.; Xu, C. Y.; Xu, X. F.; Wu, W. Z. et al. Controlled growth of a large-size 2D selenium nanosheet and its electronic and optoelectronic applications. *ACS Nano* **2017**, *11*, 10222–10229.

[390] Wu, J.; Koon, G. K. W.; Xiang, D.; Han, C.; Toh, C. T.; Kulkarni, E. S.; Verzhbitskiy, I.; Carvalho, A.; Rodin, A. S.; Koenig, S. P. et al. Colossal ultraviolet photoresponsivity of few-layer black phosphorus. *ACS Nano* **2015**, *9*, 8070–8077.

[391] Suess, R. J.; Leong, E.; Garrett, J. L.; Zhou, T.; Salem, R.; Munday, J. N.; Murphy, T. E.; Mittendorff, M. Mid-infrared time-resolved photoconduction in black phosphorus. *2D Mater.* **2016**, *3*, 041006.

[392] Huang, M. Q.; Wang, M. L.; Chen, C.; Ma, Z. W.; Li, X. F.; Han, J. B.; Wu, Y. Q. Broadband black-phosphorus photodetectors with high responsivity. *Adv*. *Mater*. **2016**, *28*, 3481–3485.

[393] Konstantatos, G.; Sargent, E. H. Nanostructured materials for photon detection. *Nat*. *Nanotechnol*. **2010**, *5*, 391–400.

[394] Konstantatos, G.; Badioli, M.; Gaudreau, L.; Osmond, J.; Bernechea, M.; de Arquer, F. P. G.; Gatti, F.; Koppens, F. H. L. Hybrid graphene-quantum dot phototransistors with ultrahigh gain. *Nat*. *Nanotechnol*. **2012**, *7*, 363–368.

[395] Sun, Z. H.; Liu, Z. K.; Li, J. H.; Tai, G. A.; Lau, S. P.; Yan, F. Infrared photodetectors based on CVD-grown graphene and PbS quantum dots with ultrahigh responsivity. *Adv*. *Mater*. **2012**, *24*, 5878–5883.

[396] Guo, Q. S.; Pospischil, A.; Bhuiyan, M.; Jiang, H.; Tian, H.; Farmer, D.; Deng, B. C.; Li, C.; Han, S. J.; Wang, H. et al. Black phosphorus mid-infrared photodetectors with high gain. *Nano Lett*. **2016**, *16*, 4648–4655.

[397] Liu, Y. D.; Cai, Y. Q.; Zhang, G.; Zhang, Y. W.; Ang, K. W. Al-doped black phosphorus p-n homojunction diode for high performance photovoltaic. *Adv*. *Funct*. *Mater*. **2017**, *27*, 1604638.

[398] Wang, J. Y.; Chang, Y.; Huang, L. F.; Jin, K. X.; Tian, W. Designing CdS/Se heterojunction as high-performance self-powered UV–visible broadband photodetector. *APL Mater*. **2018**, *6*, 076106.

[399] Long, M. S.; Gao, A. Y.; Wang, P.; Xia, H.; Ott, C.; Pan, C.; Fu, Y. J.; Liu, E. F.; Chen, X. S.; Lu, W. et al. Room temperature high-detectivity mid-infrared photodetectors based on black arsenic phosphorus. *Sci*. *Adv*. **2017**, *3*, e1700589.

[400] Xu, X. D.; Gabor, N. M.; Alden, J. S.; van der Zande, A. M.; McEuen, P. L. Photo-thermoelectric effect at a graphene interface junction. *Nano Lett*. **2010**, *10*, 562–566.

[401] Song, J. C. W.; Rudner, M. S.; Marcus, C. M.; Levitov, L. S. Hot carrier transport and photocurrent response in graphene. *Nano Lett*. **2011**, *11*, 4688–4692.

[402] Yuan, H. T.; Liu, X. G.; Afshinmanesh, F.; Li, W.; Xu, G.; Sun, J.; Lian, B.; Curto, A. G.; Ye, G. J.; Hikita, Y. et al. Polarization-sensitive broadband photodetector using a black phosphorus vertical p-n junction. *Nat*. *Nanotechnol*. **2015**, *10*, 707–713.